A spectroscopic neutral density diagnostic and exploration of the role of metastable states in fusion and astrophysical plasmas

by

Eleanor Newhouse Williamson

A dissertation submitted to the Graduate Faculty of
Auburn University
in partial fulfillment of the
requirements for the Degree of
Doctor of Philosophy

Auburn, Alabama
December 9, 2023

Keywords: Argon, Neutrals, density, metastables, tokamak, stellarator

Approved by

David Maurer, Professor of Physics
Stuart Loch, Professor of Physics
Dennis Bodewits, Alumni Professor of Physics
Catherine Ramsbottom, Professor of Physics
Edward Thomas, Jr., Charles W. Barkley Endowed Professor of Physics and Dean of the College of Science and Mathematics

Abstract

Understanding the transition region between fully ionized and neutrally dominated plasmas is important to the study of the magnetosphere of the earth, the corona/chromosphere transition regions of the sun, and detached divertors in fusion devices. Regions with partial ionization are typically low temperature plasmas, for which there is a lack of spectroscopic tools generalizable to a wide variety of plasma parameters and sizes. This work presents an Argon spectroscopic neutral density diagnostic that relies on atomic modeling. Argon is used due to its prevalence in Low Temperature Plasma environments. This work also investigates the role of time dependent metastable states in atomic modeling. The Compact Toroidal Hybrid (CTH) device at Auburn University is used as a testbed for the neutral density diagnostic, both in benchmarking and use. For this work the CTH device operates at an electron temperature of 1-10 eV and 1×10^{10} to $1 \times 10^{12}\, cm^{-3}$. The ALEXIS device at Auburn University is used to investigate the role of time dependent metastable states in atomic modeling. In this project, the ALEXIS device operates at an electron temperature of 1-10 eV and 1×10^{9} to $1 \times 10^{10}\, cm^{-3}$. The assumptions in the neutral Ar collisional-radiative modeling for CTH and ALEXIS are confirmed using spectroscopic observations. The neutral argon density diagnostic on CTH is benchmarked across a range of plasma parameters. The neutral density diagnostic on CTH is then used to measure the plasma resistivity. The neutral density diagnostic, and the approach to dealing with metastable states, is expected to make the diagnostic applicable to a range of low temperature plasma devices. Results will be shown from using the neutral diagnostic on CTH to measure resistivity.

Acknowledgments

I could not have made it through this PhD process without the help of others. Thanks go first to Dave Maurer and Stuart Loch. You two have been endlessly patient with me and have played major roles in teaching me to be a scientist.

I am enormously grateful to Nik, Noah, Roger, Tomie, and Dane for operating CTH for me and making the lab group a friendly place to be. Physics is hard, but it would've been enormously more difficult if I hadn't had a group to rely on.

Misha, Taylor, and Ben, you got me through the qualifying exams. Further thanks to Jared and Saikat for showing me how to operate ALEXIS, and to the rest of the folks in that lab group for being so friendly I didn't want to leave.

Thanks to my family including my parents, Adam, Ellen, and Alex for getting me excited about science. Thanks to Alex for supporting me and keeping me sane throughout this process.

Finally, thanks to the friends who have supported me through this process, particularly Sarah and Brandon.

Table of Contents

List of Figures

List of Tables

Chapter 1

Introduction

1.1 Motivation

This work concentrates on improving the understanding and diagnosis of partially ionized Argon plasmas. Such plasmas are present in a wide range of environments. Neutral gas is central to the operation of detached divertors on fusion devices [1]. Detached divertors use neutral gas to slow or stop the flow of plasma to the wall at particular positions in fusion devices. These divertors require a careful balance of injected gas. Too much gas can result in gas in the main body of the plasma. Too little gas can result in plasma hitting and damaging wall components. A neutral density diagnostic is crucial to the careful implementation of this divertor. In addition, certain plasma properties depend on neutral density. Cowling resistivity is dependent on neutral density [2]. Neutrals can impact Alfén wave frequencies and cause damping [3]. Charged particles tend to follow field lines but neutral particles do not. The presence of neutrals in plasmas change the dynamics of those plasmas, but a reliable neutral density diagnostic is required to study this. Finally, neutral density is critical in the study of Low Temperature Plasmas (LTPs) which are typically neutral dominated. These types of plasmas are common in industry, medical environments, food science, and space. Within industry environments plasmas are used in the production of electronics [4]. Within medical environments plasmas are used to sterilize wounds [5]. Plasmas are used within food science for sterilization [6], improving crop yields [6], and food preservation [6].

Pressure sensors are relied upon to measure neutral density through $PV = NRT$, but this has a few drawbacks. First, pressure is not a reliable measurement of neutral density in plasmas with a high fractional ionization. Pressure measurements are typically taken at the edge of a chamber. If the center of a chamber has a significantly different neutral density

from the edge, a pressure measurement will not prove a reliable measurement. Second, most pressure sensors can either measure in high magnetic fields or extremely low vacuum environments. Penning gauges span the regime between the high magnetic field and low vacuum environment, and a Penning Gauge was demonstrated by Kremeyer et al. [7] that utilizes the magnetic field within the chamber. This raises a new challenge: this gauge must be perfectly aligned with the magnetic field in the vacuum vessel.

Spectroscopy has emerged as a promising diagnostic for neutral density [8]. Spectroscopic diagnostics for neutral density are non-invasive but rely on information about the electron temperature and density of the plasma. This information is most readily obtained from a probe, itself an invasive diagnostic [9, 10].

Various optical diagnostic techniques are widely used in diagnosing Argon plasmas. Line ratio diagnostics are used in measuring electron temperature and density [11, 12, 13]. Optical emission spectroscopy is also used in estimating gas temperature [12, 14]. However, the population of Argon metastable states plays a crucial role in the atomic physics that makes optical emission spectroscopy possible [15].

The work presented in this thesis complements existing neutral density diagnostics by providing improved portability and reliability compared to others. A spectroscopic diagnostic at visible wavelengths uses equipment that is relatively portable. The multiple wavelengths used in this work increase the reliability.

This diagnostic improves upon one developed by Sciamma et al. [8] through increased spectral resolution, improved atomic rate calculations [16], and improved reliability. Another diagnostic that uses similar principles, the Lyman-Alpha Measurement Apparatus (LLAMA), has been implemented on the DIII-D experiment to measure Deuterium neutral density [17, 18] using the Ly-α line. Another mechanism involves laser induced fluorescence, an example of which has been implemented on the helicity injected torus (HIT-SI3) in Deuterium [19] and Helium [20]. Both the LLAMA system and systems involving LIF use a limited number of wavelengths to calculate the neutral density. This leads to increased

uncertainty. The diagnostic presented within the scope of this thesis adds certainty to the neutral result through the use of multiple wavelengths.

Spectroscopy is commonly used to

1.2 Overview of this thesis

This thesis has two main focuses. First, the development and testing of a spectroscopic neutral density diagnostic, described in Section 2.3, and second the impact of time-dependent metastables on the atomic model of the plasma, described in Section 3.6. These are closely related, as accurate atomic modeling is crucial in the diagnostic.

The neutral density diagnostic is theoretically generalizable to various plasma geometries and gases, provided the ability to model the atomic characteristics of the plasma. Atomic modeling of the plasma relies on the existence of atomic rate coefficients, described in Section 3.3. Furthermore, atomic modeling of the plasma relies on characterization of metastable populations: many Low Temperature Plasma environments require time-dependent modeling of the atomic metastable states as a part of any spectral diagnostic [21, 22]. The role of the time dependence of metastable states in the plasma and associated spectral modeling will be described in Section 4.6.1.

Chapter 2 will lay out the experimental platforms on which the neutral density diagnostic has been tested: the Compact Toroidal Hybrid (CTH) [23] and the Auburn Linear EXperiment for Instability Studies (ALEXIS) [16]. CTH is an ideal platform for the implementation of the neutral density diagnostic as it is able to achieve a wide range of fractional ionizations, defined as $\frac{n_e}{n_e+n_n}$ in plasmas with only a single degree of ionization. CTH is typically used to study high temperature ($>$100 eV) plasmas, but the work performed for this thesis shows its value in studying low temperature ($<$10 eV) plasmas. By contrast, ALEXIS is an ideal platform for the study of time-dependent metastable states as the vacuum vessel size limits the population achievable by metastable states. The diagnostics used on each

platform will be discussed in Sections 2.6 and 2.25 for the CTH and ALEXIS experiments respectively.

Chapter 3 will describe in depth the atomic physics required for the diagnostics being developed in this dissertation. In particular, angular momentum coupling will be discussed along with atomic level labeling in general in Section 3.4. Metastables will be defined and discussed. Collisional Radiative Modeling is used for the atomic modeling in this dissertation, and the theory will be outlined in Section 4.6.1. A discussion of optical thickness follows in Sections 3.3 and 3.4 for CTH and ALEXIS respectively, and it will be shown that none of the plasmas involved in this work are optically thick. Two atomic datasets were used in this work: one for Ar I and one for Ar II. This dissertation primarily focuses on the modeling of Ar I, although spectral lines are observed for Ar I and Ar II. Ar I atomic data shows good agreement to measured spectral line ratios (Fig. 4.23) as well as other benchmarks. The available Ar II atomic dataset does not accurately model the observed CTH spectra, and the reasons for this discrepancy will be discussed in Section 3.8. This investigation led to collaborators initiating a project to recalculate Ar II atomic data.

Chapter 3 will also present an investigation of spectroscopic electron temperature and density diagnostics based on line ratios. The neutral density diagnostic does not require spectroscopic electron density or temperature diagnostics due to existing Langmuir probe measurements. Nevertheless, it has proven useful to explore whether any line ratios observed had the potential to a provide such a diagnostic within the electron temperature and density parameter space available. None of the lines observed can be used to produce a diagnostic of T_e or n_e with sufficient accuracy.

The main results of the neutral density diagnostics that are developed in this dissertation are presented in Chapter 4. This required combining the absolute intensity calibration of the spectrometer described in Section 2.3.1 with the atomic data described in Chapter 3 to implement on the ALEXIS and CTH experiments. The ALEXIS and CTH plasmas studied in this dissertation represent very different Low Temperature Plasma environments, and

characteristic plasma parameters will be described for each experimental device, including fundamental plasma parameters. The devices have similar electron temperature regimes, both ranging from 2 eV to 10 eV, but ALEXIS operates at a significantly lower electron density and higher neutral density than CTH. The profiles of each device are discussed. The use of the Ar I atomic data file is justified. The CTH device has a relatively flat profile in both electron temperature and electron density. The ALEXIS profile is flat in electron temperature but shows a significant slope in electron density. The importance of time-dependent metastable states in the modeling of ALEXIS is discussed. The CTH experiments are at higher electron densities and longer particle confinement times, so they allow the diagnostic to be tested for the case where the neutral Ar metastables have reached a steady-state condition. By contrast, the ALEXIS experiments allow the role of time-dependence on the atomic populations to be investigated. The validity of the neutral density diagnostic on each device will be described. A comparison between a synthetic spectrum and an experimental spectrum suggests that the atomic model is a good representation of the plasma. This is further supported by a small range of calculated neutral densities based on the available ranges. The electron density shows an expected increase with an increase in power, and the neutral density shows a corresponding decrease with an increase in power. Finally the neutral density is implemented for Ohmic plasmas on CTH. A combination of Ohm's law, neutral density, electron density, and electron temperature are used to model the resistivity of CTH ohmic plasmas. Resistivity values for plasmas that are estimated from Least-Squares fitting are shown to be similar to calculated resistivity values.

Chapter 2

Experimental platforms for the study of Argon plasmas

2.1 The use of magnetic fields to confine plasmas

Magnetic fields are a common mechanism for plasma confinement. A charged particle of charge q with a non-zero velocity $\vec{v}$ in the presence of a magnetic field $\vec{B}$ experiences the Lorentz force F:

$$\vec{F} = q\vec{v} \times \vec{B}. \tag{2.1}$$

A charged particle of mass m with a non-zero velocity in a magnetic field will be pulled towards the corresponding magnetic field line. This results in gyro motion around the field line with a frequency ω:

$$\omega = \frac{|q|B}{m}. \tag{2.2}$$

Particles within a straight cylinder with an axial magnetic field are radially but not axially confined. A toroidal shape creates axial confinement but also a radial gradient in $\vec{B}$. This gradient results in charge separation and an $\vec{E}$ field. This $\vec{E}$ field leads to a radial perpendicular $\vec{E} \times \vec{B}$ drift. This charge separation and resulting perpendicular $\vec{E} \times \vec{B}$ drift can be mitigated through the addition of a poloidal field which combines with the toroidal field to create a helical field. The helical field does not eliminate the drift. Rather, the direction of the drift changes with the magnetic field and cancels out.

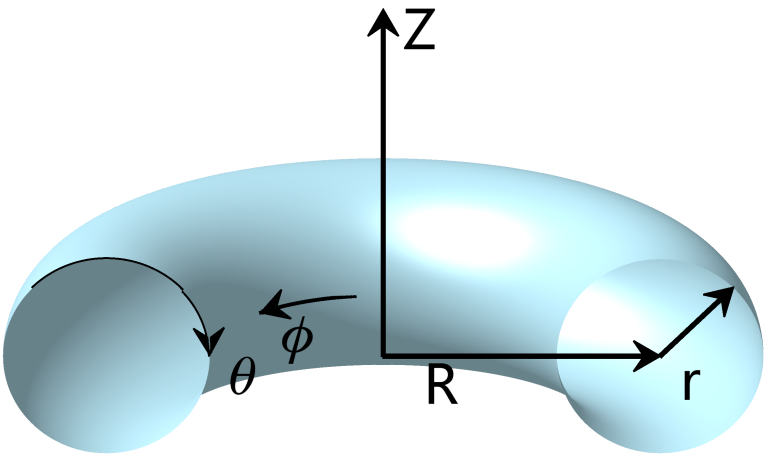

Figure 2.1: A representation of the coordinate system used for this thesis to represent the geometry of a torus. The toroidal direction is shown by ϕ. The poloidal direction is shown by θ. Also shown is the toroidal coordinate system used here. [24]

Fig. 2.1 shows the coordinate system used to described a torus. The vertical displacement from the midplane is described by Z. The major radius, the distance from the center of the full torus, is described by R. The minor radius, the distance from the center of the vacuum chamber, is described by r. The center of the plasma chamber is R_0, r=0. The outer edge of the torus is $\theta = 0$ and increases to $\pi/2$ on the top of the torus. The coordinate ϕ increases counterclockwise around the chamber as seen from the top. The relationship between machine coordinates (R_0, $r\,\theta$) and cylindrical coordinates (R, $z\,\theta$) is described by:

$$\begin{aligned} R &= R_0 + r\cos(\theta), \\ z &= r\sin(\theta), \\ \phi &= \phi. \end{aligned} \tag{2.3}$$

Magnetic surfaces are created by helical magnetic field lines and fall into two categories: rational and irrational [25]. A rational surface is created by a field line making a number of rotations around the chamber and returning to its original location. An irrational surface is

created by a field line coming arbitrarily close to its original location but never the precise point, and in the process ergodically mapping out a surface. A stochastic or chaotic structure can fill a volume [25]. Rational and irrational surfaces produce nested magnetic flux surfaces, which result in confinement. The helicity of the magnetic fields is represented by the rotational transform [26, 25]:

$$\begin{aligned} \iota &= \frac{\iota}{2\pi} \\ \iota &= \frac{d\varphi_p}{d\varphi_t}, \end{aligned} \tag{2.4}$$

where $d\phi_p$ refers to the poloidal flux and $d\phi_t$ refers to the toroidal flux.

Poloidal flux is:

$$\varphi_p = \int \vec{B} \cdot \vec{A_\theta}. \tag{2.5}$$

where $\vec{A_\theta}$ is the poloidal cross sectional area. Toroidal flux is:

$$\varphi_t = \int \vec{B} \cdot \vec{A_\phi}. \tag{2.6}$$

where $\vec{A_\phi}$ is the toroidal cross sectional area.

In the case of rational surfaces, the number of poloidal turns (n) and the number of toroidal turns (m) can be represented as:

$$\iota = \frac{n}{m}. \tag{2.7}$$

A final coordinate system is used to reduce the three-dimensional cylindrical plasma to one-dimension: the flux coordinate system s. This works on the principle that the electron temperature and electron density of charged particles tend to be constant on flux surfaces, justified in Table 4.1. The flux surface coordinate system is simply the toroidal flux at the flux surface of interest normalized to the toroidal flux at the last closed flux surface.

Two plasma devices are used for this work. The Compact Toroidal Hybrid (CTH) experiment is a torsatron with a major radius $R_0 = 75\,\text{cm}$ and a minor radius $a_{vessel} = 29\,\text{cm}$ [23]. The Auburn Linear EXperiment for Instability Studies (ALEXIS) is a cylindrical device of radius 5 cm and length 1.2 m. An axial magnetic field radially confines charged particles. This device lacks axial confinement for charged particles. In addition, the small radius results in neutral particles collisions with the wall after approximately 5 ms. The details of how this can be calculated for ALEXIS are shown in Section 4.6.3.

One focus of this thesis concerns the importance of modeling the spectral emission of neutral Argon time-dependently. The key factor is that the population of the neutral Argon bound electrons that are in excited states increases over time as the atoms remain in the bulk plasma, but a collision with a wall returns them to the ground state. The contrast between these two experiments provides an opportunity for this investigation. Owing to the size and plasma parameters, Argon neutral metastable states (highly populated excited states that are described in Section 4.6.1 on CTH are best modeled as being in steady-state along with the ground population. By contrast, Argon neutral metastables on ALEXIS are best modeled time-dependently. This is further discussed in Section 4.6.1.

Parameter	Definition	CTH Value	ALEXIS value
n_e	electron density (cm^{-3})	1×10^{10} to 1×10^{12}	1×10^{8} to 1×10^{10}
T_e	electron temperature (eV)	1 - 10	1 - 10
χ	Fractional ionization (%)	0.01-99	1×10^{-4}
I_p	plasma current (kA)	0.5	-
a	plasma minor radius (cm)	19	3.5
r	chamber minor radius (cm)	29	5
R_0	CTH major radius (cm)	75	-
L	ALEXIS chamber length (cm)	-	120
$< \|B\| >$	magnetic field strength (T)	0.6	0.05
P	Pressure (mTorr)	5×10^{-11}	0.5
	Plasma lifetime (ms)	100	Steady state

Table 2.1: A brief summary of plasma parameters used in the experiments for this dissertation, comparing CTH and ALEXIS. Descriptions of each device follow. A more complete summary of CTH plasma parameters can be found in Table 4.1, and a more complete summary of ALEXIS plasma parameters can be found in Table 4.2. Note that in some cases, such as the electron density of CTH, actual values sweep multiple orders of magnitude.

Table 2.1 shows the parameter space in which each device operates. While CTH is capable of operating in a higher temperature regime, as high as 200 eV [24], this thesis operates both CTH and ALEXIS in the same temperature regime of 1 to 10 eV. CTH is larger than ALEXIS and operates at a higher electron density and field strength. ALEXIS operates at a higher neutral pressure than CTH.

2.2 The Compact Toroidal Hybrid experiment

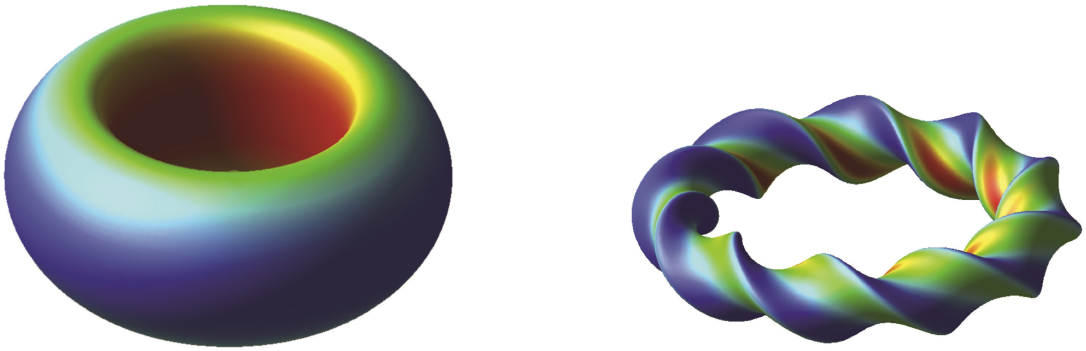

(a) Tokamak (b) 10 field period stellarator

Figure 2.2: Last closed flux surfaces of an axisymmetric tokamak and a 10 field period stellarator. Colors correspond to field strength, where red is the strongest and blue is the weakest [27].

CTH is a stellarator/tokamak hybrid. The tokamak obtains closed magnetic flux surfaces through the use of current driven inductively by a central solenoid. A stellarator by contrast obtains closed magnetic flux surfaces through the use of external magnetic coils. In the case of CTH these field coils are helical. Plasma breakdown and heating primarily comes from Electron Cyclotron Resonance Heating (ECRH) through 17.65 GHz and 18 GHz klystrons.

2.2.1 Magnetic Field Configuration

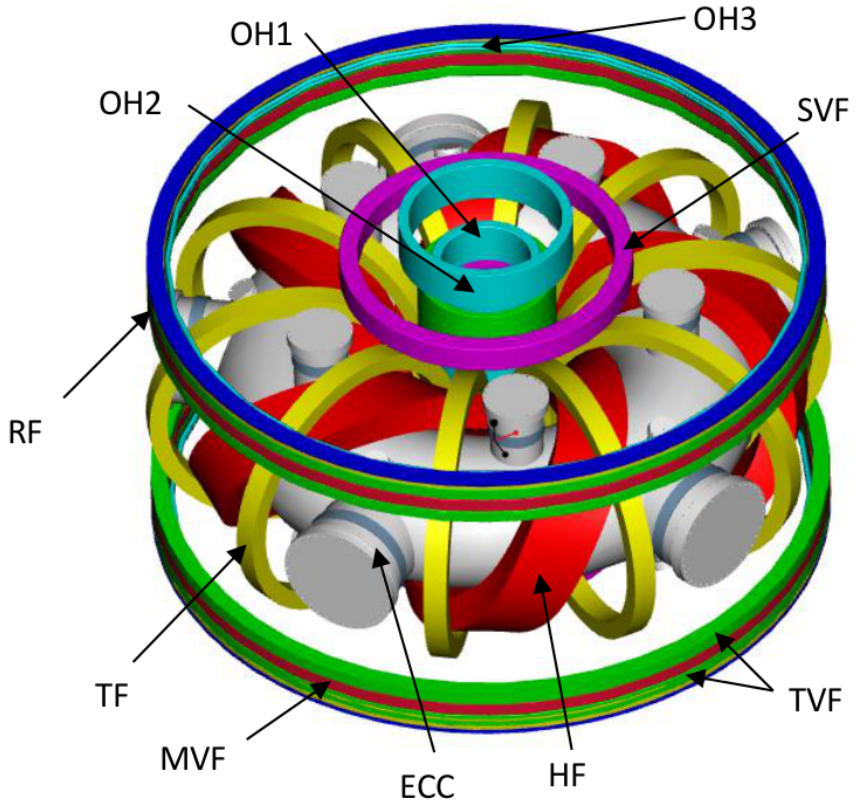

Figure 2.3: Magnetic field coils used for confinement

Fig. 2.3 shows the available coils:

- Ten Toroidal Field (TF) coils, shown in yellow, are used to create a toroidal field.
- Two Main Vertical Field (MVF) coils, upper and lower winding packs, are shown in red and are connected in series with the Helical Field (HF) coil. These are the primary source of poloidal field and result in closed flux surfaces.
- Two Trim Vertical Field (TVF) coils, also upper and lower, are used to adjust the horizontal position of the flux surfaces.
- Vertical positioning is provided by Radial Field (RF) coils.

- A Shaping Vertical Field (SVF) coil set shown in purple provides a quadropole field. This can adjust the elongation of the plasma. This coil set is not used for these experiments.

- A Radial Field (RF) coil set is shown in blue. It is available to vertically adjust the plasma.

- An Ohmic Heating (OH) coil shown in teal in the center drives toroidal current in the plasma. This is a source of heating as well as poloidal field. This is used in this thesis to a limited degree: this thesis uses up to 0.5 kA, as opposed to the >50 kA available[24].

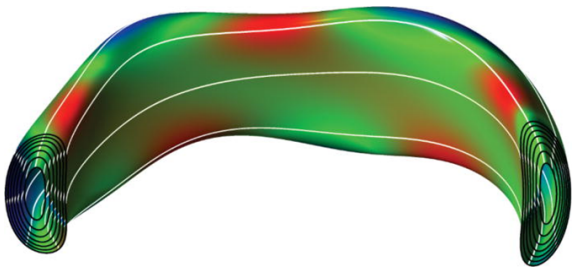

Figure 2.4: An example of nested flux surfaces. Color represents magnetic field strength: red is the strongest field and blue is the weakest field. Select magnetic field lines are shown in white. [28]

Flux surface (s) is a natural radial measurement unit for toroidal devices as charged particles tend to follow field lines. Fig. 4.3 shows estimated transport times perpendicular and parallel to magnetic field lines. Transport perpendicular to magnetic field lines is driven by collisions with neutrals, and thus neutral density. Electrons tend to travel around CTH in approximately $10^{-5}\,s$, whereas the time for electrons to hit the wall ranges from 10^{3} to $10^{7}\,s$. The difference is less extreme for ions. Ions travel one rotation around CTH in approximately $10^{-3}\,s$ and across CTH in 10^{-2} to $10^{4}\,s$. These values are demonstrated in Fig. 4.3. The result of these stark differences is that electron temperature and density tends to be constant on flux surfaces. As a result, flux surfaces are a natural unit of measurement on toroidal

devices as they allow a conversion from a 3-D coordinate system (Z, R, and ϕ) to a 1-D coordinate system (s).

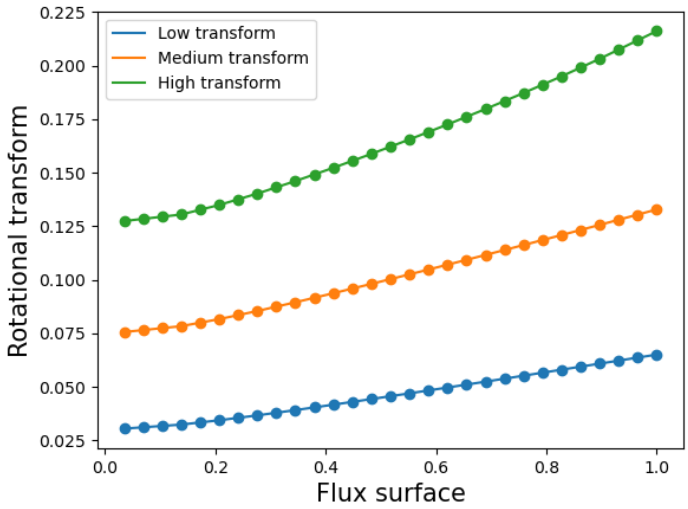

Figure 2.5: Rotational transform vs. flux surface (s) for low, medium, and high vacuum transforms.

The flux surface coordinate system defines $s = 1$ at the last closed flux surface. Fig. 2.5 shows the radial rotational transform vs. flux surface for three separate magnetic field configurations that are used in this work.

CTH is an ideal testbed for the spectroscopic neutral density diagnostic as it has access to a broader range of neutral densities and fractional ionizations than other devices. Glow discharge plasmas are low density ($10^8 - 10^9\, cm^{-3}$) with small fractional ionizations ($10^{-6} - 10^{-7}$). Fusion relevant plasmas are typically high to fully ionized with a correspondingly high fractional ionization. By contrast, CTH is able to span the full range from low to high fractionally ionized. Furthermore, plasmas can be created through ECRH alone or through ECRH coupled with OH. This further widens the regime of plasma parameters that can be investigated and allows resistivity effects to be investigated. These effects are explored in Section 4.8. Finally, CTH is able to decouple plasma creation from plasma confinement. Where other experiments see their plasmas grow in size with an increase in electron density, CTH plasma are sufficiently well confined that the size of the plasma remains unchanged

with electron density. This can be observed in Fig. 4.4 which compares two plasmas with different electron densities.

A limitation for CTH as a testbed for the neutral density diagnostic lies in the difficulty in benchmarking this diagnostic on CTH. The first problem arises in finding an appropriate pressure gauge. Existing pressure gauges on CTH cannot be used simultaneously with a plasma because the strong magnetic fields on CTH would be damaging. Many pressure gauges that function reliably in such high magnetic field do not work at the pressures on CTH. Second, a plasma with a high degree of fractional ionization has a lower neutral density at the center of the plasma than at the edge, where a pressure gauge would naturally measure. While this is also a possible drawback to a line-integrated spectroscopic diagnostic, the electron density radial profile, shown in Section 4.5.1.1, is fairly flat throughout the plasma and falls off quickly close to the edge. Most of the light that enters the spectrometer comes from the region of the plasma with the flat electron density. As a result, the spectrometer will measure the neutral density closer in a region of the plasma with roughly constant plasma parameters. The neutral density diagnostic was benchmarked on CTH by changing the amount of input power while keeping the amount of input gas constant. The observed electron density increased with an increase in power while the observed neutral density decreased with an increase in power by a similar amount. These results are presented in Section 4.7.2.

2.2.2 Diagnostics

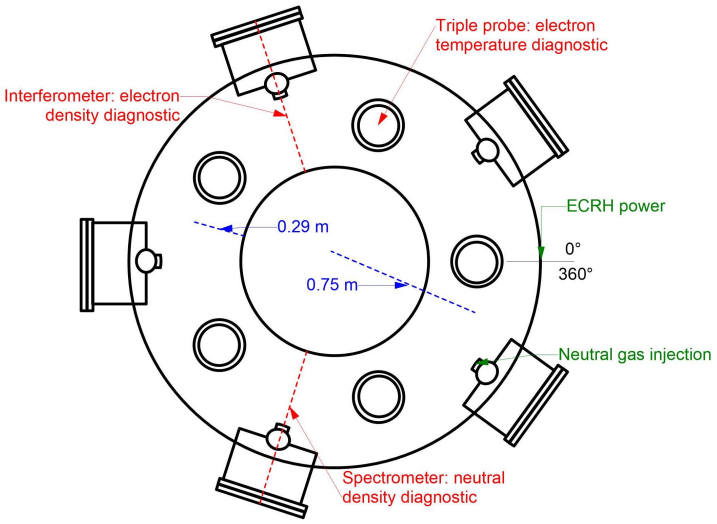

Figure 2.6: Toroidal location of CTH diagnostics

A range of plasma diagnostics are used on CTH for this work. Three diagnostics play a crucial role in the atomic modeling necessary for the neutral density diagnostic. Their toroidal locations are shown in Fig. 2.6. First is a three channel millimeter wave interferometer used to measure horizontal line integrated electron density. It is located at $\theta = 108°$ and takes horizontal measurements at the midplane, 7 cm above the midplane, and 14 cm above the midplane. Secondly, a triple tipped Langmuir probe is located at $\theta = 72°$ and $R = 0.71\ m$. This measures local electron temperature and electron density. It is vertically scannable from a top port and can be moved between plasma discharges to take a radial scan of electron temperature and density. Thirdly, a spectrometer was used exclusively to measure neutral density. An attempt was made to find line ratios that could be used to measure electron temperature or density, but none were found. A discussion of this can be found in Section 3.9.

Additional diagnostics are present on CTH, including but not limited to diagnostics to measure toroidal loop voltage, poloidal plasma current, magnetic fields, and coil currents. The toroidal loop voltage and the poloidal plasma current are relevant in Ohmic plasmas, and

are used in this work to estimate the resistivity caused by Coulomb collisions and electron-neutral collisions. A discussion of that investigation is in Section 4.8. The magnetic fields and coil currents are used in reconstructions of the plasma which are used to estimate radial electron density from line integrated interferometer signal. A discussion of that work is in Section 4.5.1.2.

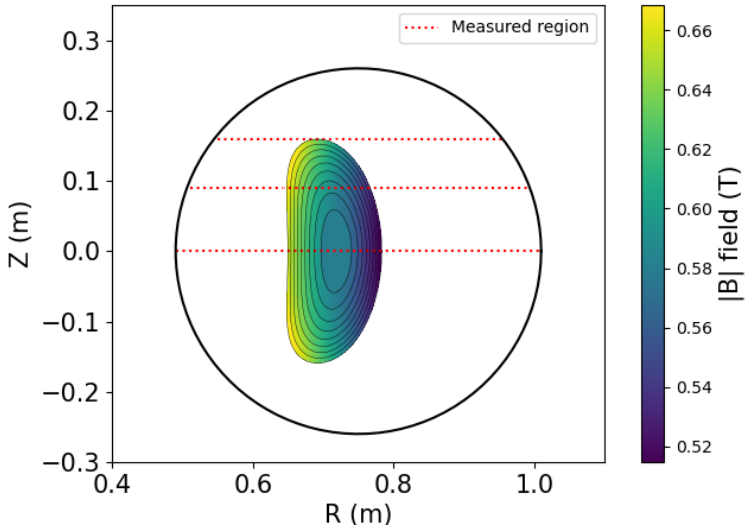

(a) Paths for interferometer chords. Central chord also represents spectrometer. Interferometer and spectrometer are located at separate toroidal locations but identical field periods.

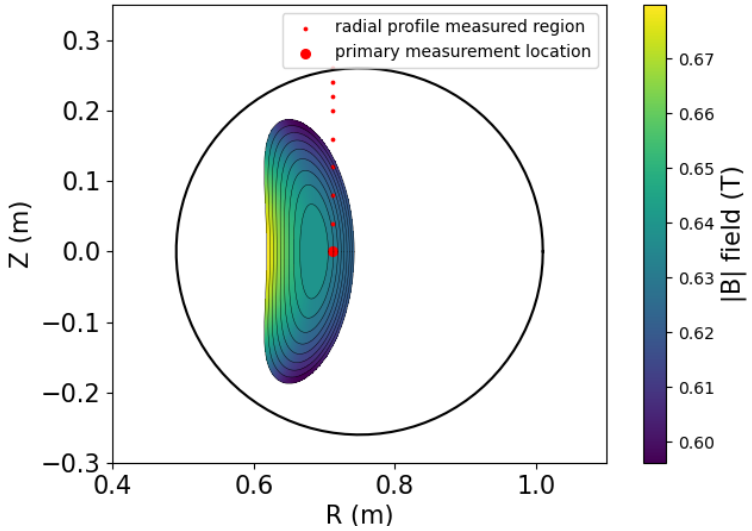

(b) Triple probe measurement locations. Triple probe can be moved between discharges to obtain local measurements ranging from the center of the chamber to the edge.

Figure 2.7: Both figures show chamber cross-sections. Fig. 2.7a shows the cross section at the locations of the interferometer and spectrometer. The dotted red line shows the region which is measured by both: both are line integrated measurements through the center. Fig. 2.7b shows the cross section at the measurement locations of the triple probe. The triple probe, in contrast to the interferometer and spectrometer, makes a local measurement of the plasma and the probe must be moved between plasma discharges. The magnetic field strength is shown in color. The chamber itself is shown as a large black circle, and closed flux surfaces are shown as smaller black ovals. Note that plasma exists outside of the colored region shown due to the ineffectiveness of limiters with little or no current.

A comparison is performed between the horizontal, line integrated electron density measurement performed by the interferometer and the local measurements performed by the triple using a tool V3FIT. V3FIT is a code for equilibrium reconstruction of three-dimensional plasmas [29]. For this work it is used to reconstruct the interferometer data and estimate local electron density values which can then be compared to those of the triple probe, a process which is described in Section 4.5.1.2. The plasma lasts approximately 100 ms with a 5 minute rest between. The triple probe is moved vertically between plasmas to obtain a vertical profile of electron temperature and density values from the center of the chamber (and ideally the plasma center) to the edge. The triple probe shows a non-zero value of electron density past the last closed flux surface. When CTH operates with a high current, limiters at the edge of the plasma limit the size of the plasma by stopping electrons. These limiters are less effective with little or no current, and so the plasma is able to extend past the flux surface that would otherwise be defined as the last closed flux surface.

The plasma cross sections for the interferometer and triple probe in Fig. 2.7 differ in both shape and magnetic field values owing to different field period locations: the interferometer and spectrometer are both at half field periods, whereas the triple probe is at a full field period. This simplifies comparison between interferometer and spectrometer values: both diagnostics are line-integrated measurements for which the length must be taken into account, but the plasma can be assumed to have the same length. Uniformity in electron temperature and density on flux surfaces allows for a comparison between triple probe and interferometer data despite their differing field periods.

Uncertainties used for the triple probe and interferometer are 25%. Uncertainty used for the neutral density is the standard deviation across the wavelengths chosen, under 20% for 93% of the frames available. This is discussed in more detail in Section 2.6.

2.2.2.1 Triple Probe

The current flowing through any biased Langmuir probe tip I_j can be expressed as[30]:

$$I_j = I_e \exp[\frac{e}{k_B T_e}(V_j - V_p)] - I_{sat}, \tag{2.8}$$

where I_e is the current from the electrons, I_{sat} is the ion saturation current, k_B is the Boltzmann constant and T_e the electron temperature, V_j is the probe tip potential and V_p the plasma potential.

Our triple probe is comprised of three Langmuir probe tips. Tip 2 is floating ($V_2 = V_f$): there is no current flowing through it, so $I_2 = 0$:

$$\begin{aligned} I_e \exp(\frac{e}{k_B T_e}(V_f - V_p)) &= I_{sat} \\ I_e \exp(-\frac{e}{k_B T_e} V_p) &= I_{sat} \exp(-\frac{e}{k_B T_e} V_f). \end{aligned} \tag{2.9}$$

Probe tips 1 and 3 have a fixed potential applied between them, such that probe tip 1 is biased positively with respect to probe tip 3. As a result, probe tip 1 draws an electron current (-I), but the bias between them means that tip 3 must draw an identical ion current, described as I_{sat}: $I_1 = I_3 = I_{sat}$. The bias between them must be high enough to force probe tip 3 to draw an ion current I_{sat}. Probe tip 1 has a potential of ϕ_1 and probe tip 3 a potential of ϕ_3, so:

$$I_1 = I_{sat} = I_e \exp[\frac{e}{k_B T_e}(V_1 - V_p)] - I_{sat}. \tag{2.10}$$

Rearrange:

$$\begin{aligned} I_1 = I_{sat} &= I_e \exp(\frac{e}{k_B T_e} V_1) \times \exp(-\frac{e}{k_B T_e} V_p) - I_{sat} \\ &= \exp(\frac{e}{k_B T_e} V_1) \times I_e \exp(-\frac{e}{k_B T_e} V_p) - I_{sat} \end{aligned}$$

Combine with Eq. 2.9:

$$\begin{aligned} &= \exp(\frac{e}{k_B T_e} V_1) \times I_e \exp(-\frac{e}{k_B T_e} V_p) - I_{sat} \\ &= \exp(\frac{e}{k_B T_e} V_1) \times I_{sat} \exp(-\frac{e}{k_B T_e} V_f) - I_{sat} \\ I_1 = I_{sat} &= I_{sat} \exp[\frac{e}{k_B T_e}(V_1 - V_f)] - I_{sat}. \end{aligned}$$

This can be rearranged to show:

$$\frac{k_B T_e}{e} = \frac{V_1 - V_f}{ln(2)}. \tag{2.11}$$

Eq. 2.11 shows how the temperature can be extracted from triple probe measurements. This expression is only valid when the bias voltage between probes 1 and 3 is sufficient to draw ion current. A series of experiments was conducted for the plasma parameters presented in this thesis in which the bias voltage was changed for a series of unchanging plasmas and the ion saturation current measured. A bias voltage of 200 V was chosen.

In deriving the electron density, we start with the ion saturation current[4]:

$$I_{sat} = n_s e A \sqrt{\frac{k_B T_e}{M_i}}, \tag{2.12}$$

where n_s is the Bohm sheath density, e is the electron density, M_i is the ion mass, and A is the exposed surface area of the probe tip. A description of the calculation of the probe surface area is below.

Assuming Maxwellian electrons the electron density is related to the sheath density by the following:

$$n_s \approx n_e \exp(-1/2). \tag{2.13}$$

Eq. 2.12 and 2.13 can be combined to equate the ion saturation current to the electron density.

$$I_{sat} = n_e e A \sqrt{k_B T_e / M_i} \exp(-1/2). \tag{2.14}$$

Electron density can be estimated from this:

$$n_e = \frac{I_{sat}}{eA} \sqrt{\frac{M_i}{k_B T_e}} \exp(\frac{1}{2}). \tag{2.15}$$

Eq. 2.15 is comprised of values that are physical constants, values that are estimated from probe theory, and values that are estimated experimentally. The ion saturation current I_{sat} and the electron temperature T_e are both estimated from probe theory. The ion saturation current is measured by the circuit itself, whereas the electron temperature is calculated through Eq. 2.11. The electron charge e, the ion mass M_i, and the Boltzmann constant k_B are physical constants.

The exposed surface area of the probe, A, is the only term that is measured. The exposed surface area of the probe is calculated as ($\frac{1}{2}$ (cylinder area + tip area)) = $\frac{1}{2}(2 \times \pi \times r \times h + \pi \times r^2)$. The radius of each tip is estimated to be 0.6477 mm and the length of each tip is estimated to be 3 mm for a final value of $1.35 \times 10^{-5}\, m^{-2}$. A vernier caliper is used for both measurements. The factor of $\frac{1}{2}$ comes from the difference between the projected area and the physical area: the presence of the magnetic field limits the possible direction of the electrons. Further uncertainty arises from the fact that the Bohm sheath should be considered in the collection area, posing a problem as the Debye length for the plasmas represented here ranges from to 0.007 mm (for a 10 eV, $1 \times 10^9\,\mathrm{cm}^{-3}$ plasma) to 0.7 mm (for a 1 eV, $1 \times 10^2\,\mathrm{cm}^{-3}$ plasma). The lowest Debye lengths do not contribute to the probe radius. The highest Debye lengths are comparable with the probe radius and would change the collection area. As a result of these two issues, the electron density presented through most of this thesis is obtained from the interferometer rather than the triple probe. The exception to this is the measurement of the vertical density profile.

Figure 2.8: Full triple probe before upgrade.

CTH had a triple probe installed prior to this work with a design described above, but it required an upgrade. The original design involved a 4-bore piece of alumina ceramic with tungsten wire in three of the bores. The tungsten wire extended approximately 3 mm at the end. The alumina was held to the outer structure using an aluminum collar in conjunction with a set screw. The full setup can be seen in Fig. 2.8. Tungsten sputtering would deposit from the wires onto the tip of the alumina, creating a short between the three wires. A more permanent solution was found by redesigning the collar that already existed in the triple probe design: the new collar holds three alumina ceramic pieces separately rather than one alumina piece with three separate tungsten wires.

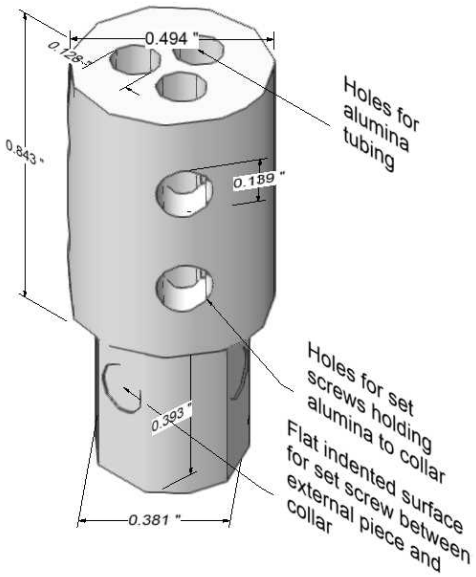

Figure 2.9: Rendering of the updated collar that simultaneously holds and separates the alumina tubing.

Fig. 2.9 shows the replacement collar that holds the ceramic tubing. Tubing fits through holes vertically through the collar. This tubing is then held in place with set screws shown on the top of the piece.

Figure 2.10: Probe tips after updated collar was implemented. The thinner portion of the collar is used to attach the part to an outer portion, as can be seen in Fig. 2.8.

Fig. 2.10 shows a picture of the probe tips once the new collar was implemented. This new collar was successful in solving the problem of shorting. The only drawback of this new triple probe design is an increase in the probe tip separation: the tips are now 5 mm apart, which limits the spatial resolution of the probe. This is not a concern on CTH due to the size and uniformity of the plasma.

2.2.2.2 Spectrometer

A portable spectrometer is implemented on both CTH and ALEXIS which measures Argon emission lines that are used to estimate neutral density.

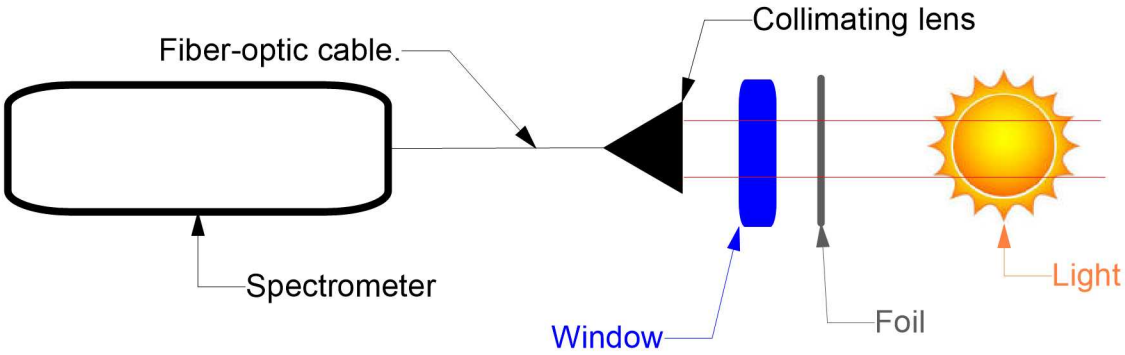

Figure 2.11: Optical setup used to calibrate spectrometer and to use the spectrometer to take plasma data. "Light" is a stand-in for either the calibration sphere or the plasma.

The spectrometer is a Princeton Instruments HRS-500 spectrometer used in conjunction with a PIXIS camera. A laptop with the Princeton Instruments software Lightfield is used to

control the spectrometer and the camera. Data is stored in both the Lightfield proprietary software and csv format along with the frame number, frame start time to microsecond accuracy, frame end time to microsecond accuracy, wavelenth, and intensity.

The diffraction grating used has a groove density of 600 g/mm. While centered at 735 nm the resolution is 0.12 nm and the wavelength window is 83 nm. Both the resolution and wavelength window will change slightly depending on the central wavelength. The fiber optic cable used on CTH does not transmit light below 350 nm. The wavelength windows used on CTH for the data in this thesis are approximately 400 nm to 480 nm and 695 nm to 775 nm. The wavelength windows used on ALEXIS for this thesis are approximately 660 nm to 860 nm.

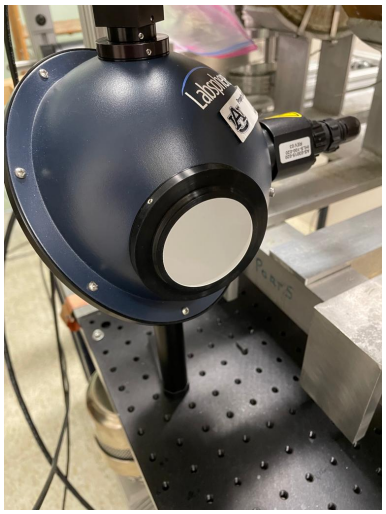

Figure 2.12: Labsphere integrating sphere.

For the neutral density diagnostic, it is important that an intensity calibration be performed on the spectrometer. For this purpose we purchased an integrating sphere. Fig. 2.11 shows the optical setup used to absolutely calibrate the spectrometer as well as make measurements of the plasma. Fig. 2.12 a Labsphere integrating sphere with a known radiance is used to absolutely calibrate the spectrometer. The integrating sphere has a 6 inch spectraflect coated inner diameter with a 2.5 inch exit port. A port reducer limits the exit port diameter to be 2 inches. The top port has a silicon detector used to measure total

light levels and account for a decrease in light levels over the lifetime of the sphere. As the integrating sphere is used, the light levels drop over time. All wavelengths are predicted to drop at similar rates, and so the calibration can be updated accordingly. The light levels did not drop sufficiently during this thesis work to require this adjustment. The light source for the sphere is a 20 Watt tungsten halogen lamp. The system is calibrated from 350 nm to 2400 nm with a relative uncertainty of 1.1% in the wavelength regime of interest.

2.3 Spectrometer absolute calibration procedure and use of the calibration in the measurement of neutral density

It is important to note that "ground state density of Argon I" and "neutral density" are used interchangeably throughout this thesis. While the neutral density is the density of all populations of Argon I combined, including ground state, metastable, and all excited states, only including the density of the ground state is a reasonable approximation. The next most populated state is the first excited state, a metastable, which will have a population at most of 1% of the population of the ground state for the plasma electron densities and temperatures used in this thesis.

The spectrometer is used to estimate neutral density in the following three-step process.

1. Use the spectral line intensity from an absolutely calibrated spectrometer to estimate the population of Argon atoms in a particular excited state.

2. Use a Collisional Radiative Model (CRM) solver, detailed in Section 3.3 to estimate the ratio of Argon atoms in that excited state to the population in ground.

3. Combine steps 1 and 2 to estimate the neutral density of Argon.

The spectrometer must be absolutely calibrated in order to be used to measure the population of excited state Argon atoms. This was done using a Labsphere Integrating Sphere.

2.3.1 Calibration Procedure

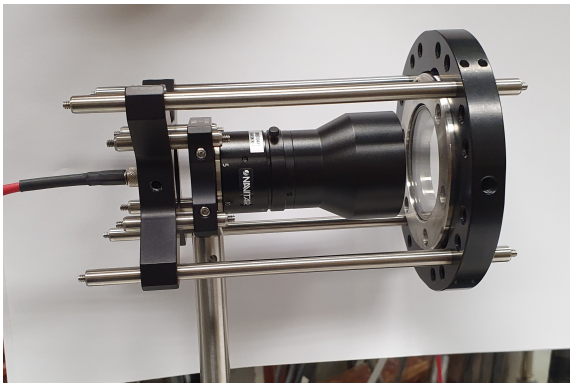

(a) Lens configuration for calibration and operation on ALEXIS. Clamp holds window in front of lens. Post, attached to an optical table, holds full system.

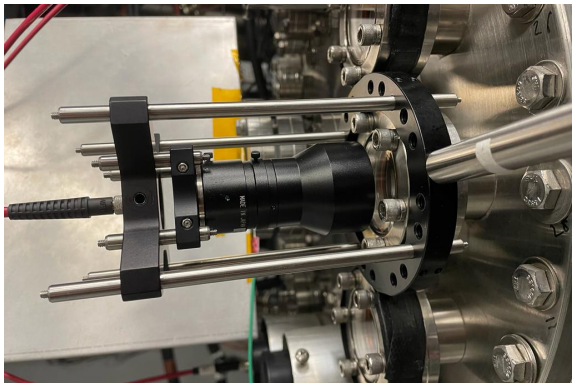

(b) Lens configuration during operation on CTH. Full system is clamped to window and post is unused.

Figure 2.13: A comparison between the lens configuration during calibration and operation on ALEXIS, shown in Fig. 2.13a and lens configuration during operation on CTH, shown in 2.13b.

The fiber optic was positioned at the focal length of the lens to ensure that the lens gathered collimated light. This was done by back-lighting the fiber and observing the resulting spot-size from the lens at varying distances. The lens system was ultimately moved into a position with respect to the fiber where the beam of light maintained the same size regardless of the distance from the lens. The sphere was positioned in front of the lens at a distance of approximately one foot. The distance was set by convenience and does not make a difference in the calibration. This assumption is tested in Section 2.3.3.2. The lens system was positioned such that the collection area of the lens was fully within the output light port of the sphere. The whole optical system (window, lens, fiber) was covered with black material to get rid of stray light. Two identical windows were used, one on CTH and one during calibration, to calibrate out any effect the CTH window could have. The effect of the two windows was compared and deemed to be negligible.

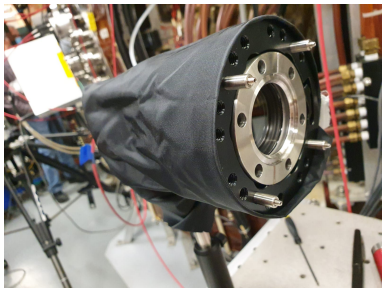

Figure 2.14: Covered lens system

Spectra were taken of light from the sphere. The sphere produces uniform light of known intensity in units of radiance (L_λ):

$$L_\lambda = \frac{Power}{A_{source} \times \Omega}. \tag{2.16}$$

Radiance constitutes power emitted from area A_{source} into solid angle Ω. Radiance does not diminish with distance from the source. Several factors impact the amount of light that the spectrometer takes in, and the only one that can be changed between calibration and experiment is the integration time: the integrating time was chosen to ensure the maximum possible number of counts without saturation. Other factors that impact light levels include the spectroscopic slit width and lens aperture size. The spectrometer measures a certain number of counts, converted to counts/s through division by the frame duration. The lamp radiance was provided by Labsphere in 1 nm increments. A python interpolation function was used on the radiance data provided by Labsphere to find the radiance for any wavelength at which the lamp emits. The radiance from the lamp was divided by the spectroscopically measured intensity of the lamp in counts/s, and the resulting value for every measured wavelength was used as the calibration function.

Fig. 2.15 shows the radiance vs. wavelength curve provided by Labsphere.

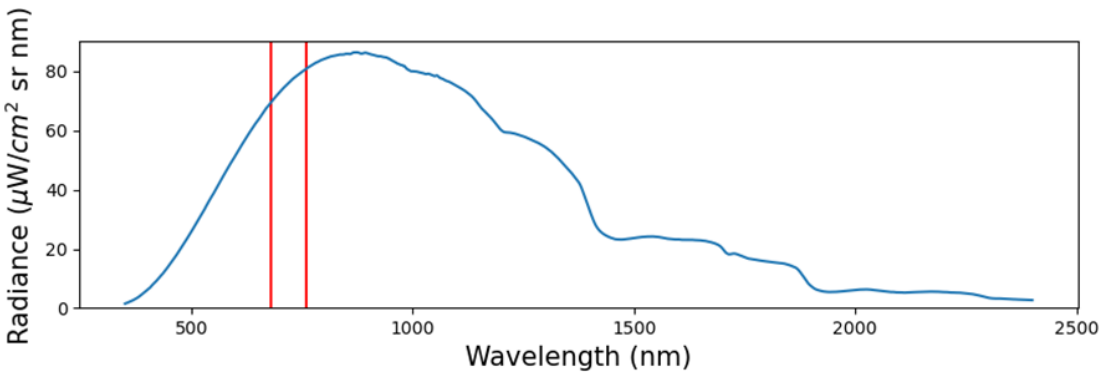

Figure 2.15: Radiance vs. wavelength curve for calibration sphere obtained from manufacturer that allows calibration to proceed.

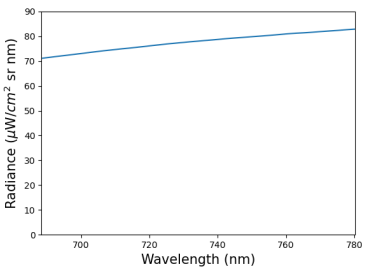

(a) Radiance vs. wavelength for calibration sphere obtained from manufacturer.

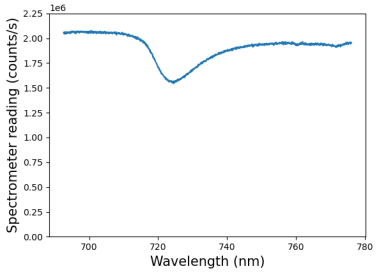

(b) Counts per second of the sphere measured by the spectrometer.

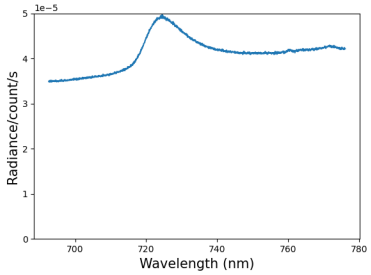

(c) Calibration curve for the spectrometer measured in Radiance/counts/s.

Figure 2.16: Calibration process for the spectrometer. Fig. 2.16a is Fig. 2.15 in the regime of interest for CTH spectra.

Spectra of the plasma were obtained as a function of wavelength and are in units of counts. A background frame was obtained and the appropriate number of counts were subtracted from the plasma spectrum. The background counts range between 550 and 750 counts. By contrast, pixel saturation occurs at 66,000 counts and the weakest line that can be fit is approximately 1000 counts above the background. In the case of CTH, the spectrometer takes frames before the plasma turns on, so the first frame becomes the background frame. In the case of ALEXIS, a separate background frame must be taken for every wavelength regime. Data from the plasma, in counts/s, was converted to radiance by multiplying it by the conversion number discussed above. The resulting spectrum is now plotted in Fig. 2.16a as radiance vs. wavelength. Usable wavelengths were identified. Exclusion criteria

included spectral lines being blended with other other spectral lines at the same wavelength, Einstein A coefficients with uncertainties over 10%, insufficient signal, and signal saturation. An experimental procedure was followed to find impurities from other species. A hydrogen plasma was made, and the spectrum was examined to find impurities. No impurities were found near the Argon wavelengths of interest. Einstein A coefficient uncertainty comes from the NIST database [31].

2.3.2 Neutral density calculation

Radiance flux refers to the amount of electromagnetic energy in Watts (W) emitted from a volume. It is wavelength specific, and is given as [8, 32]:

$$\begin{aligned}\phi_\lambda(i,j) &= n_i A_{i\to j} h\nu V_{plasma}\frac{d\omega}{4\pi} \\ &= n_i A_{i\to j} h\nu L_{plasma} A_{optics}\frac{d\omega}{4\pi}.\end{aligned} \tag{2.17}$$

The population of the upper level i of the transition producing the wavelength λ is given as n_i. The rate of spontaneous transition from upper level i to lower level j is the Einstein A coefficient $A_{i\to j}$. The energy associated with the transition is $h\nu$. The volume emitting the light is denoted here as $V_{plasma} = L_{plasma}A_{plasma}$. The light is emitted into the solid angle $\frac{d\omega}{4\pi}$.

The radiant flux is impractical for our uses because determining the solid angle into which the light is emitted can have large uncertainties. By contrast, radiance (L_λ) refers to the amount of energy transmitted, reflected, or received by a surface, and is given as [8, 32]:

$$L_\lambda(i,j) = \frac{\phi_\lambda(i,j)}{A_{optics}d\omega} = n_i A_{i\to j} h\nu L_{plasma}\frac{1}{4\pi}. \tag{2.18}$$

Eq. 2.18 can be rearranged to find the population of the excited state. For clarity we will use radiance for L_λ and L for plasma length.

$$n_i = \frac{4\pi \times radiance}{A_{i\to j} \times h\upsilon_{i\to j} \times L}. \tag{2.19}$$

Eq. 2.19 is used to obtain the density of the upper level i in the transition involved. Only two values are experimentally determined: radiance ($\frac{W}{cm^2 sr}$) is the area under the curve of the spectral line vs wavelength, and the observed size of the plasma is $L\,(cm)$. A factor of $4\pi sr$ is provided as a geometric term. The Einstein A coefficient, the rate of spontaneous decay from level i to level j, is $A_{i\to j}\,(\frac{1}{s})$. The energy of the transition is $h\nu\,(J)$.

Radiance was obtained separately for each wavelength through a python best-fit procedure to obtain the area under the curve.

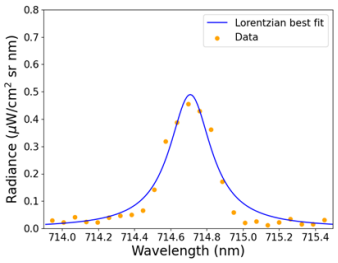

Figure 2.17: The Lorentzian best fit curve for 714.68 nm.

Fig. 2.17 shows an example fit for spectral data at 714.68 nm. The resulting integral found a radiance of $0.19 \times 10^{-6}\ \frac{\mu W}{cm^2 sr}$.

A CRM solver, discussed in Section 3.3, was used to calculate the ratio of the upper level population to the ground population, estimated to be the total neutral population due to its relative abundance. The upper level population was divided by the ratio of upper level to ground population to obtain the total neutral density:

$$n_0 = n_i \times \frac{n_0}{n_i} \tag{2.20}$$

2.3.3 Tests for sphere operation and calibration procedure

2.3.3.1 Steady-state nature of the integrating sphere

The sphere takes a certain amount of time to reach steady-state emission levels. Two experiments were performed to quantify this time.

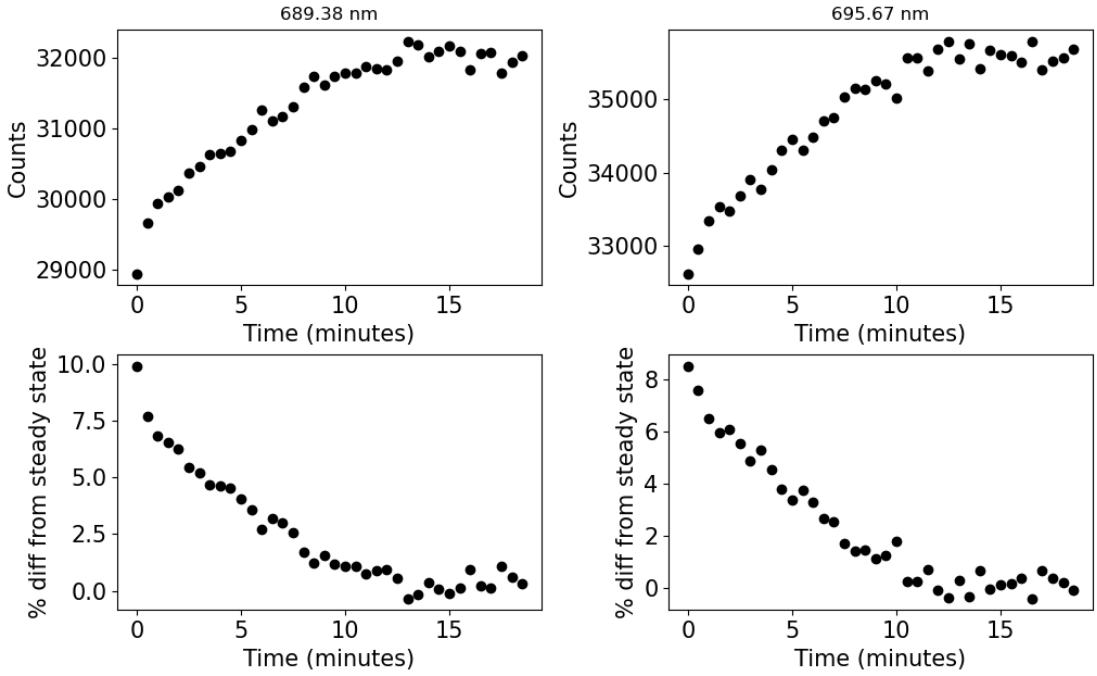

Figure 2.18: Raw data from spectrometer measuring sphere during start-up. Left column corresponds to 689.4 nm and right column corresponds to 695.7 nm. Top graphs correspond to raw data in counts from the spectrometer and bottom graphs correspond to % difference from steady state, where steady state is defined as the very last set of counts taken in this data set.

In order to test the time for the sphere intensity to reach steady state, an experiment was performed in which the spectrometer was set to obtain 20 frames every 30 seconds for 20 minutes, starting when the sphere was turned on. Two wavelengths are chosen at random to show the trend of the light levels over time. On the top is raw counts and on the bottom is % difference from steady state over time. It can be observed that the sphere takes approximately 15 minutes to reach steady state, reaching a slight peak first.

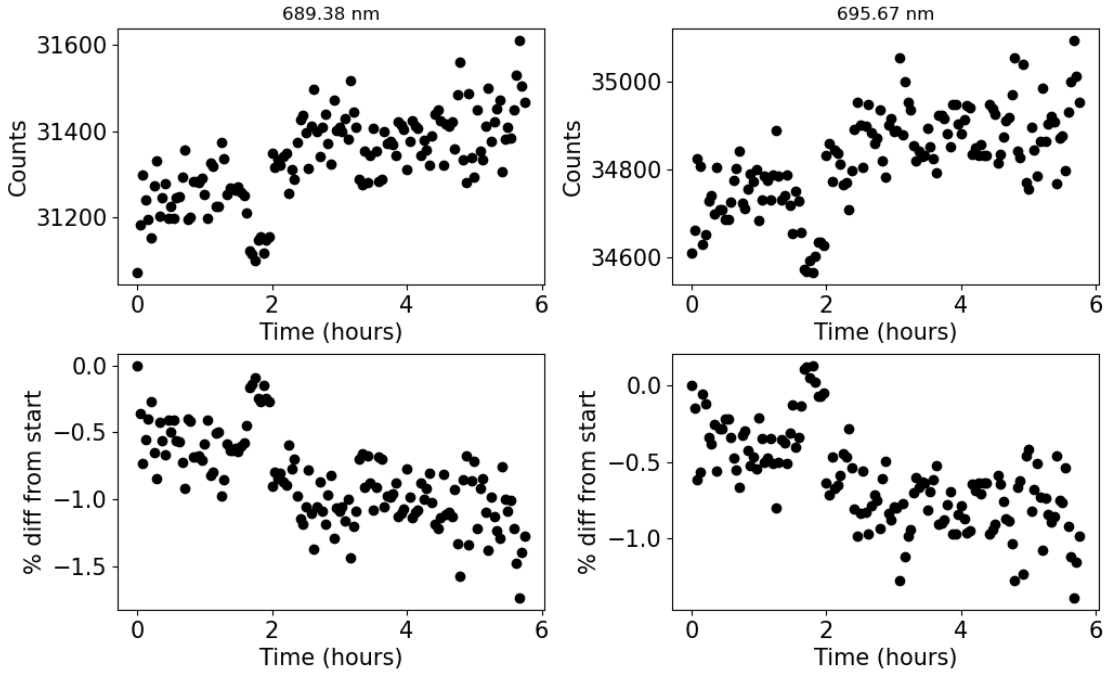

Figure 2.19: Raw data from spectrometer measuring sphere during steady-state. Left column corresponds to 689.4 nm and right column corresponds to 695.7 nm. Top graphs correspond to raw data in counts from the spectrometer and bottom graphs correspond to % difference from the beginning of measurement.

In order to test the change in sphere intensity over time, the spectrometer was set up to take 20 frames every 2.5 minutes for 6 hours after having left it on for 30 minutes. The counts measured over time are shown for two wavelengths in Fig. 2.19. The top graphs show raw counts. The bottom graphs show the % difference from the first point. A slight decrease in the number of counts measured is visible over time. This decrease appears to be no more than 2.5% which is less than the 10% error estimated on observed data.

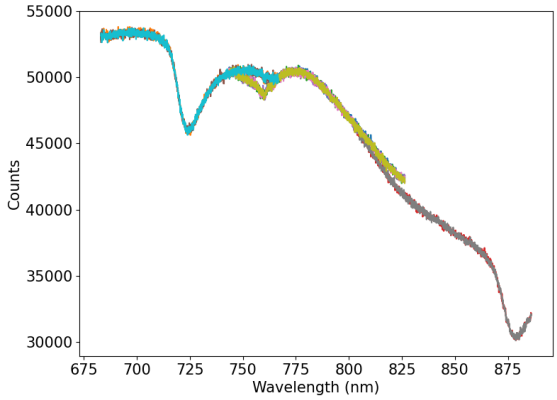

(a) Spectrometer reading when wavelength regime is not recalibrated, resulting in fiber not being adjusted.

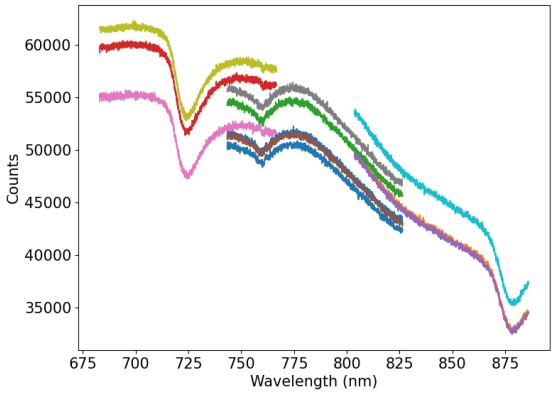

(b) Spectrometer reading when wavelength regime is both changed and and recalibrated, requiring fiber to be moved.

Figure 2.20: An analysis of adjusting the wavelength regime. Fig. 2.20a shows just the wavelength regime being changed whereas Fig. 2.20b shows the wavelength regime moved and recalibrated.

A final set of graphs, Figures 2.20a and 2.20b, demonstrate the delicate nature of the fiber setup. Fig. 2.20a demonstrates the results of moving the wavelength window without recalibrating either wavelength or intensity, and shows that both must be calibrated when the wavelength window is moved. By contrast, Fig. 2.20b mimics real data collection: the wavelength calibration is performed every time the wavelength window is moved. Disrupting the fiber enough to recalibrate the wavelength impacts the intensity calibration of the system by as much as 7%, meaning that an intensity calibration must be performed any time the fiber is moved. This change is accounted for in the calibration and so does not need to be accounted for in the error estimate, but emphasizes the need to recalibrate intensity when the wavelength calibration is performed.

2.3.3.2 Dependence of spectrum on distance from sphere

An assumption is made throughout the calibration procedure that the intensity will remain constant regardless of the distance of the lens from the sphere. Figs. 2.21 and 2.22 show the validity of this assumption.

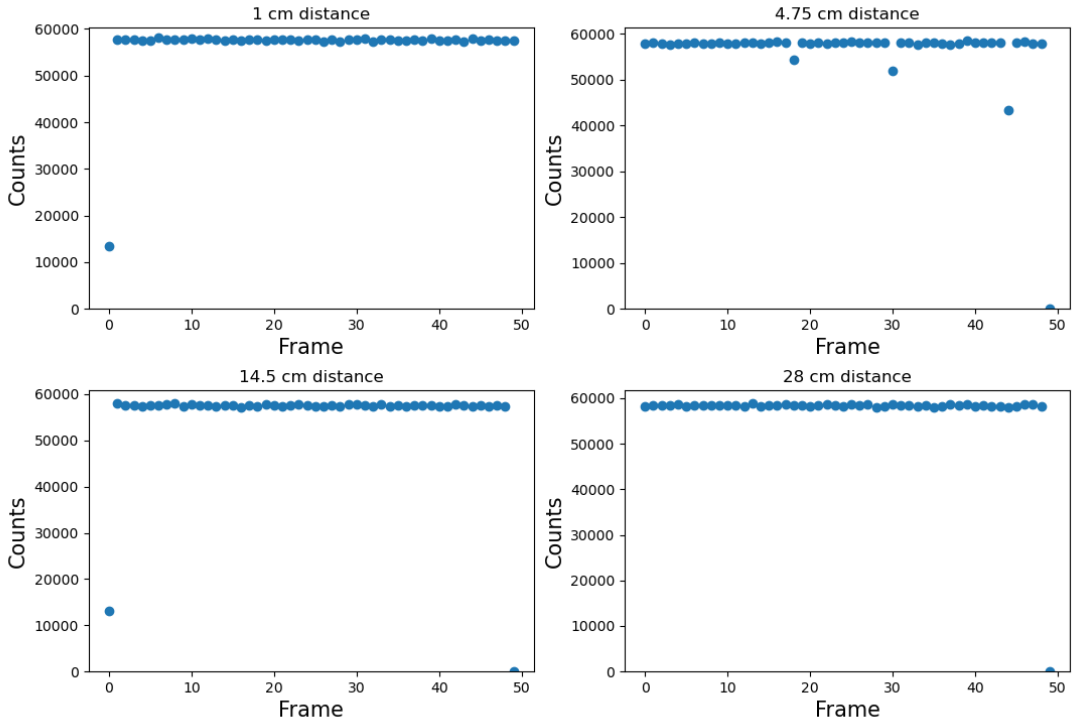

Figure 2.21: All frames taken during the process of checking the relationship between distance from sphere and counts.

Four distances between the lens and the sphere were tested, ranging from 1 inch to 28 inches. 50 spectra were taken for each lens position. The first and last frame of the spectrum did not reliably measure a consistent number of counts, so during actual calibration these frames are not used. Furthermore, several frames in one case produced anomalous counts. These were excluded from the analysis here, and during actual calibration the frames are inspected before use. The same 5 frames are excluded from every case for this analysis.

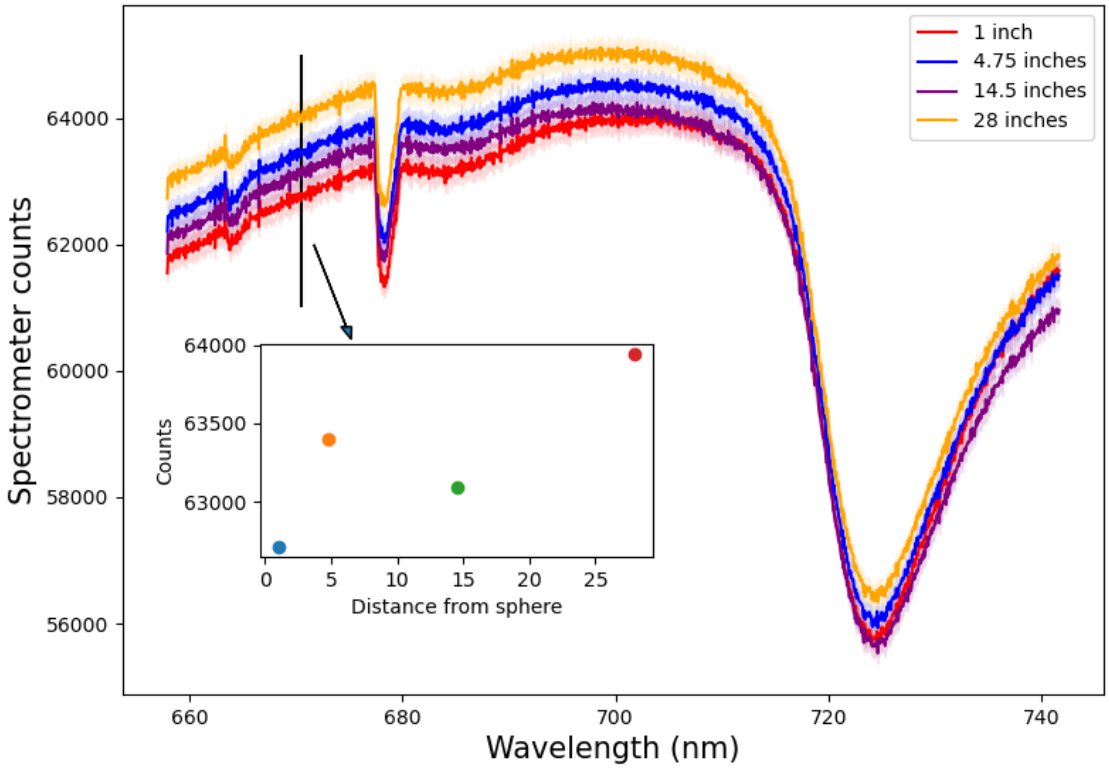

Figure 2.22: The main graph shows the average and standard deviation across spectra taken with lens at different distances from sphere. The inset graph demonstrates the relationship between counts and distance from the sphere for one wavelength, 670.5 nm, shown in black in the main graph.

The uncertainty is calculated as the standard deviation across the remaining 46 spectra. This uncertainty ranges between 0.2% and 0.4% of the total number of counts for all distances when excluding the three anomalous spectra shown in Fig. 2.22. The uncertainty for each distance is shown as shading in the figure.

The spectra in neighboring wavelength windows do not overlap in intensity perfectly. However, this is not deemed concerning for the following reasons. First, there is no trend in counts vs. distance from the spectrometer. Second, each of these spectra was taken with an adjustment of the fiber due to the need to correctly align the lens with every adjustment, and the small variation between distance results is consistent with the change

in intensity observed with movement in the fiber presented in Fig. 2.20b. This change is <0.1%, significantly less than the 7% seen in Fig. 2.20b associated with adjustment.

A dip in observed counts can exist within available spectra. An example of this can be observed in Fig. 2.22 at 680 nm. Two questions arise: what is it, and does it undermine the reliability of the wavelengths nearby? Most importantly, it is not an artifact arising from the lamp itself. It moves with the wavelength window, and appears with other light sources. It is not a problem with the spectrometer: it disappeared with a light source directly mounted on the spectrometer. It is not the fiber-optic because it appears with multiple different fiber-optic cables. The best existing guess is that it arises from the lens. In general it is determined to not be a concern: the calibration performed should remove the issue, and the good agreement observed between both synthetic and experimental data as well as across neutral densities experimentally confirms that it is not a concern.

2.4 The role of path length in electron and neutral density calculations on CTH

The equation used to estimate neutral density depends both explicitly and implicitly on the integration path length. The explicit dependence can be observed in Eq. 2.19. As estimated path length increases, the resulting estimated neutral density decreases. The implicit dependence arises from electron density measured through an interferometer, a measurement which requires the path length through the plasma [33]. This electron density dependence arises in the neutral density calculation through the CRM output as $\frac{N_j}{N_0}$. As estimated path length increases, estimated electron density decreases. This causes a decrease in $\frac{N_j}{N_0}$, which causes an increase in neutral density. Thus these two effects cancel to some degree. This section is an attempt to quantify the result.

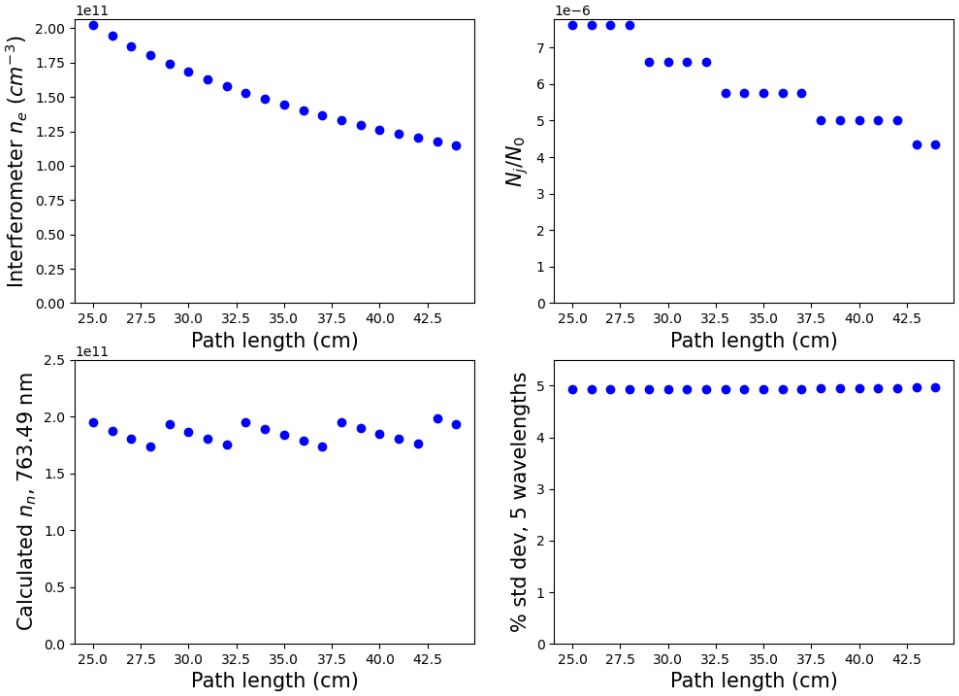

Figure 2.23: Upper left graph shows the electron density for varying path lengths. Upper right graph shows the resulting $\frac{N_j}{N_0}$ for that electron density for the upper level state corresponding to the emission line from 763.49 nm. Bottom left graph shows the neutral density with that electron density from 763.49 nm, with the appropriate path length for the neutral density. Bottom right graph shows the standard deviation across all available neutral densities. Actual plasma diameter is 37 cm.

Fig. 2.23 shows the impact of a change in path length or viewing chord on neutral density. Electron density decreases with an increase in path length. Only a finite set of electron densities have a calculated $\frac{N_j}{N_0}$, and that can be observed in the upper right graph, as $\frac{N_j}{N_0}$ decreases in a step-wise manner. That trend carries over to the calculation of neutral density. There is approximately a 10% change observed in the neutral density with a change in length, and most of that change is in the step-wise nature of the population calculation.

2.5 The ALEXIS experiment

Experiments were performed on ALEXIS for two reasons. First, there was a hope that the ability to use the pressure gauge in conjunction with plasmas on ALEXIS would make it an useful benchmarking experiment of the neutral density measurement. This was somewhat unsuccessful and is discussed in depth in Section 4.6.2. Additionally, as discussed above, ALEXIS discharges provide an environment for the exploration of the atomic physics of non-steady-state metastable states.

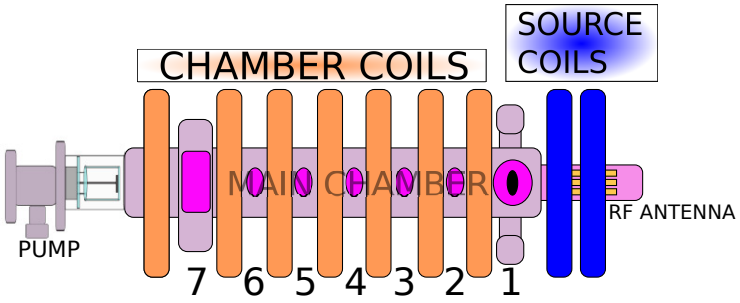

Figure 2.24: Diagram of the ALEXIS device.[16]

ALEXIS is a cylindrical plasma 91 cm long and 10 cm in diameter. Fig. 2.24 shows a diagram of ALEXIS from the side. Device ports are numbered. Locations 2 through 6 have QF-40 ports, with 4 ports located around the axis of the chamber for a total of 20 QF-40 chamber access points. Gas is injected through port 3 on top of the chamber. Pressure is measured through port 4, also on top. The spectrometer collects data through a lens pointed through a side window on port 3. A Langmuir probe is inserted into the ALEXIS chamber on port 4.

An RF antenna creates the plasma in the source portion of the chamber, and vacuum is maintained by a turbo pump at the opposite end of the device. Source magnetic coils surround the RF antenna region, and the chamber coils radially confine the ALEXIS plasma column.

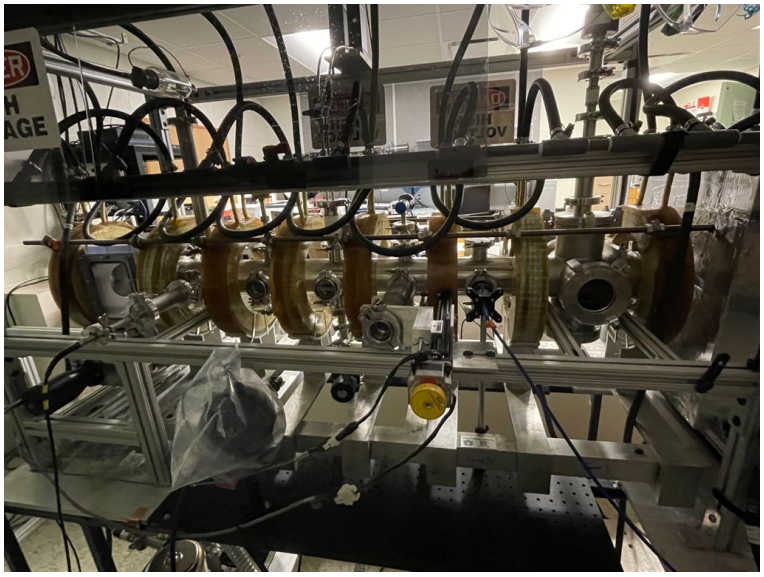

Figure 2.25: Full view of ALEXIS device.

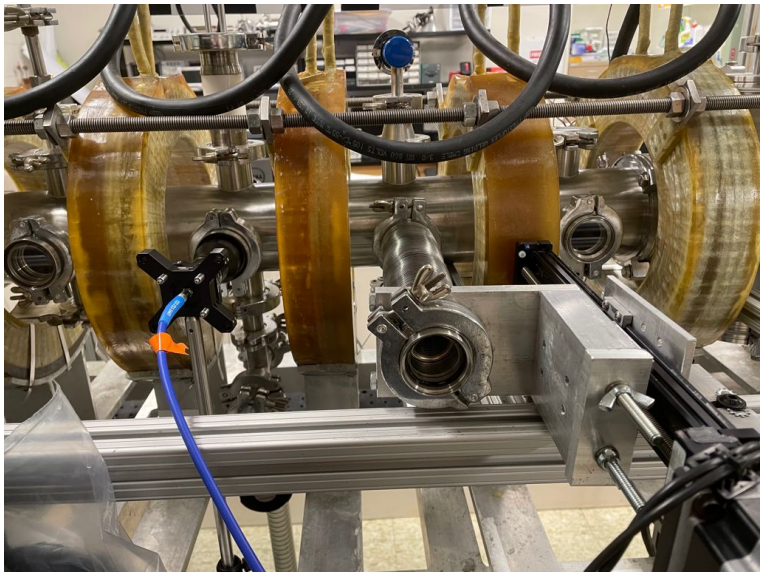

Figure 2.26: Close-up of ALEXIS. Main viewpoint visible is used for Langmuir probe measurements. The lens apparatus as well as blue fiber-optical cable can be seen on the left of the image.

A close up of ALEXIS is shown in Fig. 2.26. The spectrometer collects light emission from the blue fiber shown to the left. The blue pressure gauge can be seen on the top central port. The Langmuir probe was not installed when this picture was taken, but is typically up in the center, in the port to the right of the blue fiber-optic cable. The spectroscopic neutral

density is expected to be slightly lower than that taken from the pressure gauge measurement given that the spectrometer line of sight is closer to the pump and further from the source relative to the pressure gauge.

2.5.1 Pressure gauge

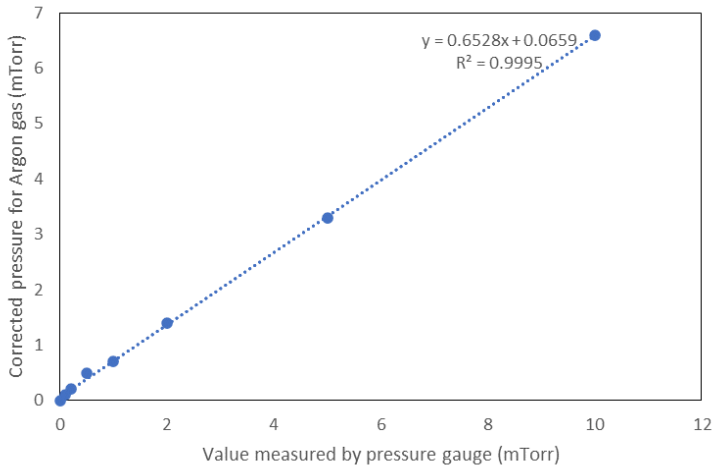

Figure 2.27: Pressure is measured by a convection gauge, and a gas-dependent conversion is necessary between the value provided by the gauge and the true value for the gas in question. x-axis shows the value provided by the gauge, y-axis shows the actual pressure for Argon gas.

Pressure is measured on ALEXIS through the use of a Convection Vaccuum gauge, series 275i. These gauges measure vacuum pressure by measuring the heat loss of a heated wire [34]. Gases conduct with different degrees of efficiency, so the gas used needs to be taken into account when determining the pressure. Fig. 2.27 shows the relevant conversion factor for Argon.

2.5.2 Langmuir probe analysis

The Langmuir probe on ALEXIS uses a swept bias voltage technique. This involves sweeping the bias voltage while simultaneously measuring the bias voltage and current collected by the probe tip. Electron temperature, electron density, and plasma potential can

then be extracted from this data through appropriate modeling of the current-voltage ($I-V$) curve [4].

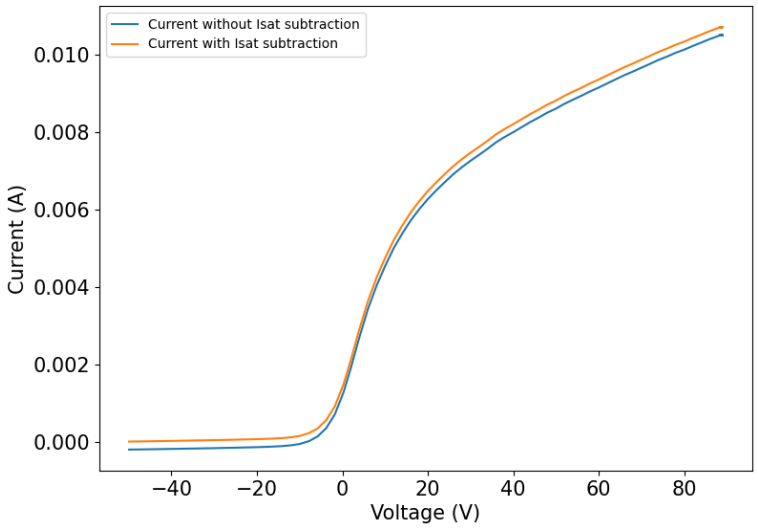

Figure 2.28: Current as a function of bias voltage for a Langmuir probe trace. The blue line shows the measured current and the orange line shows the current with ion saturation current subtracted.

Recall equation 2.8 [30]:

$$I_{probe} = -I_e \exp[\frac{q}{k_B T_e}(V_{probe} - V_p)] + I_{sat}.$$

In the case where $V_{probe} = V_f$, $I_{probe} = 0$ and so:

$$I_e \exp[\frac{q}{k_B T_e}(V_f - V_p)] = I_{sat}.$$

Solving for V_p results in:

$$V_p = V_f + ln(\frac{I_{sat}}{-I_e})\frac{k_B T_e}{q}. \tag{2.21}$$

Inserting the plasma potential v_p from Eq. 2.21 into Eq. 2.8 results in:

$$I_{probe} = -I_e \exp[\frac{q}{k_B T_e}(V_{probe} - V_f - ln(\frac{I_{sat}}{-I_e})\frac{k_B T_e}{e}] + I_{sat}$$

The exponent is separated into two components, isolating the natural log:

$$I_{probe} = -I_e \exp[\frac{q}{k_B T_e}(V_{probe} - V_f)] * exp[-ln(\frac{I_{sat}}{-I_e})] + I_{sat}.$$

This allows us to cancel out $exp(-ln)$:

$$I_{probe} = -I_e \exp[\frac{q}{k_B T_e}(V_{probe} - V_f)] * \frac{-I_e}{I_{sat}} + I_{sat}.$$

Saturation current is subtracted from both sides:

$$I_{probe} - I_{sat} = \frac{I_e^2}{I_{sat}} \exp[\frac{q}{k_B T_e}(V_{probe} - V_f)].$$

Natural log ln is taken of both sides:

$$ln|I_{probe} - I_{sat}| = \frac{q}{k_B T_e}(V_{bias} - V_f) + ln(\frac{I_e^2}{I_{sat}}).$$

Bias voltage is isolated by combining floating potential (V_f), electron current (I_e), and ion saturation current (I_{sat}), all constants in this context:

$$ln|I_{probe} - I_{sat}| = \frac{q}{k_B T_e} V_{bias} - (\frac{q}{k_B T_e} V_f - ln(\frac{I_e^2}{I_{sat}})).$$

Finally we arrive at the equation that allows us to compute the electron temperature:

$$ln|I_{probe} - I_{sat}| = \frac{q}{k_B T_e} V_{bias} - constant. \tag{2.22}$$

The raw current data from the probe, shown in orange in Fig. 2.28, is I_{probe}. The ion saturation current, the current from the region with low voltage, is represented by I_{sat}. This is the region in which current changes slowly with respect to voltage. The ion saturation current can be estimated as the current measured at the lowest voltage (i.e. furthest negative

voltages from zero) of data collected. In Fig. 2.28 this value is roughly 2×10^{-4} A, and the blue line in Fig. 2.28 is $I_{probe} - I_{sat}$. Note that because I_{sat} is a negative number, $I_{probe} - I_{sat}$ is equivalent to $I_{probe} + |I_{sat}|$. The electron temperature is $k_B T_e$ and the electron charge is q. The bias voltage is V_{bias} and V_f the floating potential. Eq. 2.22 then shows that electron temperature can be obtined by finding the inverse of the slope of the graph of $ln|I_{probe} - I_{sat}|$ vs. V_{bias}, shown in Fig. 2.29. Because q, $K_B T_e$, V_f, I_e, and I_{sat} are all constants, they will simply contribute to an offset rather than impacting the slope.

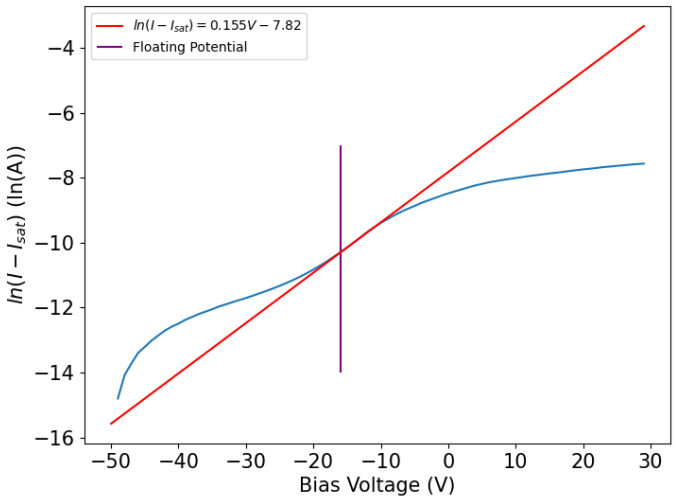

Figure 2.29: $ln|I_{probe} - I_{sat}|$ vs. V_{bias}. The slope of the linear portion of the graph is $\frac{1}{T_e}$.

Fig. 2.29 shows the relationship between $ln|I_{probe} - I_{sat}|$ and (V_{bias}). Near V=0 is a linear portion at which the slope is $\frac{1}{T_e}$.

Equation 2.15, used to measure electron density in the triple tipped Langmuir probe probe, can once again be used to measure electron in the single tipped Langmuir probe.

$$n_e = \frac{I_{sat}}{qA_{eff}} \exp(1/2)\sqrt{\frac{M}{K_B T_e}} = 4.25 \times 10^{17} \times \frac{I_{sat}}{\sqrt{T_e}}$$

The ion saturation current is I_{sat}. The Langmuir probe collection area is A_{eff}, which in this experiment is assumed to be the vacuum-exposed surface area of the cylinder as well as the whole tip. The radius of the cylinder is 2.68×10^{-3} m and the length 7×10^{-3} m, which

makes area $1.4 \times 10^{-4}\,\mathrm{m}^3$. The electron charge is q, $1.6 \times 10^{-19}\,\mathrm{C}$, and M is the ion mass, $6.63 \times 10^{-26}\,\mathrm{kg}$ for single ionized Argon. Eq. 2.15 shows the electron density for each probe trace using this probe in an Argon plasma. The electron density calculation depends on the electron temperature as seen in the above equation.

2.6 Uncertainty propagation

There are a range of items for which uncertainty needed to be determined throughout this thesis. In particular, data from the triple probe, spectrometer, Langmuir probe, neutral density, spectroscopic data, and synthetic data all required accompanying uncertainties. The data from the interferometer is determined to have an uncertainty of 10%. This is supported by the noise level in raw signal from the interferometer. An example of this raw signal can be observed in Fig. 2.30. The signal is smoothed for use in analysis through a Savitzky-Golay filter with a smooth parameter of 301.

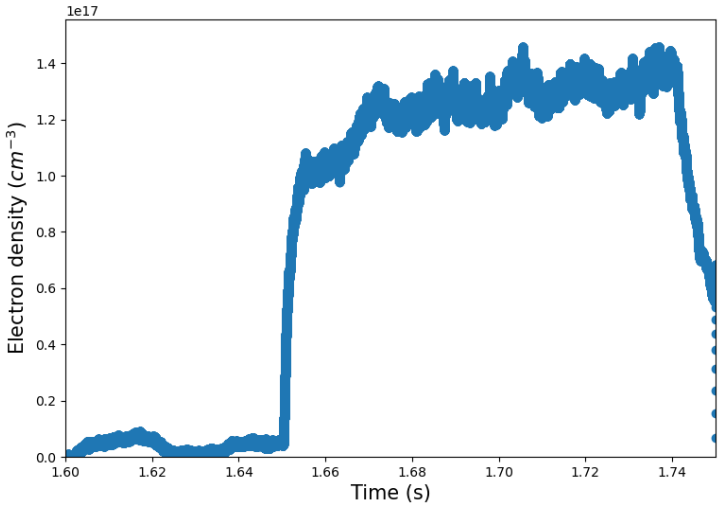

Figure 2.30: Raw data from the interferometer shown to demonstrate noise levels

The triple probe data is determined to have an uncertainty of 25%. Like the interferometer, this is supported by the level of noise in the raw signal, shown in Fig. 2.31.

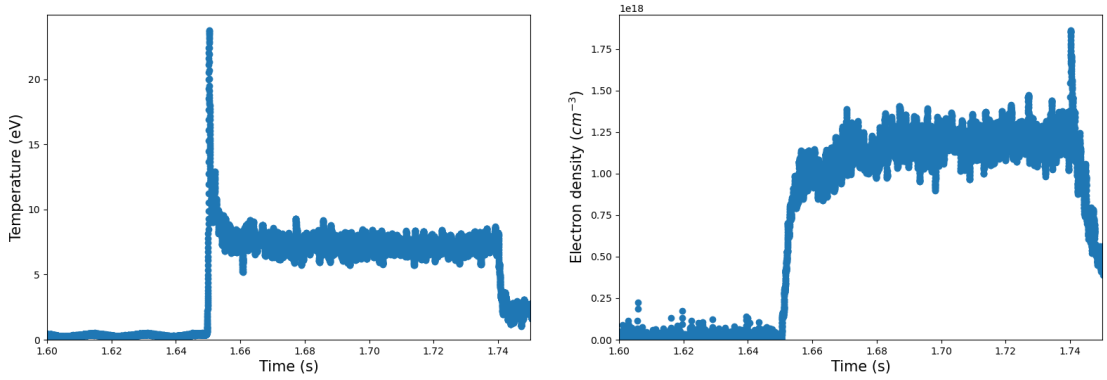

(a) Raw data from the triple probe shown to demonstrate noise levels in electron temperature data.

(b) Raw data from the triple probe shown to demonstrate noise levels in electron density data.

Figure 2.31: Uncertainties for the interferometer and triple probe.

As discussed in Section 2.2.2.1, the triple probe electron density measurement suffers from error beyond that of noise. Two examples are imperfect collection area measurement and practical collection area changes with changes in the size of the plasma sheath as plasma parameters change. In general, the triple probe electron density measurement will only be used to investigate radial profile behavior.

Determining uncertainty for spectroscopic data proved difficult. The main unit is "counts", so a Poisson approach to uncertainty is intuitive. Unfortunately, the number of counts was typically between 20,000 and 60,000, rendering any uncertainty from this source negligible. The uncertainty from the radiance calibration provided little more uncertainty: the uncertainty in the range of interest had a maximum value of 1.7% at 400 nm. The connection between the fiber-optic cable and the spectrometer was found to be extremely delicate, as can be observed in Fig. 2.20b. This was found to introduce error of up to 7%. In the end, a value of 10% was chosen for the uncertainty of the spectral lines. This is consistent with other sources, including Sciamma [35], Arnold [16]. It is also likely an overestimate. This value will be used when comparing synthetic and experimental line ratios.

All synthetic spectral line intensities were given the uncertainty associated with the Einstein-A coefficient from NIST [31]. This is likely an under-estimate as there is some

degree of uncertainty associated with the rate coefficients used, but quantifying these is outside the scope of this thesis.

Estimating the neutral density uncertainty proved a challenge. A conventional approach would have been to combine the uncertainties of the individual components. This would have included the result of the CRM, the Einstein A coefficient, and the radiance calculation. One major drawback to this option lies in the difficulty in estimating the uncertainty of the CRM. There is no existing systematic generation of uncertainties of atomic models, and estimating those uncertainties is beyond the scope of this work. There is a project underway at Auburn to investigate these uncertainties, so a future project may be able to use them.

The approach used instead was to take advantage of the standard deviation in the neutral densities from the set of spectral lines use in the analysis, each line giving a separate neutral density. The range of standard deviations is shown in Fig. 4.25, but 93% of the frames represented in this thesis have an uncertainty under 20%. This approach provides an uncertainty estimate that depends on the specific plasma to a degree beyond an approach that combines uncertainties.

A final approach was taken to examining the impact of the electron temperature and density on the neutral density. One frame was examined: the frame near time 1.72 s in shot number 21101229.

ne ↓ Te →	-25%	2.97	+25%
-10%	$1.12 \times 10^{12} \pm 11.26\%$	$6.58 \times 10^{11} \pm 12.33\%$	$2.96 \times 10^{11} \pm 13.75\%$
1.19×10^{12}	$1.37 \times 10^{12} \pm 11.45\%$	$5.98 \times 10^{11} \pm 12.49\%$	$2.38 \times 10^{11} \pm 13.86\%$
+10%	$1.25 \times 10^{12} \pm 11.63\%$	$5.43 \times 10^{11} \pm 12.64\%$	$2.12 \times 10^{11} \pm 13.96\%$

Table 2.2: The neutral density calculation requires a measurement of the electron temperature and density through the collisional radiative model. This table shows the neutral density with the range of electron temperatures provided by their uncertainties. All densities have units of cm^{-3} and all temperature have units of eV.

Fig. 2.2 shows the result of varying the electron density from the interferometer and the electron temperature from the triple probe within the bound given as their uncertainties. For this plasma, an increase in measured electron temperature results in a decrease in estimated neutral density. An increase in measured electron density has differing results depending on the electron temperature, but typically results in a decrease in neutral density, although not to the same extent as the electron temperature. In general, the electron temperature and density do have an impact on the neutral density.

Chapter 3

Atomic Physics

3.1 Introduction

The neutral density diagnostic, whose implementation is the goal of this thesis, relies on a calculation of the population of excited states of Argon, obtained through an atomic model. The atomic models presented here require previously calculated accurate atomic transition rate coefficients. The neutral Argon rates are calculated by Arnold [16], and the singly ionized Argon rates were calculated by Griffin et al. [36], both using a non-perturbative method known as the R-matrix approach. The atomic models that predict the excited state populations needed for the neutral density diagnostic depend on electron temperature, electron density, and the populations of metastable states within the plasma.

As discussed in the previous chapter, the two experiments used for this thesis differ in electron density as well as chamber size. The higher electron density in CTH allows the ground and metastable populations within neutral Argon to reach a steady state value on a quicker time-scale than in lower density plasmas. The large size of CTH ensures that neutral Argon atoms do not hit the wall in the steady-state time of the metastable states, allowing neutral Argon spectra on CTH to be modeled in a steady state metastable fashion. By contrast, the lower electron density, combined with the smaller chamber size, on ALEXIS likely does not allow neutral Argon metastable populations to reach steady state before neutral particles hit the wall. As a result, ALEXIS Argon spectra must be modeled in a time-dependent fashion.

This contrast is shown in Fig. 3.1 which shows the time dependent populations of the lowest 5 energy levels of Argon for CTH-relevant plasmas (Fig. 3.1a) and ALEXIS-relevant plasmas (Fig. 3.1b).

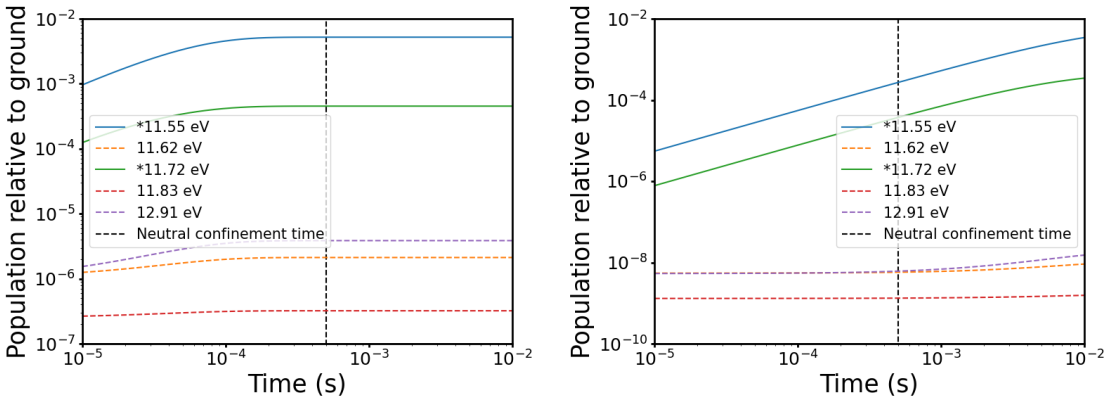

(a) CTH population vs time

(b) ALEXIS population vs time

Figure 3.1: Populations of both CTH and ALEXIS plasmas over time, along with the neutral Argon confinement time on both devices. Atomic populations have hit steady state before particles begin hitting the wall on CTH, whereas metastable populations on ALEXIS are still in flux when particles hit the wall.

The vertical line in the case of the CTH population plot shows the characteristic time of the plasma: data collection occurs on CTH between 10 and 100 ms, by which point all states have hit a steady-state population. The vertical line in the case of the ALEXIS graph shows a typical time-to-wall. This shows that the neutral particles hit the wall well before the metastables have time to hit steady-state.

This chapter will detail the atomic physics background and atomic modeling approach used for the neutral density diagnostic. Metastable states will be described. Synthetic data for neutral Argon has been found to match experimental data on both CTH and ALEXIS, justifying the use of the model. Synthetic data for singly ionized Argon has been found not to match experimental data on CTH, and this will be explored in this chapter.

3.2 Population modeling

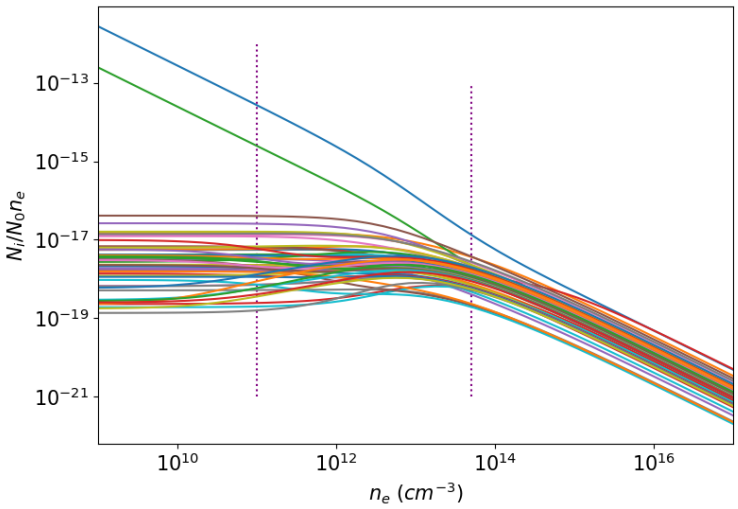

Figure 3.2: Representation of regimes in T_e, n_e and time parameter space relevent to CTH. dotted vertical lines show the different regimes, with Coronal Equilibrium occupying the lowest electron density, CR occupying the middle, and Local Thermodynamic Equilibrium occupying the highest electron density.

There are three density regimes that can be used to describe the results of an atomic population model: Local Thermodynamic Equilibrium (LTE), the Collisional-Radiative regime (CR), and the Coronal regime. These regimes are characterized by the role of collisions that redistribute the excited populations. At very low electron densities, the Coronal regime, the excited states are population by excitation from the ground state and radiatively decay before collisonal-redistribution can occur. By contrast, at very high electron densities, the LTE regime, the collisions that cause transitions between excited states drive the populations to their Local Thermodynamic Equilibrium values. In the intermediate regime, the CR regime, some collisional redistribution is important. It should be noted that Collisional-Radiative theory (described in Section 3.3) describes all three regimes, so the code used in this dissertation is applicable in all three cases.

Metastable states are fully described in Section 3.6, but in brief they are energy levels in Argon for which spontaneous radiative decay to ground is forbidden, and so the population

of those levels becomes large compared to that of the other excited states. The lower spontaneous emission rate coefficients of metastable states means that their populations may have to be modeled time-dependently. Additionally, their populations can sometimes be described by a different "regime" than the excited states. Fig. 3.2 shows the populations of neutral Ar relative to the ground population as a function of electron density. In a figure such as Fig. 3.2, Coronal populations are flat in their slope, LTE populations have a slope of -1, and the C-R regime bridges the region between these two. The green and blue lines represent the populations of the two metastable states. While the excited states are in Coronal conditions at the lowest electron densities, the two metastable states appear to be closer to LTE in their behavior.

So far the assessment of populations within the plasma has focused on the dependence on n_e, but a focus on the time dependence of populations is also crucial. In the case of neutral Argon for CTH plasma conditions, the time to reach steady state is significantly shorter than the timescale of the plasma. In the case of singly ionized, the steady state timescale is roughly the same timescale as the plasma. In the case of singly ionized this suggests that the metastable population must be incorporated into the final CRM, along with electron temperature and electron density. In the case of neutral Ar on ALEXIS, it is likely that plasmas have not had sufficient time to reach steady state conditions, so time-dependent modeling is required.

3.3 Collisional Radiative Modeling

Collisional Radiative Modeling is an approach to atomic model that was introduced in 1962 by Bates et al. [37]. It was further developed in 2006 by Summers et al. [38] to include the role of metastable states, and the Atomic Data and Analysis Structure (ADAS) was created to use the Generalized Collisional-Radiative (GCR) framework to facilitate the plasma atomic modeling [39] and has its own Collisional Radiative Model solvers. The Collisional Radiative Model solver used for this thesis is ColRadPy, developed by Johnson

et al. [40], but there are other available solvers. These include CRModel, developed by Hartgers et al. [41] as well as Flexible Atomic Code (FAC) developed by Gu [42].

CRM is an approach to modeling in which the population of a given state is obtained with knowledge of the rate at which atoms enter and leave any state.

$$\frac{dN_i}{dt} = -n_e \sum_{j \neq i} (q^e_{i \to j} + S_i) n_i + \sum_{i>j} (n_i A_{i \to j}) + \sum_{j>i} (n_j A_{j \to i}) + \sum_{j \neq i} (n_e q^e_{j \to i} n_j) + n_e \sum_k (R_{\nu_k \to i} n_{\nu_k}) \tag{3.1}$$

Eq. 3.1 describes the time dependent nature of a state i. Of the three terms, the first term shows all the mechanisms for population loss from level i, the second terms show all the mechanisms for population gain to level i, both through spontaneous transition (A) and through electron impact transition (q), and the third term shows the recombination into state i from metastables of the next higher charge state. The Einstein A coefficient ($A_{i \to j}$) is a de-excitation term only: j must be larger than i. The electron impact excitation and de-excitation is $q^e_{i \to j}$ and $q^e_{j \to i}$: an electron collides with an atom in state i, resulting in the excitation of the atom from state i to state j, or collides with an atom in state j, de-exciting it to state i. It depends on both n_e and n_i because the transition requires collisions between the two. The electron impact ionization rate is S_i: an electron collides with an atom in state i, resulting in the ionization of the atom from state i. Again, it depends on both n_e and n_i because the transition requires collisions between the two. The spontaneous transition rate, also known as the Einstein A coefficient, is $A_{j \to i}$: an atom spontaneously loses energy (emitted as a photon with a corresponding wavelength) to drop from state j to i. This does not require a collision and thus only depends on n_j. The recombination rate is $R_{\nu_k \to i}$: an electron recombines with an ion and the ion with the electron enter state i. It depends on both n_e and n_{ν_k} because it requires a collision between both, and includes radiative, dielectronic, and three-body recombination. Metastable levels of the next higher charge states are denoted ν_k.

Each level in the atom is separately described by Eq. 3.1, including ground and singly ionized. Thus we have a set of coupled differential equations, with one equation for each level being modeled. The only assumptions made so far are the ways by which it is possible for an atom to enter or leave state i. These electron-impact and spontaneous processes should be sufficient to model the emission for our plasma conditions. Additional atomic processes can be added to the model in the case of plasmas when relevant. Next, collisional-radiative equations are addressed.

The next step is to turn the set of equations into a matrix that includes equations representing all states that are not ground or metastable. The first step is to define a matrix that combines all the rates involved [43]:

$$C_{ij} = -\Big(\sum_{j\neq i} n_e q_{i\to j} + n_e S_i + A_{i\to j}\Big) N_i + \sum_{j\neq i} (A_{j\to i} + n_e q_{j\neq i}) N_j. \tag{3.2}$$

With this matrix defined, the Collisional Radiative matrix equation can be defined [43]:

$$\begin{pmatrix} dN_0/dt \\ dN_{\sigma_1}/dt \\ dN_3/dt \\ \dots \\ dN_n/dt \\ dN_{\nu_1}/dt \end{pmatrix} = \begin{pmatrix} C_{00} & C_{0\sigma_1} & C_{03} & \dots & C_{0n} & R_{\nu_1 0} n_e \\ C_{\sigma_1 0} & C_{\sigma_1\sigma_1} & C_{\sigma_1 3} & \dots & C_{\sigma_1 n} & R_{\nu_1\sigma_1} n_e \\ C_{30} & C_{3\sigma_1} & C_{33} & \dots & C_{3n} & R_{\nu_1 3} n_e \\ \dots & \dots & \dots & \dots & \dots & \dots \\ C_{n0} & C_{n\sigma_1} & C_{n3} & \dots & C_{nn} & R_{\nu_n n} n_e \\ n_e S_0 & n_e S_{\sigma_1} & n_e S_3 & \dots & n_e S_n & -\sum_n R_{\nu_1 n} n_e \end{pmatrix} \begin{pmatrix} N_0 \\ N_{\sigma_1} \\ N_3 \\ \dots \\ N_n \\ N_{\nu_1} \end{pmatrix} \tag{3.3}$$

Within Eq. 3.3, N_0 refers to the ground state population, N_{σ_1} refers to the lowest metastable state, and N_{ν_1} refers to the metastable of the next (higher) ionization state. Ar I has two

metastable states, only one of which is reflected in the notation shown here. S refers to the ionization rate coefficient and R to the recombination rate coefficient. This matrix can be solved through a matrix solver, assuming knowledge of the rates shown. There are two outputs from the matrix that are used for this thesis. The first is a set of Photon Emissivity Coefficients (PECs), defined in Eq. 3.4, that can be used as a synthetic spectra.

$$PEC^{\sigma}_{i\to j} = A_{i\to j} \times \frac{N^{\sigma}_{i}}{N_{\sigma}} \tag{3.4}$$

where $N^{\sigma_k}_i$ is the contribution to N_i from a highly populated state σ, either ground (N_0), metastable(σ_1, σ_2), or the ground or metastable states of ionized (ν_k). The CRM provides $\frac{N_i}{N_{\sigma_k}}$. The Einstein A coefficient from level i to level j is given as $A_{i\to j}$ and is available from NIST [31]. The PECs can then be compared to experimental spectra through normalization:

$$\frac{I_{i\to j}}{I_{i'\to j'}} = \frac{PEC^{0}_{i\to j} + PEC^{\sigma_1}_{i\to j}\frac{N_{\sigma_1}}{N_0} + PEC^{\sigma_2}_{i\to j}\frac{N_{\sigma_2}}{N_0} + PEC^{\nu_1}_{i\to j}\frac{N_{\nu_1}}{N_0}}{PEC^{0}_{i'\to j'} + PEC^{\sigma_1}_{i'\to j'}\frac{N_{\sigma_1}}{N_0} + PEC^{\sigma_2}_{i'\to j'}\frac{N_{\sigma_2}}{N_0} + PEC^{\nu_1}_{i'\to j'}\frac{N_{\nu_1}}{N_0}}. \tag{3.5}$$

A comparison between the experimental and synthetic spectra can validate the use of the atomic model.

The other matrix output that is used here is relative population ratios, $\frac{N_i}{N_0}$, used to estimate neutral density. The absolutely calibrated spectrometer produces the population of an excited state, described in Section 2.20, and the population ratio is then used to estimate the neutral density.

Atomic transition rates are crucial to the atomic model within this thesis. Two atomic datafiles are used heres: an ADF04 file for Ar I, created and described in detail by Arnold [16] and an ADF04 file for Ar II, similarly created and described by Griffin et al. [36]. Both are R-matrix with pseudostates calculations for the purpose of obtaining electron impact excitation rate coefficients. A synthetic dataset produced by a model using the Ar I datafile is compared to an experimental spectra in Fig. 4.23. In the case of the Ar I file, Einstein A-coefficients are produced in the creation of this data file but replaced by NIST [31] A-values

where available. The Ar II ADF04 file was LS-resolved due to computational limitations at the time. Thus, for Ar II the LS coupling scheme is used, but there was no J-resolution to the data, and it was an open question (addressed in Section 3.8) as to whether LS resolution is sufficient to model Ar II spectral lines, or whether a new atomic dataset that is LSJ resolved is required. This open question has since been resolved: the LS resolution is insufficient for both experiments represented here, and this work has become a partial impetus for the calculation of a new, LSJ resolved datafile by collaborators at Queens University Belfast.

Finally, Collisional Radiative Modeling can also be performed time-dependently, in a context in which any or all the levels have not reached steady state. There are two circumstances represented in this thesis under which a plasma must be modeled time-dependently. The first scenario is that in which the plasma does not last long enough for metastable states to reach steady-state, a circumstance which occurs for Ar II on CTH and a contributing factor for why LS rates are insufficient. The second scenario is that atoms hit the wall, returning excited state electrons to ground, a circumstance which occurs on ALEXIS and the results of which are described in Section 4.6.3.

3.4 Angular momentum

Angular momentum is one of the most important quantities in atomic systems, hence it is valuable to consider angular momentum coupling in some detail. Electrons within atoms sit in "shells" described by n orbitals and k electrons. Each electron has an orbital angular momentum l_k, which can range as an integer from $0 \leq l \leq n-1$. It also has a spin angular momentum quantum number s_k which is $1/2$, with an associated magnetic spin quantum number that can be $-1/2$, or $+1/2$. l_k and s_k for an electron then combine for total angular momentum of j_k. Electrons are fermions, possessing anti-symmetric wavefunctions. A consequence of this fact is the Pauli Exclusion principle: no two electrons in the same nl-subshell can have the same set of n, l, m_l, s, and m_s quantum numbers.

Coupling schemes describe the addition of electron atomic angular momenta within an atom, and Russell-Saunders coupling (also known as LS coupling) is the most common for light elements. The valid angular momenta of two individual electrons are then described by the following equations:

$$\begin{aligned} |l_1 - l_2| \leq L \leq l_1 + l_2 \\ 0 \leq l_r \leq n - 1, \end{aligned} \tag{3.6}$$

$$\begin{aligned} |s_1 - s_2| \leq S \leq s_1 + s_2 \\ s_r = 1/2. \end{aligned} \tag{3.7}$$

Angular momentum can then be added for any number of electrons by combining those already combined with another:

$$|L - S| \leq J \leq L + S \tag{3.8}$$

.

These quantum numbers are written concisely for the full atom as:

$$^{2S+1}L_J \tag{3.9}$$

L angular momentum of integer value is described through letters. S means $L = 0$, P means $L = 1$, D means $L = 2$, F means $L = 3$, etc. Lower case letters describe individual electrons whereas upper case describe the state of the total atom.

3.5 Atomic level labeling

There are three labeling schemes used in this thesis for labeling Argon atomic levels. The first is Racah notation, owing to its common use in the literature when labeling neutral Argon energy levels. The second is the energy of the level relative to ground, because this provided a useful means of labeling the levels that is independent of the coupling scheme

and could be used in the analysis of Collisional Radiative code output to extract transitions. A third scheme, LS-coupling (described above), is used to identify levels in the input file of containing all of the rate coefficients used in the atomic Collisional Radiative Model described in Section 3.3. The Racah and LS coupling schemes produce the same total angular moment J. The difference arises in the order in which the contributing angular momentum is added.

Racah notation is used by the National Institute of Standards and Technology (NIST) in their labeling of neutral Argon energy levels. We use this database of atomic levels and transitions in this work and it is a vital component of the work [31]. Racah notation separates the atom into the core (unexcited) electrons and the excited electron. The core electrons are described through Russell Saunders notation to give a total L_1, S_1, and J_1 for the electron angular momentum coupled up to that point. The core is then combined with the excited electron to describe the full atom.

$$\begin{aligned} n_{core}l_{core}(^{2S_1+1}L^o_{1_{J_1}})n_{outer}l_{outer}[K]^o_J \\ K = J_1 + l \\ J = K + s \\ s = 1/2 \end{aligned} \tag{3.10}$$

Eq. 3.10 shows Racah notation as used by the NIST database [31].

1. The $n_{core}l_{core}$ structure of the core is described first. In the case of neutral argon this is most commonly $3s^2 3p^5$. In addition to the n and l values, the electron population of each n_{core} and l_{core} is outlined. This provides information about the core electrons which will then allow the reader to see which outer electron is going to be coupled to the core.

2. $(^{2S_1+1}L^o_{1_{J_1}})$: LSJ of the core.

3. The $n_{outer}l_{outer}$ values of the excited electron is described next.

4. The last piece describes the angular momentum of the excited electron. $K = J_1 + l$ and $J_{total} = K + s$. If K is an integer it can be represented by the appropriate letter. If not it is represented with fractions. The "parity" of the total wave function is represented by o: o indicates odd parity, whereas the lack of o indicates even parity.

This thesis primarily uses energy difference from the ground level of an ionization state to label levels as information about the atomic physics of a level is rarely needed. When necessary, Racah notation will also be used. This is in part because J values are relevant to this work and in part because this is the notation scheme preferred by NIST [31]. Table 3.1 can be used to more easily convert between energy levels and Rach notation for the lowest 12 energy levels of neutral Argon.

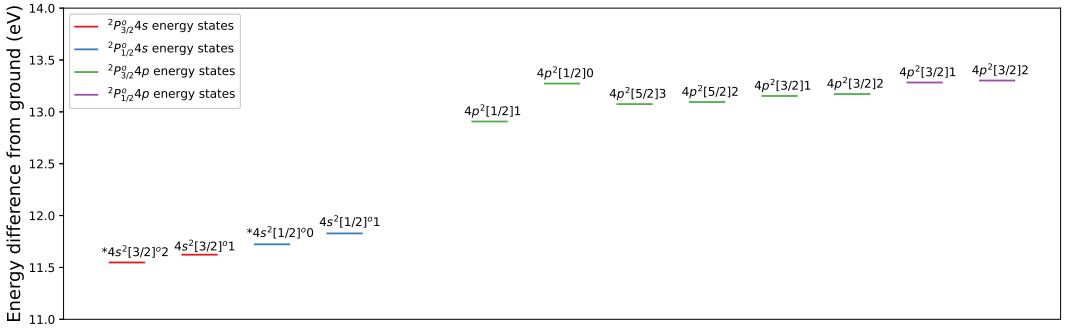

Figure 3.3: Energy levels and J values for lowest 12 energy states of neutral Argon, all energy states in the $^2P^o_{3/2}4s$ states (red), $^2P^o_{1/2}4s$ states (blue), $^2P^o_{3/2}4p$ states (green), and $^2P^o_{1/2}4p$ states (purple). Metastable states are 11.548 eV and 11.723 eV, and both are labeled with *. Every level is labeled in the format: $nl^{2s+1}[K]^oJ$.

Energy level (eV)	Energy level (cm^{-1})	Racah notation
11.548	**93143.76**	$4s^2[3/2]^o2$
11.623	93750.60	$4s^2[3/2]^o1$
11.723	**94553.66**	$4s^2[1/2]^o0$
11.828	95399.83	$4s^2[1/2]^o1$
12.907	104102.10	$4p^2[1/2]^o1$
13.273	107054.27	$4p^2[1/2]^o0$
13.076	105462.76	$4p^2[5/2]^o3$
13.095	105617.27	$4p^2[5/2]^o2$
13.153	106087.26	$4p^2[3/2]^o1$
13.172	106237.55	$4p^2[3/2]^o2$
13.283	107131.71	$4p^2[3/2]^o1$
13.302	107289.70	$4p^2[3/2]^o2$

Table 3.1: Lowest 12 energy levels of Argon I. Energy in eV and cm^{-1} are both shown, along with Racah notation.

3.6 Definition and importance of metastable states

Metastable states are states for which there are no allowed (electric-dipole) transitions to lower levels, making transition out of a metastable state infrequent. Electric-dipole transition rules are outlined in Fig. 3.2.

Allowed (E-dipole)	Forbidden (E-quadrupole)	Forbidden (M-dipole)
$\Delta J = 0, +/-1$ (not 0-0)	$\Delta J = 0, +/-1, +/-2$ (not 0-0, 1/2-1/2, 0-1)	$\Delta J = 0, +/-1$ (not 0-1)

Table 3.2: Main atomic transition rules. E-dipole transitions are "allowed" and represented by atomic transition rates. E-quadrupole are less common than E-dipole, and M-dipole are "forbidden". Note that "forbidden" here is a technical term: these transitions occur, but rarely.[44]

The low rate of radiative decay for metastables states results in them becoming more highly populated than a typical excited state. It can also mean that their populations evolve slowly relative to the populations of other excited states, often similar to the timescale of plasma dynamics. This means that time-dependent modeling of ground and metastables populations may be required [45, 21, 22]. It also means that an analysis of time-dependent populations can be used to identify metastable states. Where a normal excited state would have a steady-state population that is very small compared to the ground population (typically millions of times smaller), a metastable state will have a population closer to that of the ground population and much greater than the non-metastable excited states.

The metastable level of Argon with the lowest energy and the highest population has an energy of 11.54 eV relative to ground, and the other metastable state has an energy of 11.72 eV relative to ground. The energy of these two metastables states has an important consequence for Argon spectroscopy. Transitioning from 11.54 eV or 11.72 eV to higher energy states is straightforward in the low temperature plasmas represented here, whose electron temperatures range from 2 to 10 eV. By contrast, electron excitation from ground to the excited states requires an electron with a much higher energy. As a result, small changes in the population of metastable states have a large impact on the populations of other states, and so quantifying metastable population is important to quantifying the populations of all other states.

3.7 Optical thickness tests

The use of spectroscopy as a diagnostic assumes that all photons emitted from a plasma are able to escape. The case where photons are absorbed to a noticeable degree is known as being "optically thick". Since our main neutral density diagnostic is used on CTH, we check whether the neutral Argon emission is likely to be optically thick for CTH conditions.

The photons can only be absorbed if a transition is readily available according to atomic physics selection rules between the electron with which the photon collides and the energy

Wavelength Ratio	Upper level energy	Lower level energies	A ratio	Real intensity ratio
696.54/727.24	13.33 eV	11.548 ev*/11.623 eV	3.5 +/- 0.49	3.52 +/-.10027
480.33/500.99	19.22 eV	16.64 ev/16.75 eV	5.17 +/- 0.67	4.76 +/- 0.7

Table 3.3: Optical thickness assessment on CTH. The ratio of intensities from the wavelengths $\frac{696.54}{727.24}$ is used to check optical thickness, whereas the ratio $\frac{480.33}{500.99}$ is used to check the validity of the process.

difference above. The highest degree of photon absorption is expected in transition that descend to ground or metastable states: more population in the lower level would allow for more absorption. The test used for this thesis requires two wavelengths that originate from the same upper level: one descending to a metastable level and one descending to a non-metastable level. This check was performed on both CTH and ALEXIS.

For homogeneous plasma conditions, the ratio of the observed intensities of two wavelengths in the absence of opacity effects is:

$$\frac{A_{i\to j} * N_i}{A_{k\to l} * N_k} \tag{3.11}$$

If both transitions descend from the same upper level this reduces to the ratio of their Einstein A coefficients. If the plasma is optically thick the intensity of the wavelength that descends to a metastable is reduced significantly more than the intensity of the wavelength that descends to a non-metastable state, a change that would be reflected in the intensity of the measured ratio.

Table 3.3 lists wavelengths along with the upper and lower levels for each wavelength on CTH. Similarly, Table 3.4 lists those values for ALEXIS. The lower level which are metastable have * beside them. An identical approach is taken to wavelengths which do not involve metastable states to allow for a control.

If a plasma were optically thick, as is the case for the wavelength 696.54 nm, a transition that descends to a metastable state would be absorbed more than 727.24 nm. As a result,

Wavelength Ratio	Upper level energy	Lower level energies	A ratio	Real intensity ratio
696.54/727.24	13.33 eV	11.548 ev*/11.623 eV	3.5 +/- 0.49	3.18 +/-0.31
852.11/794.81	13.28 eV	11.83 ev/11.72 eV	0.75 +/- 0.15	0.80 +/- 0.05

Table 3.4: Optical thickness assessment on ALEXIS. The intensity ratio from wavelengths $\frac{696.54}{727.24}$ is used to check optical thickness, whereas the ratio $\frac{852.11}{794.81}$ is used to check the validity of the process.

the experimental ratio in $\frac{696.54}{727.24}$ would be expected to be smaller than the ratio of Einstein A coefficients. Instead, in both the cases of ALEXIS and CTH, the experimental ratio slighter higher than but within uncertainty of the A value. The conclusion is that neither plasma is optically thick.

The line ratio results shown above are experimental evidence that the wavelengths within the plasmas being studied in this thesis are optically thick. A more in depth investigation of optical depth is outside the scope of this work, but will be included in future work. Such an investigation will include using the neutral densities diagnosed to calculate the optical depth of transitions from the ground and metastable states, and use an escape factor technique [39, 46] to include opacity effects if they are found to be significant.

3.8 Comparison between synthetic Ar II spectra and experimental spectra on CTH

While good agreement has been found between measured and synthetic spectra for Ar I, no such agreement has been found between the intensities of synthetic Ar II and experimental spectra on CTH. To address this, a number of fixes have been attempted, which we outline here. As will be shown below, the most likely answer for these discrepancies is that the LS resolution of the atomic dataset is not sufficient to model Ar II spectra, and that a new J-resolved dataset should be calculated. This information was passed on to atomic physics colleagues, and they are nearing completion of a new Ar II dataset to be used to

model spectra. To show how we reached this conclusion, we outline the possible reasons for discrepancies below.

1. Check to see if metastable populations are steady state

2. Check to see if Einstein A coefficients from NIST [31] match those from the model input file

3. The available set of rates are not J resolved, and the splitting routine assumes statistically split Ar II. If the J values are not in fact statistically split then no match will be achievable between synthetic and experimental spectra. The only available fix here is for a new input file to be made that has J-split levels.

3.8.1 Statistical splitting of Ar I and Ar II

A set of J-resolved rates are available for Ar I but not for Ar II. One possible reason for the absence of a match between observed line intensities and modeled values for Ar II is that J populations are not simply the statistical split of the LS populations. Electrons are populated into higher levels primarily from metastable states, all of which in Ar II have J values of either 3.5 or 4.5. Atomic transition rules dictate that $\Delta J = 0, +/-1$, and so J=2.5, 3.5, 4.5, and 5.5 will be preferentially populated from the metastable states. With sufficient collisions, the electrons would be expected to populate statistically into all J values available within the LS term, as a result of the proximity of the energy levels of separate J-split values. If this expectation is correct, all J values within an LS term would be expected to be statistically populated. With this information, the Ar II LS atomic dataset can be used to create a J resolved spectrum.

First, the assumption of statistical splitting can be checked. Recall the definition of a PEC:

$$PEC_{i\to j} = A_{i\to j} \times \frac{N_i}{N_{ground}}. \tag{3.12}$$

For the intensity ratio from two wavelengths this becomes:

$$\frac{PEC_{i\to j}}{PEC_{k\to l}} = \frac{A_{i\to j}N_i}{A_{k\to l}N_k}. \tag{3.13}$$

If the two transitions are from the same, statistically split upper LS-term but separate J values within that term:

$$\frac{PEC_{i\to j}}{PEC_{k\to l}} = \frac{A_{i\to j}g_iN}{A_{k\to l}g_kN} = \frac{A_{i\to j}g_i}{A_{k\to l}g_k}. \tag{3.14}$$

in which g_i is the statistical weight of level i. The validity of the assumption of statistical splitting of J-populations within an LS term can be checked. Every PEC corresponds to a wavelength, and the intensity from the corresponding intensity ratio can be compared to the ratio of statistical weights and Einstein A coefficients shown in Eq. 3.14. If both lines originate from the same J value, statistical splitting plays no role and the ratio must match: this can be used to ensure that no differences exist that arise from poor experimental intensity calibration. It can also be used to check that the emission is optically thin in both lines.

This process is performed for neutral Argon in table 3.5 and for singly ionized Argon in table 3.6.

Wavelength Ratio	numerator J	denominator J	$\frac{A_{i\to j}g_i}{A_{k\to l}g_k}$	Exp. ratio
696.54/727.24	1	1	3.5 +/- 0.59	3.93
714.68/738.34	1	2	0.04 +/- 0.01	0.07

Table 3.5: Ar I check of statistical splitting

In the case of the intensity ratio from wavelengths 696.54 nm/727.24 nm, both electrons descend from the same upper level. As a result, the ratio of experimental intensities should match the ratio of $\frac{A_{i\to j}g_i}{A_{k\to l}g_k} = \frac{A_{i\to j}}{A_{k\to l}}$. The experimental ratio is 3.93, and the ratio of $\frac{A_{i\to j}}{A_{k\to l}}$ is

3.5 +/- 0.59: there is overlap between the experimental ratio and the synthetic ratio. Conversely, in the case of the intensity ratio from wavelengths 714.68/738.34, the two transitions descent from different upper levels, but they do descend from the same upper LS term. The experimental ratio of 0.07 is higher than the $\frac{A_{i\rightarrow j}g_i}{A_{k\rightarrow l}g_k}$ ratio of 0.04 +/- 0.01. This shows that Ar I is not statistically split. Furthermore we see that the level with a J value of 1 has more population than statistical splitting would dictate, and the level with a J value of 2 has less population than statistical splitting would dictate. As a result, a J-resolved file was necessary to obtain agreement with for the observed ratio.

Wavelength Ratio	numerator J	denominator J	$\frac{A_{i\rightarrow j}g_i}{A_{k\rightarrow l}g_k}$	Exp. ratio
401.388/434.802	3.5	3.5	0.09 +/- 0.01	0.09
480.628/473.55	2.5	1.5	2.02 +/- 0.12	2.93
480.628/484.808	2.5	0.5	2.76 +/- 0.36	4.13
401.388/437.951	3.5	0.5	0.42 +/- 0.03	1.00

Table 3.6: Ar II check of statistical splitting

Table 3.6 shows the experimental and $\frac{A_{i\rightarrow j}g_i}{A_{k\rightarrow l}g_k}$ ratios for Argon II. Within each pair, both wavelength originate from the same upper LS term. "Numerator" and "denominator" refer to the J value of the upper level in the transition. When the two match, that indicates that they come from the same level. When two do not match, that indicates that the two come from a different level within the same term.

The first intensity ratio to examine is that from wavelengths 401.388/434.802, which originate from the same upper level. In the case of that intensity ratio there is a match between the experimental ratio of 0.09 and the $\frac{A_{i\rightarrow j}g_i}{A_{k\rightarrow l}g_k}$ ratio of 0.09 +/- 0.01. This is expected. By contrast, the remaining intensity ratios do not come from the same upper level, only the same LS term. None of those intensity ratios show a match between $\frac{A_{i\rightarrow j}g_i}{A_{k\rightarrow l}g_k}$ ratios and experimental ratios. Furthermore, this discrepancy in Ar II is weighted towards J levels which can be populated from metastable states. This suggests a lack of statistical splitting

in both Ar I and Ar II. By contrast, a good match is observed between Ar I experimental and synthetic spectra, despite a lack of statistical splitting. This is because the Ar I dataset is J-resolved and allows for collisions that redistribute in J. This set of comparisons motivated a request for a new Ar II atomic dataset which is now underway and nearing completion.

3.8.2 Comparison between Einstein A coefficients from NIST and model input file in Ar II

A comparison between the calculated A-values from the existing Ar II data file and those from the NIST [31] database showed differences. The levels within the file for Ar II were not split by J, only LS, and so the Einstein A coefficients from the input file were not expected to match those in NIST [31]. However, Einstein A coefficients in the input file are expected to be the weighted sum of the individual Einstein A coefficients, and that was found to not be the case. The most practical solution was to calculate all PECs after statistically splitting all atomic populations and use the NIST J-resolved Einstein A coefficient to generate the PECs. The following equation shows the calculation for PEC from the normalized upper level population ($\frac{N_i}{N_{ground}}$), which is available from the CRM.

$$PEC_{i\to j}^{\sigma_k} = A_{i\to j} \times \frac{N_i^{\sigma_k}}{N_0} \tag{3.15}$$

N_i can be estimated from an unsplit N through the following equation:

$$N_i = g_i N \tag{3.16}$$

where

$$g_i = \frac{2J+1}{(2L+1)(2S+1)} \tag{3.17}$$

The denominator is the total number of weights within the unsplit level. The numerator is the weight of the individual split level of interest. This is a necessary fix for the input file,

but the previous section shows that the levels are not statistically split across J values, so this fix was not sufficient to fix the discrepancy.

3.8.3 Comparison between ionization balance and experimental data

A check was performed on the neutral density diagnostic through the use of a time dependent ionization balance. This produces the population of Ar I (ionization level 0) and Ar II (ionization level 1), normalized to the total population of Argon I from start. It also produces the population of other ionization states, but observational evidence suggests that CTH lacks higher ionization states. The populations of Ar I and Ar II, normalized to the total neutral population from start, is also available experimentally: Argon I corresponds to $\frac{n_n}{n_n+n_e}$ and Argon II corresponds to $\frac{n_e}{n_n+n_e}$.

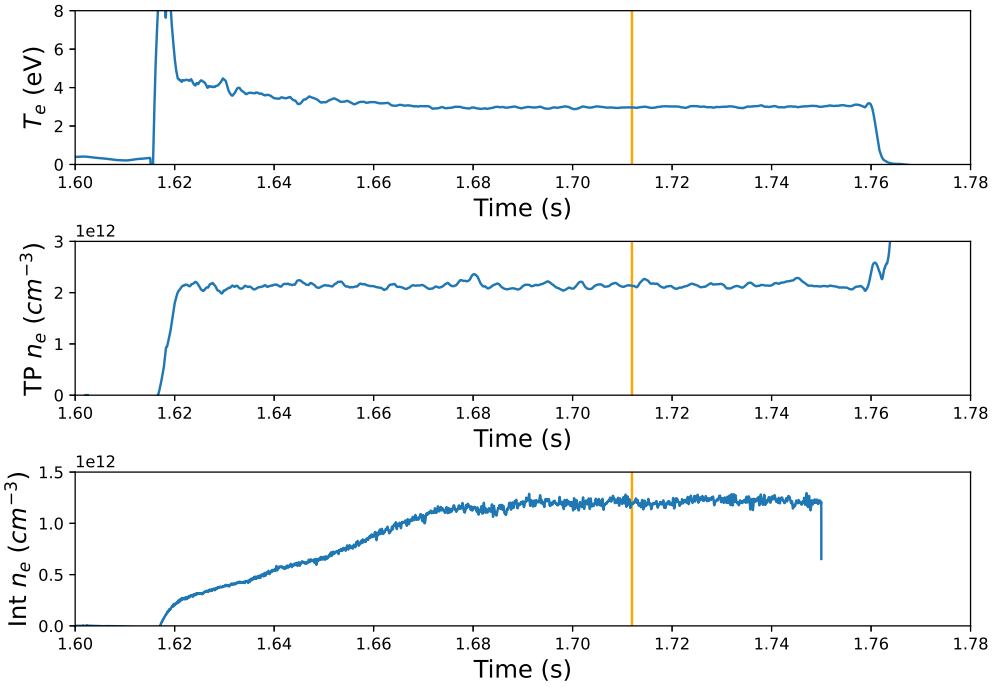

Figure 3.4: Plasma discharge used as an example for the ionization balance. Electron temperature is plotted on the top. Electron density from the triple probe is in the middle. Electron density from the interferometer is on the bottom. A vertical orange line corresponds to the start time of a sample spectrum pulled from this discharge. This plasma is considered to have started at 1.617 s.

Fig. 3.4 shows the electron temperature and electron density from a single plasma discharge. The top frame shows the electron temperature, the middle frame shows the electron density from the triple probe, and the bottom from shows the electron density from the interferometer. The electron density from the interferometer increases more slowly than that of the triple probe; one possible explanation for this is the electron density increases quickly in the local region measured by the triple probe but more slowly along the line-integrated region measured by the interferometer. A spectrum is selected from the discharge, and the start time for that spectrum is demonstrated by a vertical orange line. The triple probe provides an electron temperature of 3 eV and an electron density of $2.2 \times 10^{12}\,\mathrm{cm}^{-3}$.

The interferometer provides an electron density of $1.3 \times 10^{12}\,\mathrm{cm}^{-3}$. This plasma is considered to have started at 1.617 s, when the diagnostic signals in Fig. 3.4 begin to rise.

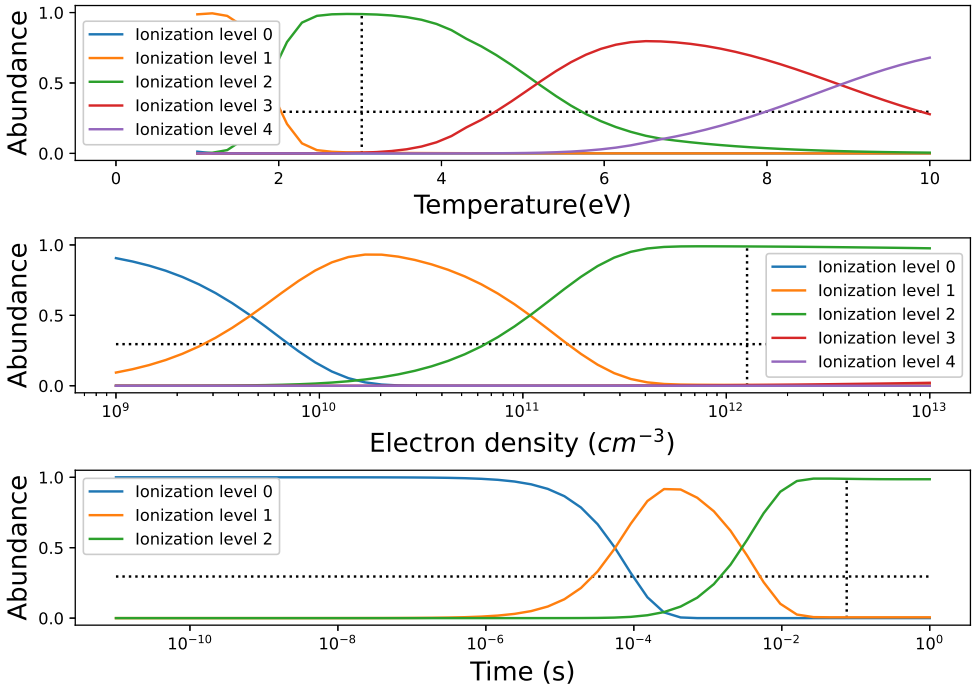

Figure 3.5: Ionization balance. The top graph is temperature dependent, the middle graph is electron density dependent, and the bottom graph is time dependent. The time, temperature, and electron density are 75 ms, 3 eV, and $1.2 \times 10^{12}\,\mathrm{cm}^{-3}$ in any case where they are not time dependent.

Fig. 3.5 shows the resulting argon fractional abundances for several ionization states of Ar from the plasma shown in Fig. 3.4 at the time indicated by the vertical orange line. In each graph, a horizontal dotted line corresponds to the experimental abundance of ionization level 0, or $\frac{n_n}{n_n+n_e}$. A vertical dotted line corresponds to the correct value for the plasma of interest. The top graph shows the abundance vs. temperature, assuming an electron density of $1.2 \times 10^{12}\,\mathrm{cm}^{-3}$ and a time of 75 ms. 75 ms was chosen because it was the time between the start of the plasma and the start of the frame in the frame chosen for the example shown in Fig. 3.5. A vertical line is positioned at 3 eV. The middle graph shows the abundance vs electron density, assuming a temperature of 3 eV and a time of 75 ms. A vertical line is

positioned at $1.2 \times 10^{12}\,\mathrm{cm}^{-3}$. The bottom graph shows the abundance vs time, assuming an electron density of $1.2 \times 10^{12}\,\mathrm{cm}^{-3}$ and a temperature of 3 eV. A vertical line is positioned at 75 ms.

If the input rate coefficients to the time dependence ionization balance of the CRM were correct, the vertical and horizontal lines would intersect at the blue line, ionization level 0. In reality, the model significantly over-predicts the speed of ionization. This suggests that the input rate coefficients are inaccurate. In particular, the existing hypothesis is that the available predicted Ar I recombination rates are too low, resulting in a lower availability of charge states above Ar I than is predicted by the ionization balance model.

3.9 The search for spectroscopic electron density or electron temperature diagnostics on CTH

Plasma parameters n_e and T_e can be measured by the triple probe and the interferometer, but a search was performed for neutral Argon line ratios that could measure either. In particular, a line ratio to estimate T_e would provide a second, line integrated measurement.

A useful spectroscopic T_e diagnostic consists of a line ratio which is sensitive to T_e but insensitive to n_e. The reverse applies for n_e. Spectral lines exhibit different behavior in different plasma parameter spaces. In contrast to the n_n diagnostic which functions in any plasma parameter space for which atomic rates have been calculated, T_e and n_e diagnostics are plasma specific.

Figs. 3.6 and 3.7 show the line ratios available for CTH plasma parameter regimes. In both the variable of diagnostic interest is plotted on the x-axis. The synthetic line ratio at that variable is plotted on the y-axis. The vertical spread represents the range of the other variable. Each point corresponds to a different temperature and density. A useful diagnostic has significant change over the variable of interest but little vertical spread.

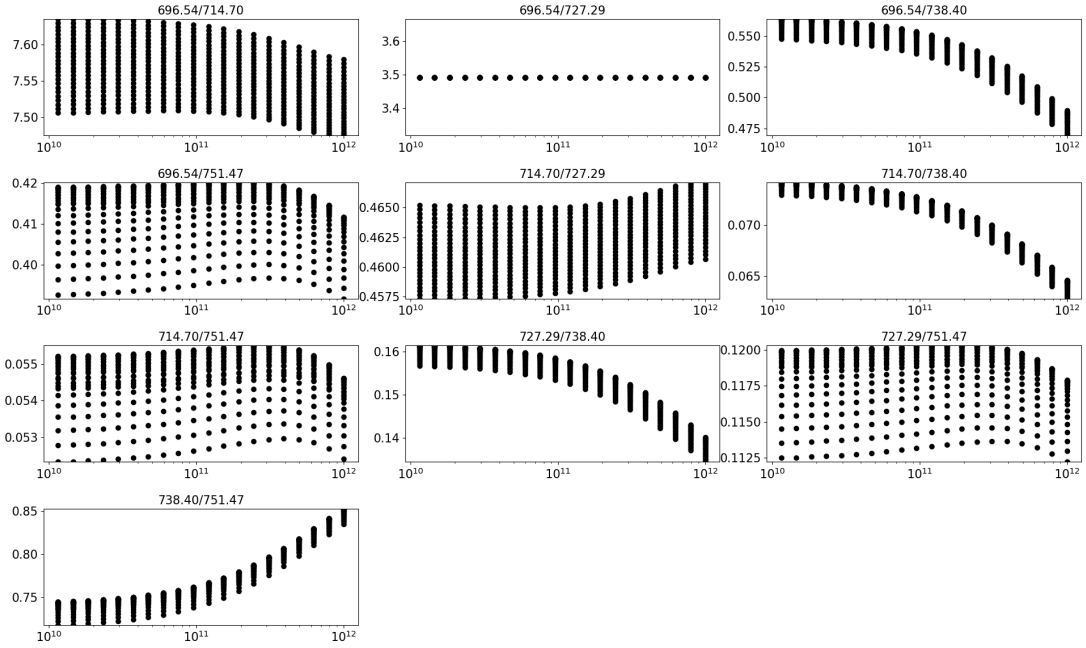

Figure 3.6: Synthetic line ratios on CTH that could lead to a n_e diagnostic. The x-axis on all graphs is n_e in cm^{-3} and the y-axis in all graphs is the synthetic line ratio at that electron density. The range of T_e represented here is 4 eV to 6.5 eV.

Fig. 3.6 show the synthetic line ratios available in pursuit of a n_e diagnostic on CTH. None are sufficient. As an example, 714.7 nm/727.29 nm is insensitive to changes in n_e and has a significant spread in T_e.. 738.4 nm/751.47 nm is a line ratio that at first glance seems as though it might be a sensitive enough between 10^{11} and 10^{12} cm^{-3}, but upon closer inspection the total change in the ratio, from 0.75 to 0.85, is insufficient for an effective diagnostic. Note that 696.54 nm/727.29 nm is flat. This is because both wavelengths originate from the same upper level, so the ratio is simply the ratio of Einstein A coefficients.

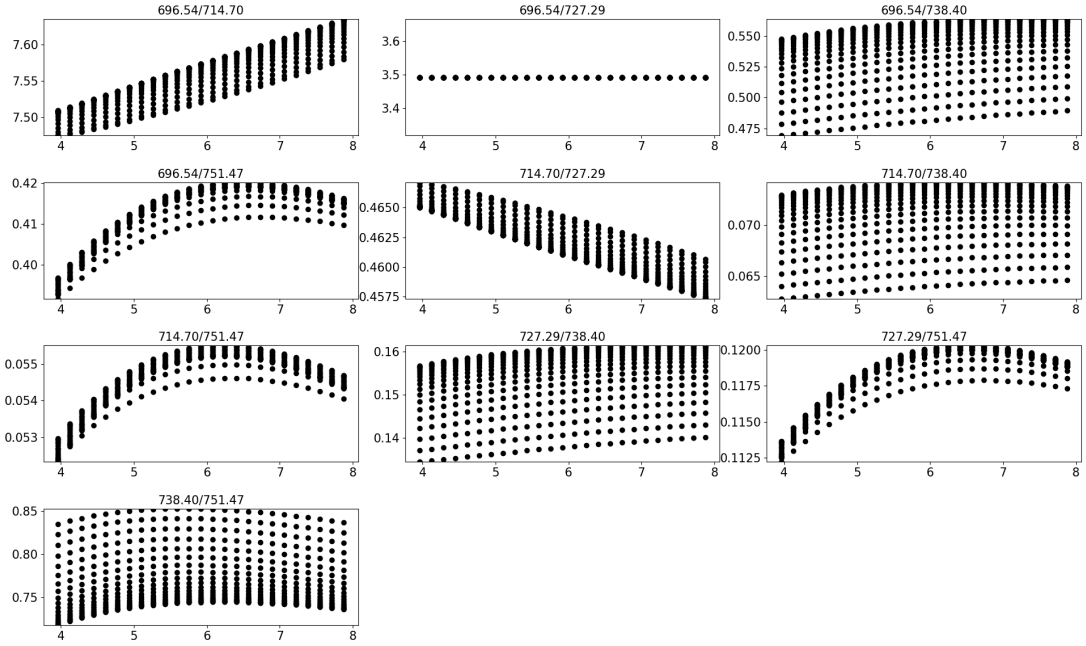

Figure 3.7: Synthetic line ratios on CTH that could lead to a T_e diagnostic. The x-axis on all graphs is T_e in eV and the y-axis in all graphs is the synthetic line ratio at that temperature. The range of n_e represented here is 1×10^{10} to 1×10^{12} cm^{-3}.

Fig. 3.7 shows the synthetic line ratios available in pursuit of a T_e diagnostic on CTH. As in the case of a n_e diagnostic, no line ratios are available. The ratio of 714.7 nm/727.29 nm, which appeared in the n_e diagnostic case as though it contained significant sensitivity in T_e, does not change over the range of temperatures observed to be considered as a diagnostic.

No line ratios are examined for ALEXIS plasmas. ALEXIS plasmas require a time-dependent approach to modeling. The method used to find the correct time for the model involves comparing synthetic vs experimental spectra for a range of times. Consequently, it is not then possible to refer back to those line ratios for electron temperature and density as they have already been used to find the optimal time.

Chapter 4

Data Analysis and Results for ALEXIS and CTH

The aim of this chapter is to use the spectrometer described in Section 2.2.2.2 along with the CRM described in Section 3.3 to benchmark and then use the spectroscopic neutral density diagnostic that is the focus of this thesis to characterize the plasmas on the CTH and ALEXIS devices. This chapter will start by summarizing basic plasma physics concepts, which will then be laid out for both devices. The wavelengths used on both devices will be described and justified. The plasma profiles of both devices will be explored, an important step due to the line integrated nature of the neutral density diagnostic.

The ALEXIS plasma results will be summarized. The use of the time dependent CRM on ALEXIS will be justified. Efforts to benchmark the neutral density on the ALEXIS device will be explored. Finally, a comparison will be presented between the appropriate time found from the time-dependent CRM and the diffusion-to-wall time.

The CTH plasma results will be summarized. The particle balance model of the plasma will be explored and the results compared to experiment. Similarly, the power balance model will be explored. The use of the neutral density diagnostic on CTH will be justified. Finally, the neutral density diagnostic will be used to estimate the resistivity of CTH plasmas.

An important note about the use of a spectroscopic frame within this chapter: each plasma discharge within CTH is measured time-dependently using multiple spectroscopic frames. A full CTH discharge is referred to as a discharge. Each plasma which is measured by a single spectrum within that discharge is referred to as a separate plasma.

Before characterization of the plasma begins, background plasma physics is introduced.

4.1 Basic plasma physics

A charged particle or charged object within a plasma is subject to shielding of a length characterized by the Debye length (λ_D):

$$\lambda_D = \left(\frac{\epsilon_0 K T_e}{n_e e^2}\right) = 743 \times \sqrt{\frac{T_e}{n_e}}. \tag{4.1}$$

In the context of this thesis, the Debye length primarily plays a role in determining the collection area of probe tips.

The electron thermal velocity v_{th}^e is:

$$v_{th}^e = \sqrt{\frac{k_B T_e}{m_e}} = 4.19 \times 10^7 T_e^{1/2}\, cm/s. \tag{4.2}$$

The ion thermal velocity v_{th}^i depends on the ion mass μ, expressed in units of the mass of a proton m_p: $\mu = \frac{m_i}{m_p}$, which for Argon ions is 40:

$$v_{th}^i = \sqrt{\frac{k_B T_i}{m_i}} = 9.79 \times 10^5 T_i^{1/2} \mu^{-1/2}\, cm/s. \tag{4.3}$$

Charged particles experience circular motion in the presence of a magnetic field, and the Larmor gyroradius is the radius of the circular motion of a charged particle around a magnetic field line. The electron gyroradius is:

$$r_L^e = \frac{m_e v_{th}^e}{qB} = \frac{2.38 \times T_e^{1/2}}{B}\, cm. \tag{4.4}$$

The gyroradius depends on the charge of the charged particle. As a result, the ion gyroradius depends on the charge state, 1 for Ar II.

$$r_L^i = \frac{m_i v_{th}^i}{qB} = \frac{102 \times (\mu T_i)^{1/2}}{B \times Z}\, cm. \tag{4.5}$$

The related frequency of this orbit is the gyrofrequency:

$$\begin{aligned} \omega_c &= \frac{eB}{m} \\ \omega_c^e &= \frac{eB}{m_e} = 1.76 \times 10^7 B \text{ rad/s} \\ \omega_c^i &= \frac{eB}{m_i} = 9.58 \times 10^3 \frac{ZB}{\mu} \text{ rad/s}. \end{aligned} \tag{4.6}$$

The mean free path λ_{mfp} is the distance traveled before a collision with another particle, in this case a neutral Argon atom. This depends on the neutral argon density n_n as well as the collision cross section between the two particles σ_{AB}.

$$\lambda_{mfp} = \frac{1}{n_n \sigma_{AB}}. \tag{4.7}$$

The collision frequency ν is related to the velocity and mean free path as well as the collision cross section and thermal velocity:

$$\nu = \frac{v_{th}}{\lambda_{mfp}} = n\sigma v_{th}. \tag{4.8}$$

4.2 Plasma motion from fluid equations

We consider the treatment of the plasma as two separate fluids: ions and electrons. We begin with the fluid equation of motion:

$$mn\frac{d\vec{v_\perp}}{dt} = \pm en(\vec{E} + \vec{v_\perp} \times \vec{B}) - kT\nabla n - mn\nu\vec{v}. \tag{4.9}$$

This equation begins $\pm$ as the sign depends on whether the motion of ions $(+)$ or electrons $(-)$ is being considered. We assume $\frac{d\vec{v_\perp}}{dt}$ is small, so:

$$\begin{aligned} 0 &= \pm en(\vec{E} + \vec{v_\perp} \times \vec{B}) - kT\nabla n - mn\nu\vec{v} \\ mn\nu\vec{v} &= \pm en(\vec{E} + \vec{v_\perp} \times \vec{B}) - kT\nabla n \\ \vec{v} &= \pm\frac{e}{m\nu}(\vec{E} + \vec{v_\perp} \times \vec{B}) - \frac{kT}{m\nu}\frac{\nabla n}{n} \end{aligned} \tag{4.10}$$

The definition of mobility (μ) and diffusion (D) appears naturally:

$$\begin{aligned} D &= \frac{kT}{m\nu} \\ \mu &= \frac{e}{m_e\nu} \end{aligned} \tag{4.11}$$

Similarly, conductivity is related to mobility:

$$\sigma = n_e e\mu = \frac{n_e q^2}{m\nu} \tag{4.12}$$

Diffusion concerns movement caused by the thermal motion of the particles, whereas mobility concerns movement of charged particles with respect to E and B fields. Both are impeded by collisions.

A random walk estimate is used to estimate the diffusion coefficient:

$$D = (step\,size)^2(collision\,frequency).$$

The parallel step size is the mean free path (λ_{mfp}) whereas the perpendicular step size is the Larmor radius (r_L).

$$\begin{aligned} D &= (\delta x)^2\nu \\ \delta x_\perp &= r_L \\ \delta x_\parallel &= \lambda_{mfp} \end{aligned} \tag{4.13}$$

First take diffusion parallel to the magnetic field: $D_\parallel = (\lambda_{mfp})^2\nu$. Upon first glance this estimate shows proportionality between $D_\parallel$ and ν, which is counter-intuitive. Diffusion describes movement, whereas the collision frequency impedes movement, so a higher collision frequency would intuitively lead to a decrease in movement. However, upon closer inspection:

$$
\begin{aligned}
D_{\parallel} &= (\lambda_{mfp})^2 \nu \\
&= \frac{n_n \sigma v_{th}}{(n_n \sigma)^2} \\
&= \frac{v_{th}}{n_n \sigma}
\end{aligned}
$$

This proportionality is much more intuitive. A higher thermal velocity corresponds to more movement. Conversely, both more neutral Argon and a higher collision cross section result in more collisions and thus less movement.

Now we turn to diffusion perpendicular to the magnetic field: $D_{\perp} = (r_L)^2 \nu$. Motion perpendicular to field lines is possible due to the gyro-orbit of a charged particle around a field line combined with the subsequent collision of that charged particle, typically with a neutral atom. However, the assumption of proportionality between $D_{\perp}$ and ν breaks down when the collision frequency is significantly higher than the gyrofrequency. Fortunately, the gyrofrequency on CTH is significantly higher than the collision frequency for both electrons and ions: the ratio of gyrofrequency to collision frequency ($\frac{\omega_c}{\nu}$) for electrons is 1×10^7 and the ratio for ions is 1×10^3. As a result, both electrons and ions on CTH are shown to be well magnetized.

A subset of the plasmas obtained on CTH have an Ohmic plasma so Ohm's law plays a role. A conductivity tensor can be derived from Ohm's law [47]. Consider a magnetic field $\vec{B} = B_0 \hat{z}$ and Ohm's law:

$$
\vec{J} = \sigma_0 (\vec{E} + \vec{v_e} \times \vec{B}) \tag{4.14}
$$

The plasma current can be related to the electron velocity:

$$
\vec{J} = -n_e e \vec{v_e}. \tag{4.15}
$$

The velocity from Eq. 4.15 can be substituted into Eq. 4.14:

$$\vec{J} = \sigma_0(\vec{E} - \frac{\vec{J}}{n_e e \vec{v_e}} \times \vec{B}).$$

Distribute σ into the parentheses to isolate $\hat{J} \times \hat{B}$:

$$\vec{J} = \sigma_0 \vec{E} - \frac{\sigma_0 \vec{B}_0}{n_e e \vec{v_e}} (\vec{J} \times \hat{z}).$$

Simplify to include the gyrofrequency (ω_c) and collision frequency (ν):

$$\vec{J} = \sigma_0 \vec{E} - \frac{\omega_c}{\nu} (\vec{J} \times \hat{z}) \tag{4.16}$$

Recall that:

$$\vec{J} \times \hat{z} = J_x \hat{y} - J_y \hat{x}$$

As a result, the $\hat{x}$, $\hat{y}$, and $\hat{z}$ components of the plasma current J can be expressed as:

$$\begin{aligned} J_x &= \sigma_0 E_x + \frac{\omega_c}{\nu} J_y \\ J_y &= \sigma_0 E_y - \frac{\omega_c}{\nu} J_x \\ J_z &= \sigma_0 E_z \end{aligned}$$

The next step is to express the plasma current solely in terms of the electric field. The $\hat{x}$ component is used as an example:

$$\begin{aligned} J_x &= \sigma_0 E_x - \frac{\omega_c}{\nu}(\sigma_0 E_y + \frac{\omega_c}{\nu} J_x) \\ &= \sigma_0 E_x - \frac{\omega_c}{\nu}\sigma_0 E_y - \frac{\omega_c^2}{\nu^2} J_x \\ J_x + \frac{\omega_c^2}{\nu^2} J_x &= \sigma_0 E_x - \frac{\omega_c}{\nu}\sigma_0 E_y \\ J_x &= \frac{\nu^2}{(\nu^2 + \omega_c^2)}\sigma_0 E_x + \frac{\omega_c \nu}{(\nu^2 + \omega_c^2)}\sigma_0 E_y \end{aligned}$$

A similar procedure can be followed with the y component. The z component is more straightforward as it contains no perpendicular term. Combining all components results in:

$$
\begin{aligned}
J_x &= \frac{\nu^2}{(\nu^2+\omega_c^2)}\sigma_0 E_x - \frac{\omega_c \nu}{(\nu^2+\omega_c^2)}\sigma_0 E_y \\
J_y &= \frac{\nu^2}{(\nu^2+\omega_c^2)}\sigma_0 E_y + \frac{\omega_c \nu}{(\nu^2+\omega_c^2)}\sigma_0 E_x \\
J_z &= \sigma_0 E_z.
\end{aligned}
$$

This conductivity can be fully represented through a tensor:

$$
\begin{aligned}
\sigma &= \begin{pmatrix} \sigma_\perp & -\sigma_H & 0 \\ \sigma_H & \sigma_\perp & 0 \\ 0 & 0 & \sigma_\parallel \end{pmatrix} \\
\sigma_\perp &= \left(\frac{\nu^2}{\nu^2+\omega_c^2}\right)\sigma_0 \\
\sigma_H &= \left(\frac{\nu\omega_c}{\nu^2+\omega_c^2}\right)\sigma_0 \\
\sigma_\parallel &= \sigma_0 = \frac{n_e q^2}{m\nu}
\end{aligned}
\tag{4.17}
$$

Parallel conductivity, σ_0, is current along the $\vec{B}$ field. Hall conductivity, σ_H, is current perpendicular to both $\vec{E}$ and $\vec{B}$ fields. Pederson or perpendicular conductivity, $\sigma_\perp$ is current parallel to $\vec{E}$ fields but perpendicular to the $\vec{B}$ field. As seen previously, the collision frequency is ν. The gyrofrequency is ω_c. As described in the discussion of diffusion, the gyrofrequency is much bigger than the electron-neutral collision frequency for CTH plasmas: $\omega_c >> \nu$. As a result, both $\sigma_\perp$ and σ_H are approximately zero: the plasma current is dominated by $\sigma_\parallel$.

The next step is to derive the $\vec{E} \times \vec{B}$ drift. By assuming that $\nabla n = 0$ and $\frac{d\vec{v}_\perp}{dt} = 0$ in a plasma with low collisionality, a simplified version of the fluid equation can be used [47]:

$$\begin{aligned} mn\frac{d\vec{v_\perp}}{dt} &= \pm en(\vec{E} + \vec{v} \times \vec{B}) - kT\nabla n - mn\nu\vec{v} \\ 0 &= \pm en(\vec{E} + \vec{v_\perp} \times \vec{B}) \end{aligned} \tag{4.18}$$

Note that:

$$(\vec{v} \times \vec{B}) \times \vec{B} = -\vec{v}_\perp B^2$$

The result is the $\vec{E} \times \vec{B}$ drift velocity:

$$\vec{v}_\perp = \frac{\vec{E} \times \vec{B}}{B^2} \tag{4.19}$$

A derivation for the $\nabla P \times \vec{B}$ drift is not included here due to the uniformity of n throughout CTH. In combining all these concepts, we refer back to the velocity based on the fluid equations:

$$\vec{v} = \pm\frac{e}{m\nu}(\vec{E} + \vec{v_\perp} \times \vec{B}) - \frac{kT}{m\nu}\frac{\nabla n}{n}$$

We then summarize the x, y, and z components of this velocity:

$$\begin{aligned} v_x &= \frac{\nu}{(\nu^2 + \omega_c^2)}\Big(\nu\sigma_0 E_x - \omega_c\sigma_0 E_y\Big) - D_\perp\frac{\nabla n}{n} + \frac{v_{E_x}}{1 + (\frac{\nu_n}{\omega_c})^2} \\ v_y &= \frac{\nu}{(\nu^2 + \omega_c^2)}\Big(\nu\sigma_0 E_y + \omega_c\sigma_0 E_x\Big) - D_\perp\frac{\nabla n}{n} + \frac{v_{E_y}}{1 + (\frac{\nu_n}{\omega_c})^2} \\ v_z &= \sigma_0 E_z - D_\parallel\frac{\nabla n}{n} \end{aligned} \tag{4.20}$$

The last term relates to velocity from $\vec{E} \times \vec{B}$ drift. Many of these terms can be disregarded. We consider $\frac{\nabla n}{n} \approx 0$ along the Z direction. leaving only the E_z component.

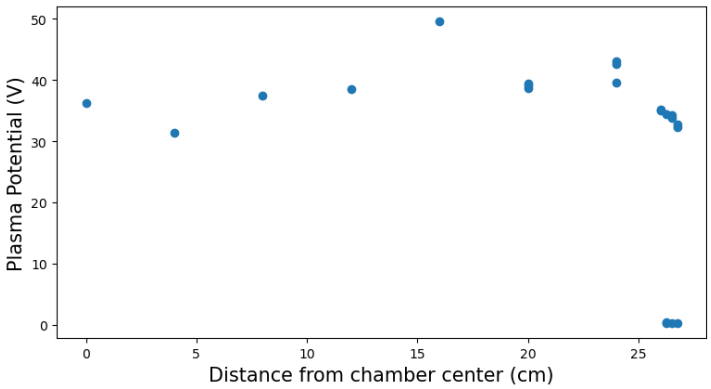

Figure 4.1: Radial profile of the plasma potential in a plasma with a high fractional ionization of 92%.

Fig. 4.1 shows the radial profile of the plasma potential in a plasma with a high fractional ionization, specifically 92%. This shows very little change in potential, suggesting little or no radial $\vec{E}$ field. This eliminates both the E_x and E_y components of the radial velocities as well as velocity from $\vec{E} \times \vec{B}$ drift. Any E_z is from the applied loop voltage and is expected to result in OH current. What remains is the following:

$$\begin{aligned} v_x &= D_\perp \frac{\nabla n}{n} \\ v_y &= D_\perp \frac{\nabla n}{n} \\ v_z &= \sigma_0 E_z \end{aligned} \tag{4.21}$$

The only diffusion which remains is $D_\perp$, despite the value for $D_\parallel$ being significantly higher (calculations shown in Table 4.1). In the absence of OH current, only random-walk movement is expected from particles parallel to the magnetic field.

4.3 Characteristic plasma values for each device

In this section we show characteristic values for the plasma experiments used in this dissertation. These values are representative but not comprehensive: every plasma parameter shown varies.

The values in Table 4.1 are representative of CTH plasma parameters. Only the ions and electrons react to the magnetic field. The collision cross section with neutrals is an estimate. The electron-neutral cross section comes from Raju et al. [48], Eq. 9, based on work by Garcia et al. [49]:

4.3.1 Values for CTH

Value	Ions	Electrons	Neutrals
Magnetic field B (T)	0.6	0.6	0.6
Temperature T (eV)	1	10	0.025
Density (cm^{-3})	1×10^{11}	1×10^{11}	1×10^{12}
Collision cross section with neutrals σ_n (cm^2)	1×10^{-13}	1×10^{-15}	1×10^{-14}
Mean free path λ_{mfp} (cm) (Eq. 4.7)	100	1×10^{4}	100
Thermal velocity v_{th} (cm/s) (equations 4.2 , 4.3)	1.5×10^{5}	1.3×10^{8}	3.0×10^{4}
Larmor radius r_L (cm) (equations 4.5, 4.4)	0.108	0.0013	-
Gyrofrequency ω_c (rad/s)	1.4×10^{6}	1.1×10^{11}	-
Collision frequency ν (s^{-1}) (Eq. 4.8)	1.5×10^{3}	1.3×10^{4}	268
Diffusion coefficient $D_\perp$ (cm^2/s) (Eq. 4.13)	17.9	0.0208	2.7×10^{6}
Diffusion coefficient $D_\parallel$ (cm^2/s) (Eq. 4.13)	1.5×10^{7}	1.3×10^{12}	2.7×10^{6}
Longitudinal conductivity σ_0 $(\frac{C^2 s}{kg\,cm})$	2.5	0.21	-
Hall conductivity σ_H $(\frac{C^2 s}{kg\,cm})$	2.0×10^{-3}	2.7×10^{-8}	-
Pederson conductivity $\sigma_\perp$ $(\frac{C^2 s}{kg\,cm})$	1.5×10^{-6}	3.3×10^{-15}	-
Debye length λ_D (cm)	0.002	0.0074	-

Table 4.1: CTH characteristic plasma parameters.

$$Q_{inel} = 4\pi a_0^2 \left[M_{inel}^2 \left(\frac{R}{T_e}\right) ln\left(4C_{inel}\frac{T_e}{R}\right) \right] \tag{4.22}$$

In the above equation, Q_{inel} represents the inelastic collisional cross section in m^2, a_0 represents the Bohr radius, here $5.3 \times 10^{-11}\,m$, M_{inel} is 2.255, C_{inel} is 0.8114, and R is the Rydberg constant, 13.6 eV. M_{inel} and C_{inel} are both dimensionless. Both M_{inel} and M_{inel} are defined by Inokuti et al. [50] as the dipole-oscillator strength per atomic excitation energy. This equation comes from Raju et al. [48] based on work by Inokuti et al. [50].

Both the ion-neutral cross section and the neutral-neutral cross section come from Phelps et al. [51].

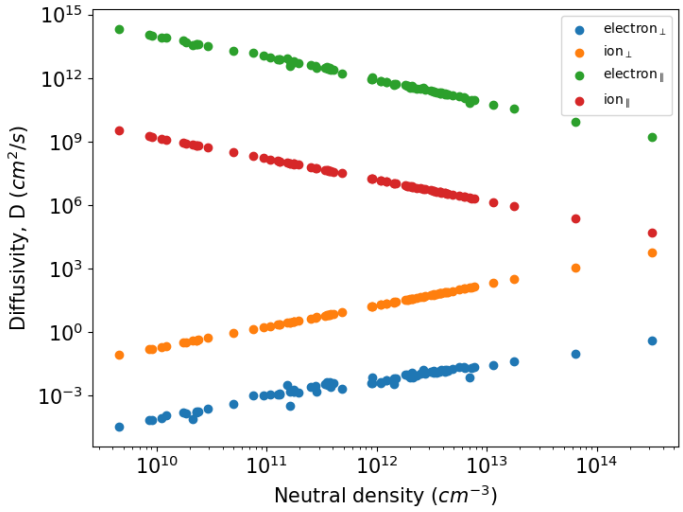

Figure 4.2: Perpendicular and parallel diffusion vs. neutral density for electrons and ions for all plasmas. Ion temperature is assumed to be 1 eV throughout.

Fig. 4.2 shows perpendicular and parallel diffusion coefficients for electrons and ions for every plasma available. Densities and temperatures are based on actual data with the exception of ion temperature which is assumed to be 1 eV for all plasmas. The plasma is assumed to be quasi-neutral, with ion density equal to electron density. Parallel diffusion is universally higher than perpendicular diffusion. Parallel diffusion decreases with neutral density because a larger neutral density corresponds to a higher collision frequency and a lower mean free path. By contrast, that higher collision frequency results in an increase in perpendicular diffusion as those collisions are the mechanism for transport across the magnetic field. Electron diffusion parallel to the magnetic field is higher than ion diffusion

as a result of the difference in thermal velocities. Ion perpendicular diffusion is higher than electron perpendicular diffusion due to both a larger Larmor radius and collision cross section.

In determining velocity from diffusion in the perpendicular and parallel direction, note that $v = -D\frac{\nabla n}{n}$. Parallel to the magnetic field an assumption is made that $\vec{\nabla}_{\parallel} n = 0$, therefore $v_{\parallel B} = 0$. Perpendicular to the magnetic field $\frac{\nabla n}{n} \approx \frac{1}{L}$, where L is the length over which the density is changing as measured by the triple probe.

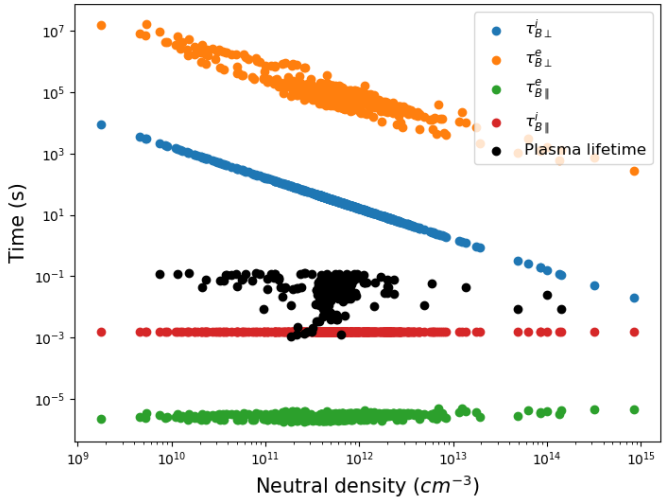

Figure 4.3: Each point in this figure represents a characteristic time for a CTH plasma. The black points correspond to the time between the beginning of a CTH plasma discharge and the beginning of the frame represented by that point. The blue points represent $\tau^i_{D\perp}$, and the orange points $\tau^e_{D\perp}$. Red points represent $\tau^i_{\parallel}$ and green points $\tau^e_{\parallel}$. While electrons have a higher thermal velocity, they also have a higher frequency for collisions with neutrals.

Fig. 4.3 shows the estimated time for ions and electrons to diffuse 29 cm to the wall perpendicular to the magnetic field (blue and orange respectively). This is calculated as:

$$\tau_{\perp} = \frac{\Delta x_{\perp}^2}{D_{\perp}} = \frac{\Delta x_{\perp}^2}{r_L^2 \nu} = \frac{\Delta x_{\perp}^2}{r_L^2 v_{th} n_n \sigma} \tag{4.23}$$

in which $\Delta x_{\perp}$ is 29 cm, the width of CTH as a cylinder.

The estimated time for ions and electrons to random-walk halfway around the machine is also plotted (red and green respectively). This is calculated as:

$$\tau_{\parallel} = \frac{\Delta x_{\parallel}}{v_{th}} \tag{4.24}$$

The $\Delta x_{\parallel}$ is 471 cm, the length of CTH as a cylinder through $2\pi R_0$ where $R_0 = 75$. Parallel diffusion is assumed to be negligible due to limited density gradient parallel to the magnetic field. Electrons are well confined around CTH for all the plasmas. Neither ions nor electrons can diffuse to the wall in the time during which the plasma exists on CTH.

4.3.2 Values for ALEXIS

The ALEXIS device has a magnetic field that is lower than that of CTH. The temperature regime is the same. The electron density is 3 orders of magnitude lower, but with similar neutral densities.

Value	Ions	Electrons	Neutrals
Magnetic field (T)	0.05	0.05	0.05
Temperature (eV)	1	10	0.03
Density (cm^{-3})	1×10^{9}	1×10^{9}	1×10^{14}
Neutral collision cross section (cm^2)	1×10^{-14} [48]	1×10^{-16} [51]	1×10^{-14} [51]
Mean free path (cm) (Eq. 4.7)	100	1×10^{4}	100
Thermal velocity (cm/s) (equations 4.2 , 4.3)	1.5×10^{5}	1.3×10^{8}	3.0×10^{4}
Larmor radius (cm) (equations 4.5, 4.4)	0.108	0.0013	-
Gyrofrequency (rad/s)	12	8.8×10^{5}	-
Collision frequency (s^{-1}) (Eq. 4.8)	1.5×10^{3}	1.3×10^{4}	268
Diffusion coefficient $\perp$ (cm^2/s) (Eq. 4.13)	17.9	0.0208	2.7×10^{6}
Diffusion coefficient $\parallel$ (cm^2/s) (Eq. 4.13)	1.5×10^{7}	1.3×10^{12}	2.7×10^{6}
Debye length λ_D (cm)	-	0.074	-

Table 4.2: ALEXIS characteristic plasma parameters.

4.4 Spectral line choice

Table 4.3 shows the wavelengths used in the spectral analysis of CTH. The diffraction grating used allowed for a wavelength window of 80 nm. 685 nm-765 nm was chosen as it allowed for wavelength calibration with an Argon lamp and gave the highest quality neutral lines to choose from. In order to be included, lines must have an Einstein A coefficient grade above B (10%), and they must not be blended with neighboring lines. Individual lines were excluded from an individual frame if they were found to be too weak to obtain a fit or saturated for that particular frame. 750.3 nm was found to show a poor match between synthetic and experimental on both CTH and ALEXIS, and so was excluded from all analysis. The reason for this poor match was never found, though many possibilities were explored. More investigation is needed.

λ (nm)	Upper Energy (eV)	Lower Energy (eV)	A Coeff. (s^{-1})	Grade	Grade in %
696.54	13.33	11.55	6.40×10^6	B+	7
714.70	13.28	11.55	6.30×10^5	B+	7
727.24	13.33	11.62	1.83×10^6	B+	7
738.34	13.30	11.62	8.50×10^6	B	10
750.34	13.48	11.83	4.50×10^7	B	10
751.46	13.27	11.62	4.00×10^7	B	10
763.51	13.17	11.55	2.45×10^7	B	10

Table 4.3: Ar I wavelengths used on CTH

Table 4.4 shows the list of Ar II wavelengths used on CTH. As in Ar I, wavelengths are excluded in all analysis for a high uncertainty in Einstein A value as well as blending. Wavelengths are also excluded in individual frames when they are too weak to obtain a fit or saturated.

Effort was taken to observe two Ar III lines: 350.27 nm and 348.05 nm. Care was taken to ensure that those two lines would be observable by the spectrometer given the spectroscopic setup. An Ar II line at 351.4 nm was observed, which suggests that the two Ar III lines of interest should be visible. The two lines from Ar III were not observed. Therefore the assumption is made that only singly ionized Argon is present on CTH.

It is not clear whether or not Ar III should be observed. No atomic rates file exists for Ar III, so it is not possible to do a time dependent CRM. The existing ionization balance file is shown to be flawed in Section 3.8.3. Ionization energies are lower for Ar III than for Ar I or Ar II so it should be attainable given the plasma parameters, but it is not clear that a CTH discharge is sufficiently long for Ar III to be created in significant quantities.

λ (nm)	Upper Energy (eV)	Lower Energy (eV)	A Coeff. (s^{-1})	Grade	Grade in %
401.39	19.49	16.41	1.05×10^7	A	3
422.83	19.68	16.75	1.31×10^7	A	3
433.13	19.61	16.75	5.74×10^7	A	3
434.80	19.49	16.64	1.17×10^8	A	3
437.95	19.64	16.81	1.00×10^8	A	3
457.82	19.97	17.26	8.00×10^7	B	10
460.92	21.14	18.45	7.89×10^7	A	3
465.76	19.80	17.14	8.92×10^7	B	10
472.65	19.76	17.14	5.88×10^7	A	3
473.55	19.26	16.64	5.80×10^7	A	3
476.51	19.87	17.26	6.40×10^7	B	10
480.63	19.22	16.64	7.80×10^7	A	3

Table 4.4: Argon II wavelengths used on CTH

ALEXIS plasmas are steady state and repeatable, so it is possible to change the wavelength window over which the observations were taken without changing the plasma conditions. This is contrasted with CTH plasmas which are too short for the wavelength window to be changed during a plasma discharge. The steady state nature of the plasmas coupled with the fact that the spectrometer is absolutely calibrated, means that a wider wavelength window was available and more wavelengths were used. Table 4.5 shows all the wavelengths used on ALEXIS.

4.5 Plasma profiles

4.5.1 CTH profiles

Two main diagnostics on CTH are used for the assessment of plasma profiles: the triple probe described in Section 2.2.2.1 and the interferometer. The triple probe provides

λ	Upper Energy (eV)	Lower Energy (eV)	A Coeff. (s^{-1})	Grade	Grade in %
696.54	13.33	11.55	6.4×10^6	B+	7
714.70	13.28	11.55	6.30×10^5	B+	7
727.24	13.33	11.62	1.83×10^6	B+	7
738.34	13.30	11.62	8.50×10^6	B	10
750.34	13.48	11.83	4.50×10^7	B	10
751.46	13.27	11.62	4.00×10^7	B	10
763.51	13.17	11.55	2.45×10^7	B	10
794.81	13.28	11.72	1.80×10^7	B	10
811.50	13.07	11.58	3.30×10^7	B	10
826.41	13.33	11.83	1.53×10^7	B+	7
840.78	13.30	11.83	2.23×10^7	B+	7
842.38	13.10	11.62	2.15×10^7	B+	7
852.11	13.28	11.83	1.39×10^7	B	10

Table 4.5: Argon I wavelengths used on ALEXIS.

local measurements of plasma parameters whereas the interferometer provides line-averaged measurements. The major drawback of the triple probe as an electron density diagnostic is a significant degree of uncertainty, as discussed in Section 2.6. Furthermore, obtaining a plasma profile from the triple probe requires making multiple plasmas with the same plasma parameters and making an assumption of repeatability. This assumption of repeatability is reasonable for ECRH plasmas, which tend to be relatively stationary.

A comparison can be made between the line integrated and local electron density measurements through the use of V3FIT, a stellarator equilibrium reconstruction code from Auburn University: this tool can be used to construct a crude estimate of the plasma profile from the interferometer data. The profile from the reconstruction can then be compared to a profile built from an ensemble of plasmas with triple probe measurements.

4.5.1.1 Triple probe profiles of plasmas

A number of different plasma parameters are used for this work, and the radial cross section of electron temperature and electron density for a broad range of the plasma parameters follows. Each point is chosen at 1.65 s, although in each case the discharge begins at a different time. In each case every data point obtained is plotted with a 25% uncertainty. For some locations each point is identical. For others there is a spread in measured value. All profiles are fairly flat in both temperature and density.

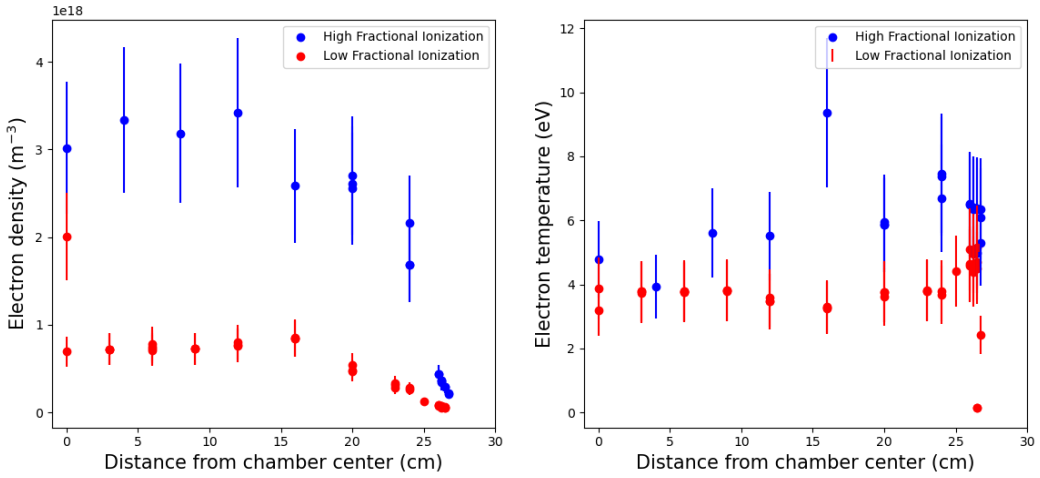

Figure 4.4: Radial profiles of low and high fractional ionization plasmas. The low fractional ionization plasma has a fractional ionization of 43% with an electron density of $1.4\times10^{11}\ cm^{-3}$ and a neutral density of $1.9\times10^{11}\ cm^{-3}$. The high fractional ionization plasma has a fractional ionization of 91% with an electron density of $3.8\times10^{11}\ cm^{-3}$ and a neutral density of $3.7\times10^{10}\ cm^{-3}$.

Fig. 4.4 shows plasmas with varying fractional ionizations. The lower fractional ionization plasma appears to have a spatially wider electron density profile. They have similar electron temperature values, but the higher fractional ionization case has a slight peak towards the edge.

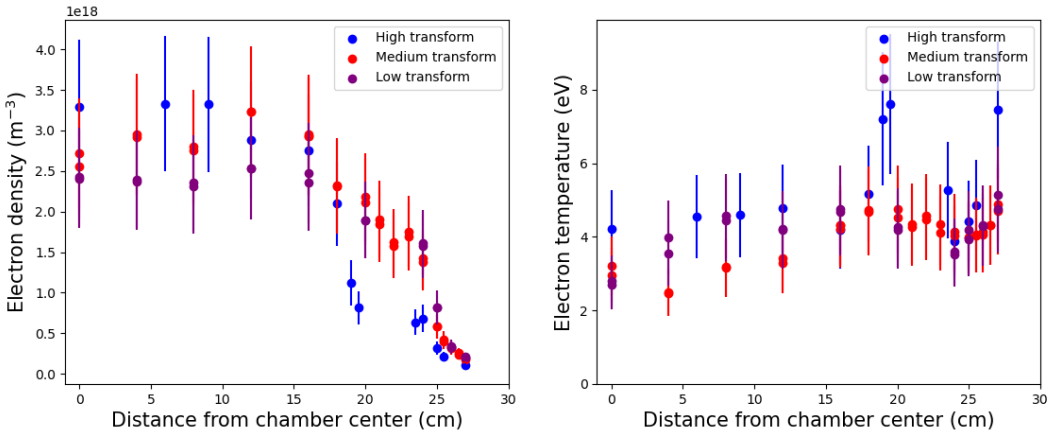

Figure 4.5: Radial profiles of low, medium, and high transform plasmas. No OH current is included in these plasmas. The transforms at the last closed flux surface for the low, medium, and high transform plasmas are 0.06, 0.13, and 0.22 respectively.

Fig. 4.5 shows ECRH only plasmas with varying rotational transforms. The highest transform appears to have a slightly steeper gradiant in electron density. The electron density and temperature profiles otherwise appear similar.

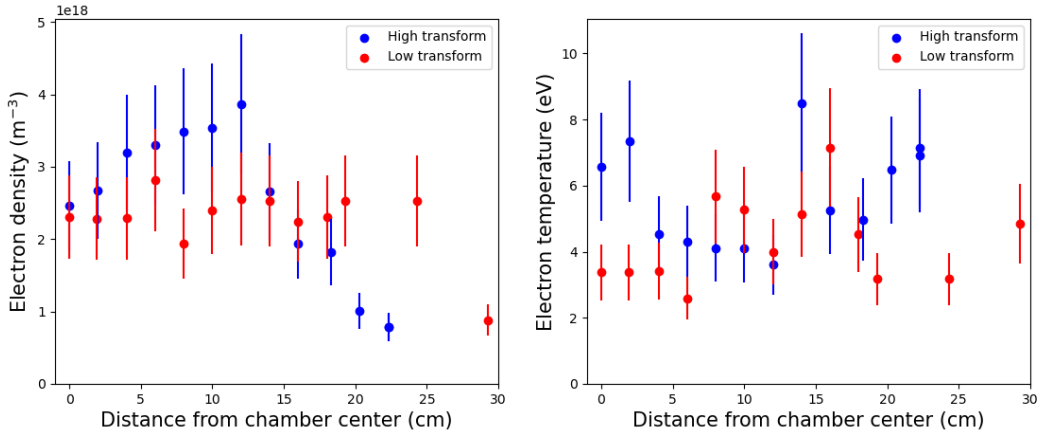

Figure 4.6: Radial profiles of low and high transform plasmas with OH current. The transforms at the last closed flux surface for the low and high transform plasmas are 0.07 and 0.12 respectively.

Fig. 4.6 shows plasmas with varying transforms and OH current. The low transform case shows a flatter electron density profile that extends further to the edge.

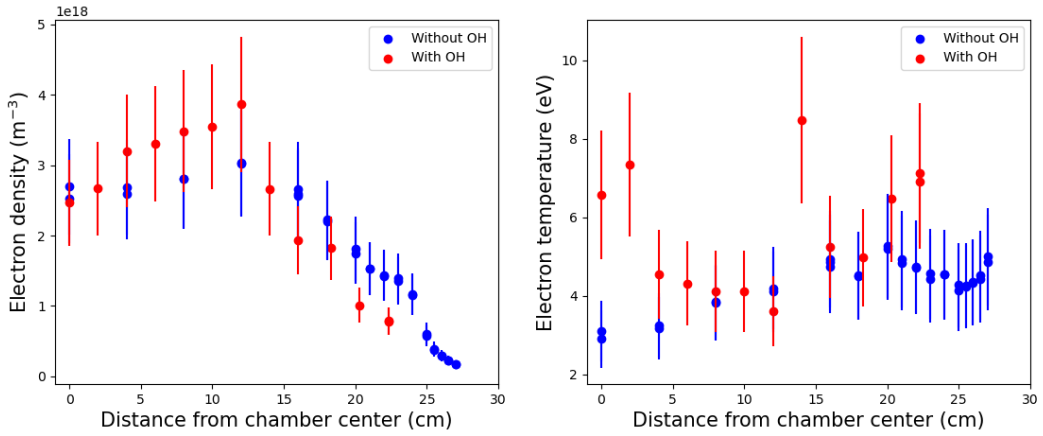

Figure 4.7: Radial pofiles of high transform plasmas, with and without OH current. The transforms with and without OH are 0.12 and 0.13 respectively.

Fig. 4.7 shows two cases of high transform plasmas with and without OH current. The current has no discernible impact on the radial gradient of the electron density profile. In both cases the electron temperature appears lower towards the center than at the edge.

All triple probe profiles are significantly flatter than would be expected if all radial movement were due to diffusion and mobility. Thus we expect that turbulence must be present in the plasma to create these radial profiles.

4.5.1.2 Comparison between triple probe and interferometer data

The triple probe cross section can be compared to the corresponding interferometer data through V3FIT reconstructions. The interferometer paths can be seen in Fig. 2.7a and a representative scan of triple probe sample locations can be seen in Fig. 2.7b. The triple probe can measure the entire radial profile from the magnetic axis to the vacuum chamber wall.

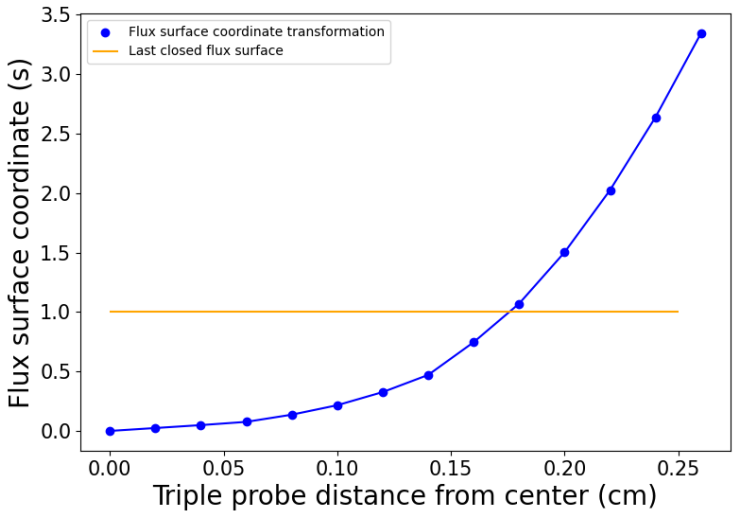

Figure 4.8: Conversion between the triple probe vertical distance from the midplane in cm (z) and the flux surface coordinate (s). The triple probe is located at R=71.1cm. s is not calculated outside of the last closed flux surface, so coordinates shown above s= 1.0 are extrapolated.

Before describing V3FIT it is important to note that the radial coordinate used by V3fit is not Z, rather it is s, a flux surface coordinate system described in Section 2.1. It

is a flux surface based radial coordinate system defined as the toroidal flux through the flux surface of interest normalized to the toroidal flux at the last closed flux surface. Fig. 4.8 can be used to determine the relationship between the vertical position of the triple probe (Z) and the flux surface coordinate (s) for a single magnetic transform. First VMEC coordinates are translated to Cartesian coordinates for a particular transform profile. Then the toroidal position and R position are given as those of the triple probe. Plotted is the vertical displacement (Z) and the corresponding flux surface coordinate (s). In general, both Z and s increase vertically, but the two coordinates do not increase linearly together.

A V3FIT reconstruction is used here to model the local electron density values given the line integrated electron densities. The reconstruction can be performed in a number of ways, but in this case three locations are chosen where the electron density will be defined. The electron density will be set for one of those locations, and the electron density at the other two locations will be chosen by the model. The edge of the plasma (limiting location) will also be set before the model runs.

Two graphs of reconstructions will be shown. The first graph will be used to show how reconstructions are compared to triple probe data. The second graph will show a series of reconstructions on the same plasma discharge with changing input parameters.

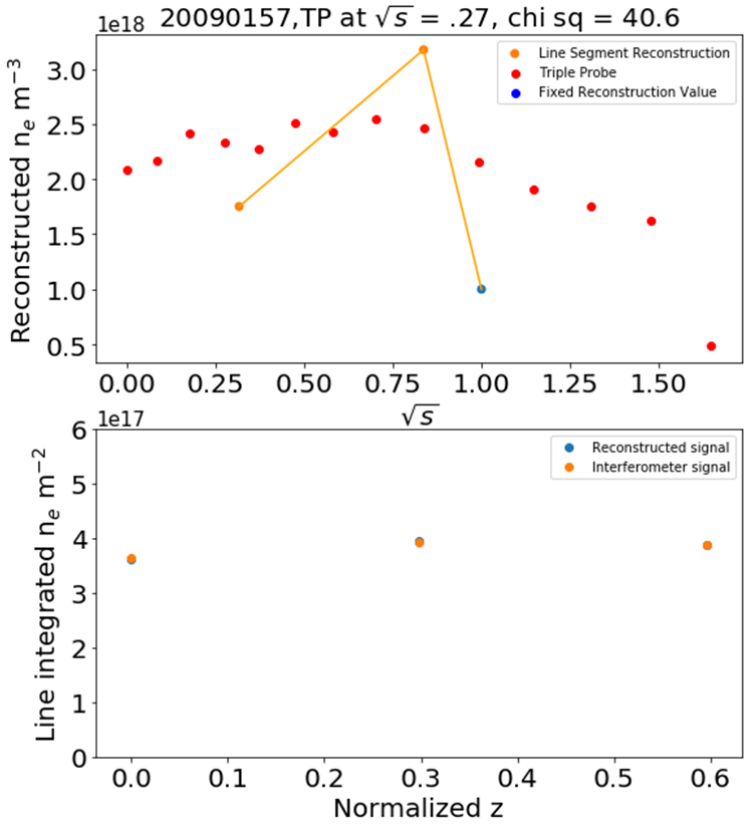

Figure 4.9: Example of one reconstruction compared to triple probe data. The top graph shows a comparison between the reconstructed locations (connected by orange lines), and the values measured by the triple probe (represented by red points). The blue point corresponds to an electron density that is fixed in both position and value. In the case of the orange points, position is fixed but value is permitted to vary. The bottom graph is a comparison between reconstructed line integrated electron density (in blue) and measured line integrated electron density (in orange). The points in the bottom graph are difficult to distinguish due to their proximity. The top graph shows an x axis in units of $\sqrt{s}$, where s is the flux surface coordinate.

Fig. 4.9 shows the result of a single reconstruction as an example. The top graph compares the reconstruction, in orange, to the triple probe radial profile, in red. Obtaining a triple probe profile requires a series of reproducible discharges, whereas the reconstruction relies on a single discharge: the discharge used for the reconstruction is shown when the triple probe is at $\sqrt{s} = 0.27$. The reconstruction result consists of three points, two orange and one blue. The blue point has the position and electron density value fixed. The two orange points have a fixed position, but the value is dictated by the model. The electron

density between the individual points is then given by a straight line. There is more change in the reconstruction electron density than is observed in the triple probe data, suggesting that the two do not agree. A different set of starting positions and dictated electron density will result in a different match between the interferometer and triple probe data.

The bottom graph shows a comparison between the data from the interferometer, in orange, and the reconstructed integrated value, in blue. The two are nearly indistinguishable: while the reconstruction may or may not accurately represent the electron density of the plasma, it does match well with the interferometer data.

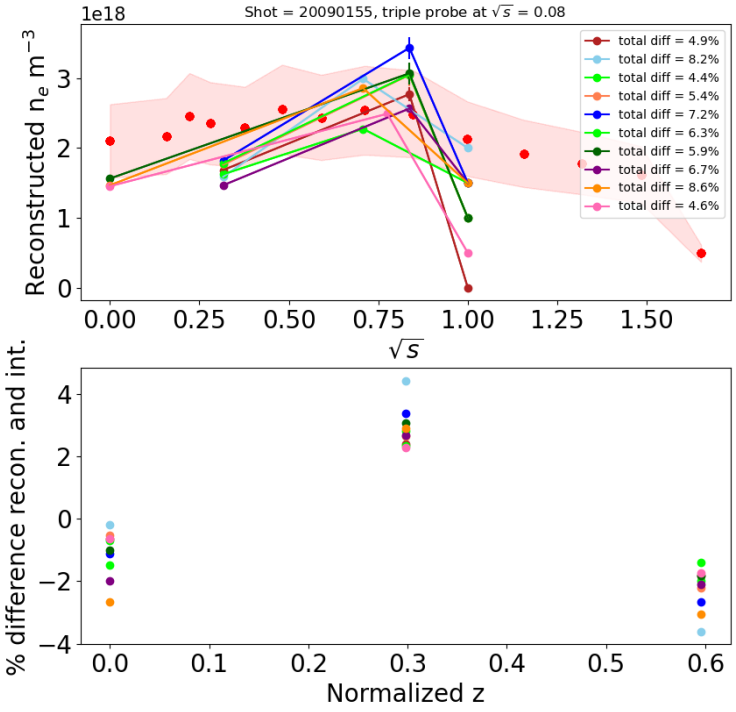

Figure 4.10: Multiple reconstruction attempts of one shot. A triple probe profile error of 25% is shaded in red.

An assessment is performed of various reconstruction attempts of the same discharge. The top graph of Fig. 4.10 shows a comparison between multiple reconstructions of the same discharge. The bottom graph shows the % difference between line-integrated electron densities and the reconstructions. The total % difference on the top graph is the absolute

sum of the individual % differences in the bottom graph. Several reconstructions show a match between triple probe and interferometer values.

CTH is typically a plasma limited in size by limiters within the device, but when only ECRH is used to create a plasma, the plasma extends beyond the limiters. The interferometer density is a line-integrated diagnostic which requires division by a plasma size for a true value. The plasma size used is the size of a plasma that extends to the limiters, but in the case of an ECRH only plasma this becomes a poor assumption. As a result, when the plasma is bigger than estimated, the electron density is lower.

4.5.2 ALEXIS profile

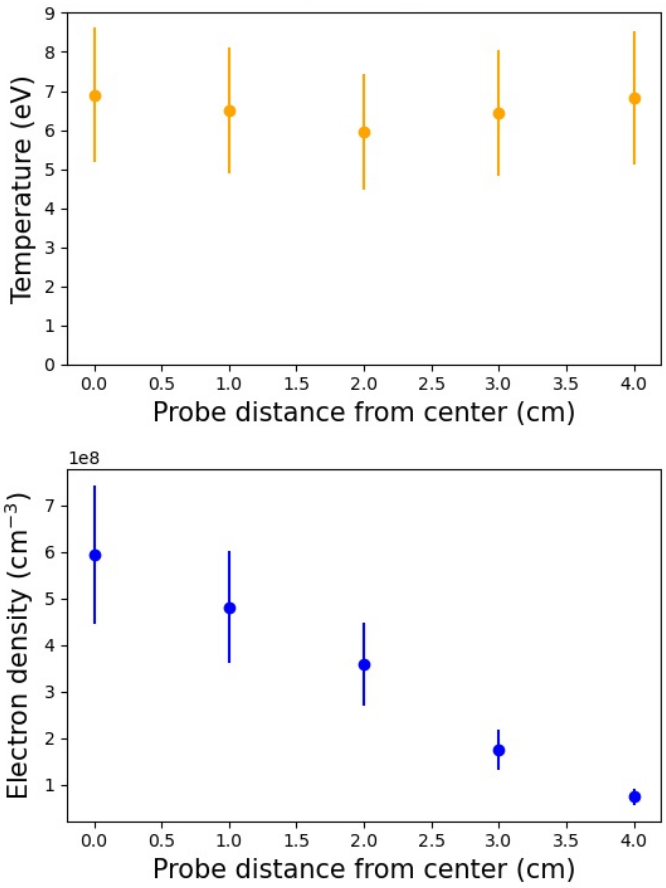

Figure 4.11: Radial scan of Argon plasma on ALEXIS using a single tipped Langmuir probe.

Fig. 4.11 shows the electron temperature and electron density radial profiles of ALEXIS, measured through the use of a single tipped Langmuir probe that scans bias voltage. The electron temperature profile is flat over the entire minor radius of the plasma the chamber. By contrast, electron density falls off radially. The central electron density is used for atomic modeling of the plasma. This may introduce some error in the model and will be discussed later in this chapter. Based on this data, the line-of-sight length of the plasma is considered to be 8 cm for the spectroscopic measurements made here.

4.6 ALEXIS results

Plasmas on ALEXIS play two roles in this thesis. First, ALEXIS plasmas were used to test the importance of considering the time dependence of metastable states in the comparison between synthetic and experimental data. Second, ALEXIS plasmas were used to attempt to benchmark the Ar neutral density diagnostic measurements. The small axial size of the chamber led to short metastable lifetimes. Two ALEXIS sets of experimental results are presented here. The first dataset contains 26 plasmas in which the flow rate, and thus density, of input gas, the input power, and the confining magnetic field are all changed. The purpose of this is to explore the match between the synthetic and experimental spectra. The temperatures for this set of plasmas ranged from 4.1 eV to 8.7 eV, the electron densities from $4.3 \times 10^8\, cm^{-3}$ to $6 \times 10^9\, cm^{-3}$, and neutral densities as measured from the pressure from $6.1 \times 10^{13}\, cm^{-3}$ to $1.2 \times 10^{14}\, cm^{-3}$. The second dataset contains a set of 40 plasmas with varying input gas at 20 W input power and a set of 40 plasmas with varying input gas at 55 W input power. The purpose of this is to show the relationship between the chamber pressure and the spectroscopically estimated neutral density. The temperatures for this set of plasmas ranged from 6.3 eV to 13.5 eV, the electron densities from $4.7 \times 10^8\, cm^{-3}$ to $2.4 \times 10^9\, cm^{-3}$, and neutral densities as measured from the pressure from $1.8 \times 10^{12}\, cm^{-3}$ to $1.6 \times 10^{14}\, cm^{-3}$.

4.6.1 ALEXIS match between model and experiment assuming non-steady-state metastables

Synthetic line ratios were compared to observed line ratios to explore the importance of metastable lifetimes in the atomic model. In obtaining the experimental spectra, two absolutely calibrated spectra were obtained on ALEXIS, one centered at 760 nm and the other at 820 nm. These spectra were absolutely calibrated, and so they could be combined and normalized to one wavelength across the longer combined spectrum. The synthetic spectra depends on three variables: the electron temperature of the plasma, the electron density of the plasma, and the time over which the metastable populations can evolve. Two metastable states exist in neutral Argon, and their population change with time can be modeled with knowledge of the electron temperature and density.

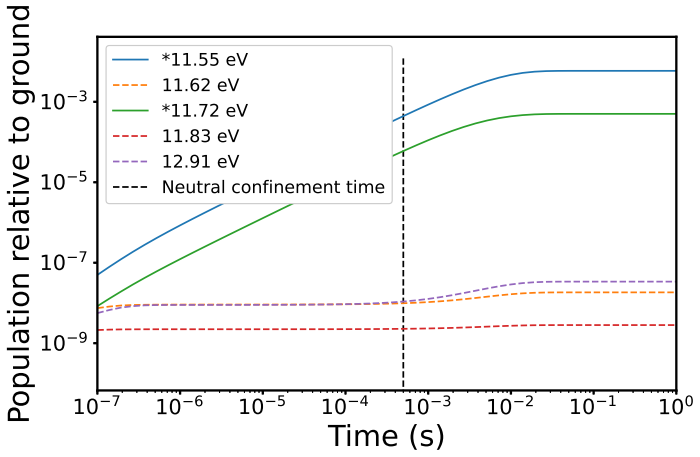

Figure 4.12: Population vs time for lowest 5 neutral argon energy levels. Metastable levels are marked with * and are solid. Non-metastable-states are dashed. Electron temperature is 5.6 eV and electron density is $9.4 \times 10^8\,\mathrm{cm}^{-3}$.

Fig. 4.12 shows the time dependent population of the 5 lowest neutral argon energy levels. The metastable states are solid lines marked with an asterisk, *. The atomic model fundamentally depends on four variables: n_e, T_e, N_{σ_1}, and N_{σ_2}. However, the metastable populations can be predicted by a time: N_{σ_1}, and N_{σ_2} can be replaced by *time*. As a result, the four variable problem can be reduced to a three-variable problem: n_e, T_e, and *time*.

An experiment was performed on ALEXIS in which the confining magnetic field, the input RF power, and the input gas were changed over an ensemble of 26 differing plasmas. For each plasma, the electron temperature and electron density were measured with the single tipped Langmuir probe, described in Section 2.5.2. A series of synthetic spectra were created for each plasma using the electron temperature, electron density, and a range of reasonable neutral Argon lifetimes. Each synthetic spectrum was compared to the real spectrum from the plasma. The time that resulted in the best match was deemed to be a reasonable approximation for the time for neutral atoms to hit the wall.

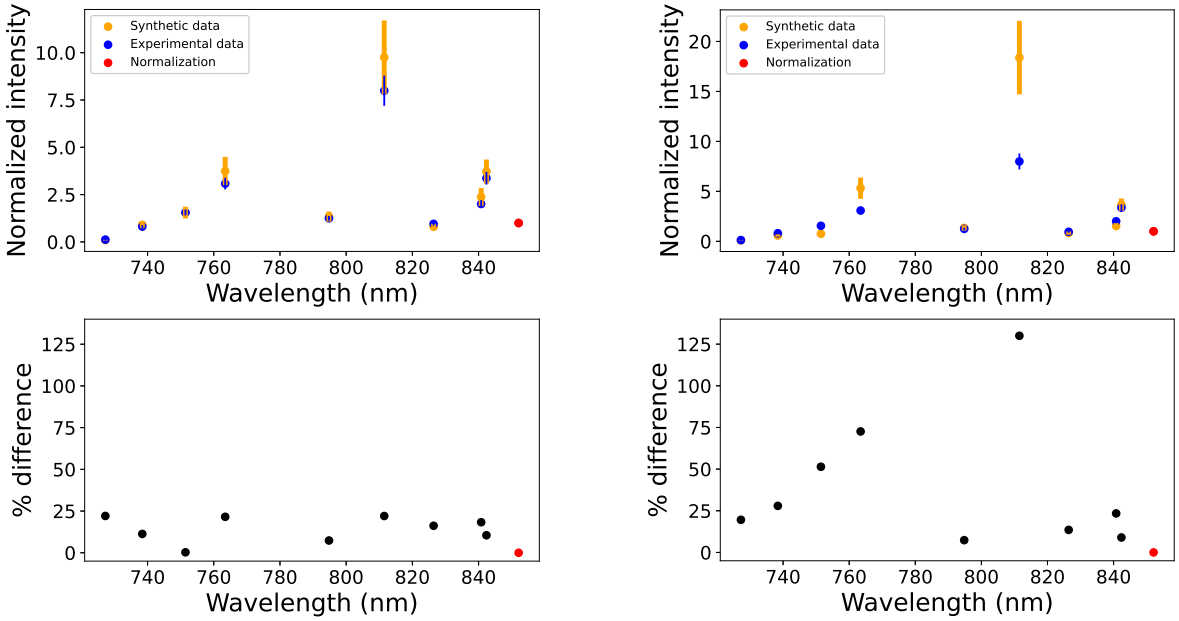

(a) Synthetic vs experimental assuming metastables that have not reached steady state.

(b) Synthetic vs experimental assuming steady-state metastables.

Figure 4.13: Experimental vs synthetic data presented at 3 separate plasma parameters. Experimental ALEXIS spectra in blue, synthetic PEC spectra in orange. All spectra are normalized to the 852.1 nm line. Experimental error bars are all 10%. PEC error bars are the Einstein A coefficient error quoted by NIST [31] (based upon [52, 53]). Electron temperature is 7.3 eV and electron density is $6.6 \times 10^8\,\mathrm{cm}^{-3}$.

An example of this comparison can be seen in Fig. 4.13. The top graph shows a direct comparison between line ratios in blue and orange. All wavelengths are normalized to 852.1 nm, which is shown in red and, as the normalization wavelength, is 1 for both synthetic

and experimental. The synthetic spectrum is shown in orange and the experimental spectrum is shown in blue. The error bars for the synthetic ratios are constructed by combining the percentage errors from both the Einstein A coefficients of both wavelengths. The error bars for the experimental ratios are all 10%, as discussed in Section 2.6. The bottom graph shows the % difference between the synthetic and experimental data and shows a difference under 25% for most wavelengths. The % difference for the normalization wavelength 852.1 nm is again shown in red and is 0.

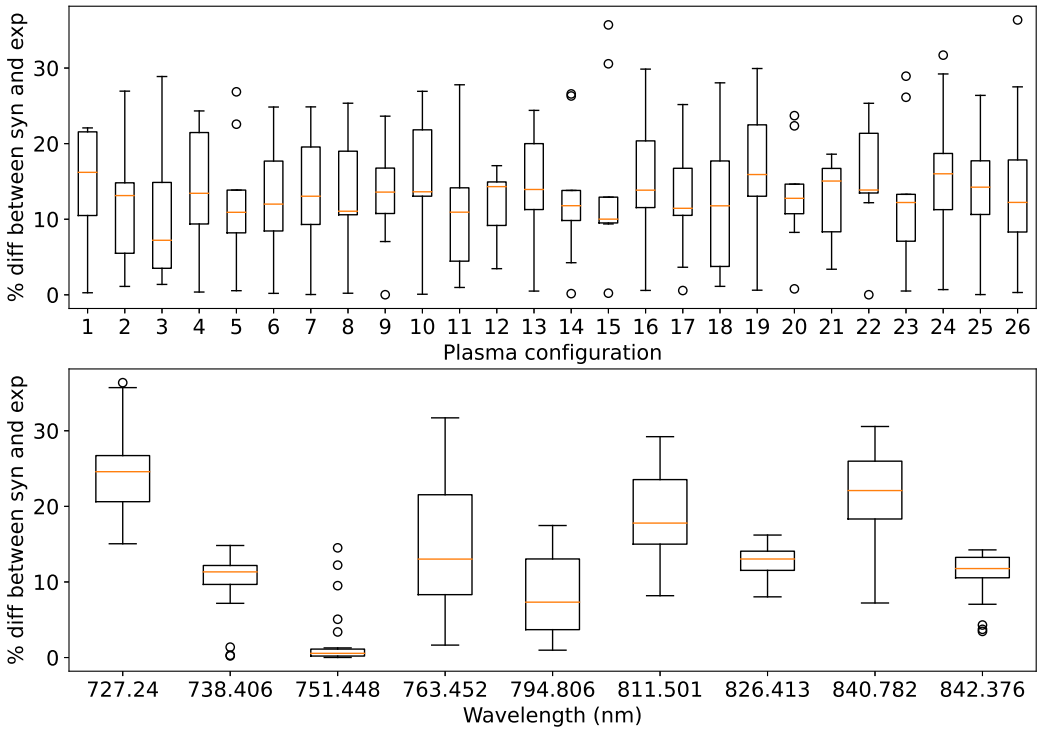

Figure 4.14: Summary of % difference between synthetic and experimental data across all used wavelengths for all 26 plasmas analyzed.

While Fig. 4.13 shows a single comparison between synthetic and experimental line ratios, all 26 plasma configurations were run through this comparison and Fig. 4.14 summarizes the % difference across all plasmas and wavelengths using a box and whisker plot. In the box and whisker plot shown here, the horizontal orange line represents the median

value. The box contains the interquartile range (IQR) or the middle 50% of the data: the lower side of the box represents the lower 25% and the upper side of the box represents the upper 25%. A vertical line connects the box to horizontal lines representing $1.5 \times IQR$. Any values outside $1.5 \times IQR$ are represented as points.

The top plot shows a separate box and whisker plot for each plasma configuration. Each of the bottom box and whisker plots represents 9 separate wavelengths. This graph shows that the median % difference between synthetic and experimental data was consistently below 20%, and no wavelength shows a % difference over 40%. The bottom plot shows a box and whisker plot for each wavelength. Each box and whisker plot represents 26 separate plasma configurations. The 751.45 nm line shows a better match between synthetic and experimental data than the others. The 727.24 nm line shows a poorer match between synthetic and experimental data than the others.

4.6.2 Measurement of neutral density through gas pressure

As mentioned previously, the ALEXIS device was used to benchmark the neutral density diagnostic.

The ideal gas law is used to convert the measured pressure to neutral density on ALEXIS.

$$PV = N_n k_B T_n \tag{4.25}$$

In Eq. 4.25, P represents the pressure of gas in the chamber, V represents the volume of the chamber, N_n represents the number of neutral particles, k_B represents the Boltzmann constant, $1.38 \times 10^{-23}\,(\frac{m^2 Kg}{s^2 K})$, and T_n represents the neutral gas temperature, assumed to be room temperature, $273\,K$.

Both sides are divided by V and N_n becomes n_n:

$$P(Pa) = n_n(m^{-3}) k_B(\frac{m^2 Kg}{s^2 K}) T_n(K) \tag{4.26}$$

Pressure is converted from Pascal to mTorr (1000 mTorr=133 Pascal).

$$n_n(m^{-3}) = \frac{P}{k_B T_n} \tag{4.27}$$

$$n_n(m^{-3}) = \frac{P(mTorr) \times 133(\frac{Pa}{Torr})}{1000(\frac{mTorr}{Torr})} \times \frac{1}{1.38 \times 10^{-23}(\frac{m^2 kg}{s^2 K}) \times 273(K)} \tag{4.28}$$

$$1Pa = 1\frac{kg}{ms^2} \tag{4.29}$$

$$n_n(cm^{-3}) = 3.53 \times 10^{13} P(mTorr) \tag{4.30}$$

There are several challenges anticipated in estimating the neutral density on ALEXIS using the spectrometer measurements. First, ALEXIS did not have a wide range of diagnostics, and the probe used on ALEXIS was closer to the plasma source than the lens. As a result, the electron density is expected to be lower at the lens location than at the probe location. The pressure gauge was at the same axial location as the probe, so the neutral density would be expected to drop further at the location of the spectrometer. This is not taken into account in any of the data analysis. Second, the probe diagnostic that ALEXIS had was a single tipped Langmuir probe which is not RF compensated. As a result, the T_e measurement is less trustworthy. The n_e measurement relies on the T_e measurement and as a result is also less accurate. Third, as described earlier ALEXIS does not have steady state metastables. This introduces "time" as a variable in addition to electron density and temperature.

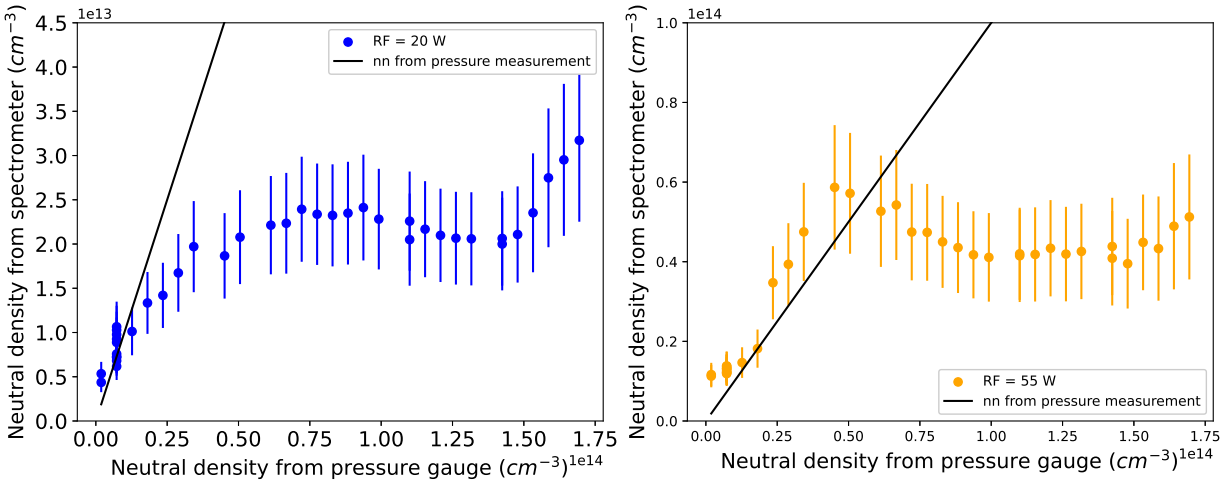

Figure 4.15: Neutral density as measured by both the pressure gauge and the spectrometer.

Fig. 4.15 shows the result of an attempt to benchmark the neutral density diagnostic on ALEXIS. The input gas flow is changed while keeping the input power constant. The x-axis shows neutral density measured by the pressure gauge and the y-axis shows the neutral density measured by the spectrometer. If the two matched perfectly they would line along the black line. The yellow points show the result when the RF power supply is supplying 55 W of power and the blue points show the result when the RF power supply produces 20 W of power. There should be a steady increase in neutral density with an increase in gas, but that is not observed. The spectrometer does not seem to be able to measure a neutral density above $1 \times 10^{13}\, cm^{-3}$. However these initial results suggest that below $1 \times 10^{14}\, cm^{-3}$ there may be agreement between the neutral density diagnostic and the pressure measurement. The reason for this discrepancy is not known, however the primary hypothesis is that the mode of operation changes throughout the pressure regime used.

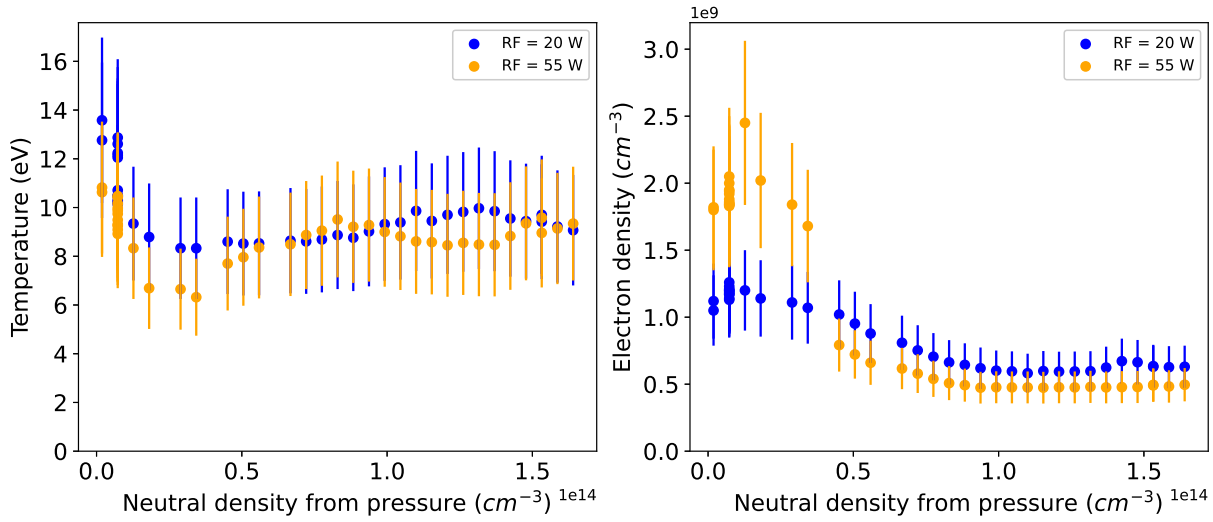

Figure 4.16: Electron temperature and density for the plasmas in which the input gas was changed.

Fig. 4.16 shows the electron temperature associated with the same set of plasmas represented in Fig. 2.2.2.2. These figures show a change in plasma characteristic across the regime used. The electron temperature changes from the lowest neutral densities until approximately $2.5 \times 10^{13}\, cm^{-3}$, at which point the temperature remains somewhat constant. By contrast, the electron density increases then decreases with a change in neutral density, further suggesting a change in mode of operation. This behavior is more extreme for an input power of 55 W than an input power of 20 W.

One final possible explanation that has not been pursued is that the electron density and/or electron temperature radial profile could change aross neutral densities. It is possible that the corresponding plasma parameters measured in the center of the chamber are not those which should be used to model the plasma. More experiments are needed.

Despite the poor match between neutral density from pressure and neutral density from the spectrometer, Fig. 4.14 shows a good match between synthetic and experimental line ratios: no set of plasma parameters provided an average match worse than 20%.

4.6.3 Calculation of Metastable Time on ALEXIS

Metastable states on the ALEXIS device evolve on a slow enough time scale that when modeling them it is not safe to assume that they have reached their steady state values. Instead, it seems likely that a neutral Argon atom in the plasma could have hit the wall, causing them to decay down to the ground state, before the metastables have had time to reach steady state.

Recall Eq. 4.16:

$$D_{\parallel} = (\lambda_{mfp})^2 \nu = \frac{v_{th}}{n_n \sigma},$$

used in conjunction with:

$$t = \frac{(L)^2}{D}.$$

Neutral particles do not interact with the magnetic field, and so parallel diffusion is used. The neutral Argon thermal velocity, assuming room temperature atoms, is $v_{th} \approx 3.94 \times 10^4\, cm$ [54] and neutral-neutral collisional cross section $\sigma = 1 \times 10^{-14}\, cm^2$ [51] are fixed, along with the distance to the wall $L = 5\, cm$. Combining all terms, the time to the wall is:

$$t = \frac{(L)^2 n_n \sigma}{v_{th}} = \frac{25\,(\mathrm{cm}^2) \times n_n\,(\mathrm{cm}^{-3}) \times 1 \times 10^{-14}\,(\mathrm{cm}^2)}{3.94 \times 10^4\,(\mathrm{cm/s})} = 6.34 \times 10^{-17} \times n_n\,(\mathrm{s}). \quad (4.31)$$

A representative neutral density on ALEXIS is $n_n = 1 \times 10^{13}\, cm^{-3}$, which corresponds to a time of of $6.3 \times 10^{-4}\, s$, or 0.6 ms. By contrast, Fig. 4.12 shows a population vs. time graph of the lowest 5 neutral Argon energy states under typical ALEXIS plasma conditions, showing the time-to-steady-state for metastable states on ALEXIS to be closer to 0.01 ms.

On the x-axis is the time found through a best fit across all available wavelengths. On the y-axis is the time found through the diffusion calculation in Eq. 4.31

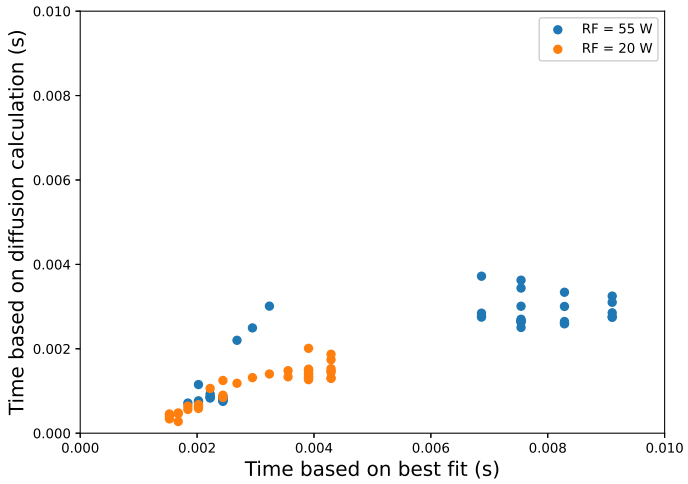

Figure 4.17: Characteristic times for plasmas in which only gas is changed.

Fig. 4.17 shows a comparison between two approaches to finding the characteristic time for ALEXIS plasmas.

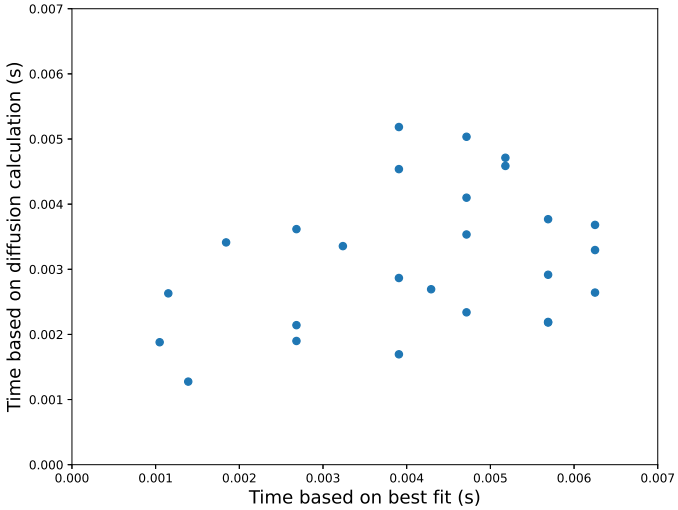

Figure 4.18: Characteristic times for plasmas in which all variables are changed.

The similarity between the two times from very different sources bolsters both.

4.7 CTH results

As can be seen in Fig. 4.19, metastable states on CTH have a chance to reach steady state. As a result, the analysis of CTH data is comparatively simple.

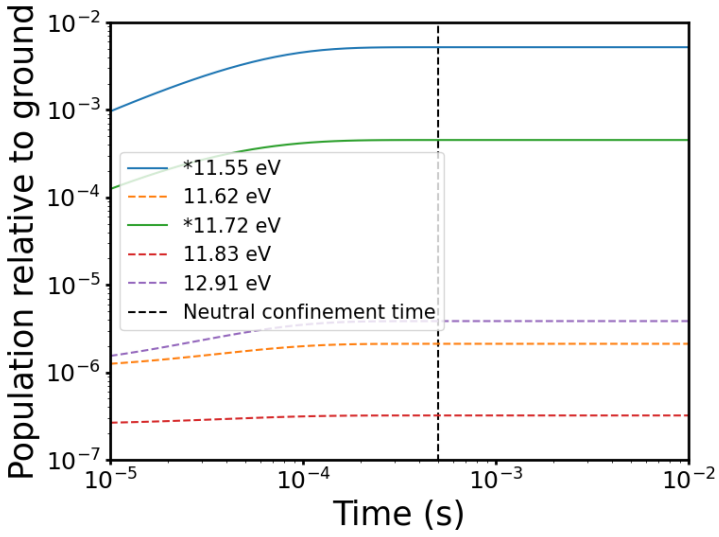

Figure 4.19: Time dependent populations for the lowest 5 energy levels of CTH-relevant Argon plasmas. Metastable states are marked with *.

4.7.1 CTH temperature and density dependence

Power and particle balance play a crucial role in the expected dependence of electron temperature and electron density on input power and input neutral density. A cylindrical model is used to estimate this dependence [55]. Maxwellian electrons are assumed, absorbing Power P_{abs}. A uniform electron density distribution is assumed in the bulk plasma, with the electron density falling off sharply close to the edge. This assumption is reflected in the electron density radial profiles measured by the triple probe.

The first equation used is particle balance:

$$\begin{aligned} n_e u_B A_{eff} &= K_{iz} n_n n_e \pi R^2 L [55] \\ u_B A_{eff} &= K_{iz} n_n \pi R L^2 \end{aligned} \tag{4.32}$$

Eq. 4.32 shows the particle balance within a plasma. u_B is the Bohm velocity, A_{eff} is the surface area of a volume of plasma, K_{iz} is the ionization rate which, along with elastic scattering and excitation rates, depends strongly on the electron temperature. This dependence is shown in Fig. 4.20, which is based on the equations in Table 4.6. The neutral density is n_n and R^2L is the volume of the plasma. The left side of Eq. 4.32 shows electrons leaving the plasma through a cylinder of area A_{eff} whereas the right side shows electrons being created through collisions between electrons and neutrals in an volume of size $\pi R^2 L$.

Reaction	Ratio coefficient value
Elastic scattering	$2.336 \times 10^{-14} \times T_e^{1.609} \times e^{0.0618(ln(T_e))^2 - 0.1171(ln(T_e))^3}$
Excitation	$2.34 \times 10^{-14} \times T_e^{0.59} \times e^{-17.44/T_e}$
Ionization	$2.48 \times 10^{-14} \times T_e^{0.33} \times e^{-12.78/T_e}$

Table 4.6: Rate coefficients (K) from Lieberman Lieberman and Lichtenberg [55] Table 3.3.

Table 4.6 show sample rate elastic scatter, excitation, and ionization rate coefficients [55].

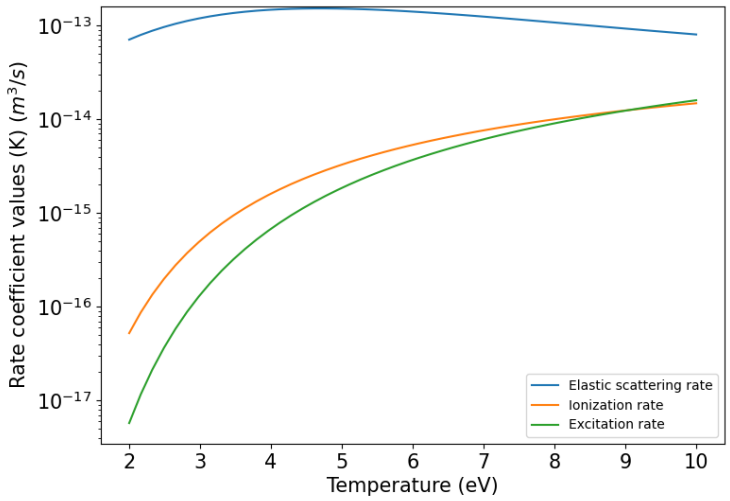

Figure 4.20: Elastic, excitation, and ionization collision rates from Table 4.6. Elastic scattering happens at a much higher rate than ionization or excitation.

The plasma electron temperature appears in Eq. 4.32 through the rate coefficients shown in Table 4.6, but no electron density dependence is present in the particle balance. As a result, a change in neutral density would be expected to impact the electron temperature, but not the electron density.

The lack of electron density dependence of the particle balance equation enables it to be used to calculate electron temperature from neutral density. With electron density in hand, the power balance equation can be used to estimate the electron density from the absorbed power.

$$P_{abs} = u_B e n_e A_{eff} \epsilon_T [55] \tag{4.33}$$

Eq. 4.33 shows the power balance of the plasma. The power absorbed by the plasma is P_{abs}, u_B is the Bohm velocity, e is the electron charge, n_e is the electron density, A_{eff} is the surface area of a volume of plasma, and ϵ_T is the energy lost per ion-electron pair. A change in power is expected to have an impact on the electron density.

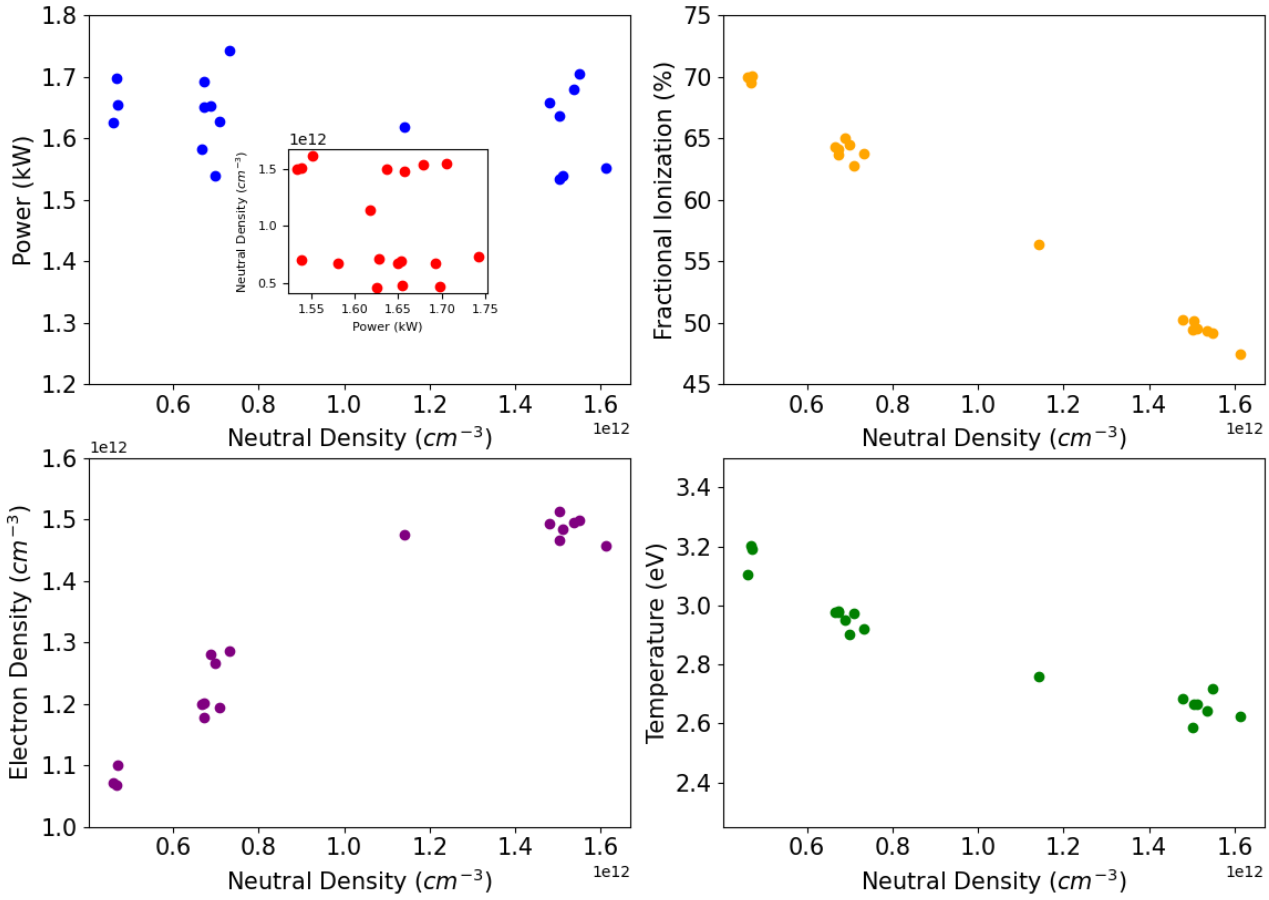

Figure 4.21: Results within CTH of changing input gas without changing input power.

Fig. 4.21 shows the result of keeping the input power as constant as possible while changing the neutral density. This result differs somewhat from the result expected from particle balance: temperature drops, as predicted by particle balance, but electron density increases, a result which is not predicted by particle balance.

The inset graph in the upper left graph also shows that the estimated neutral density does not change with power. The neutral density measurement depends on a model with electron temperature and density inputs, and there is some concern that the calculated value might change with electron temperature and density.

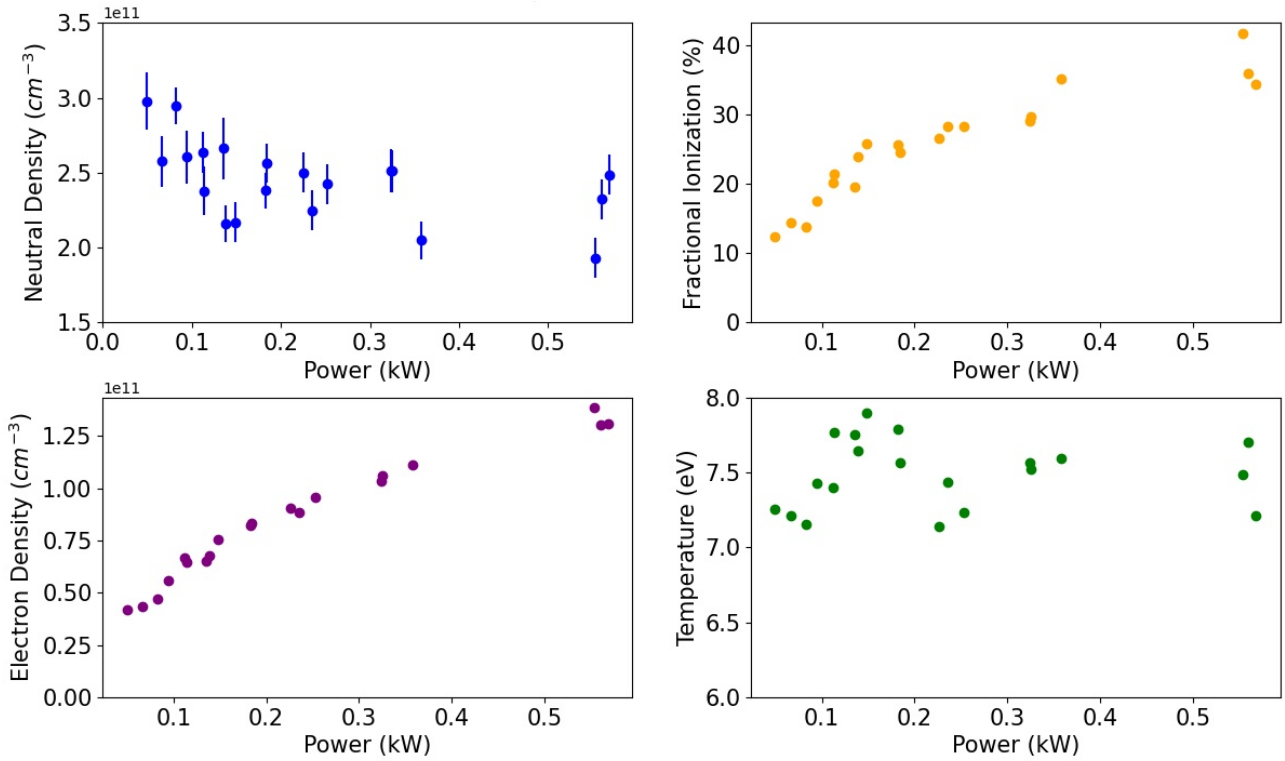

Figure 4.22: Results within CTH of changing input power without changing input gas.

Fig. 4.22 shows the result of keeping the input gas constant while changing input power. Neutral density changes because increasing power allows for more ionization without a change in the electron temperature, consistent with the conclusion from the power balance equation.

4.7.2 Validating neutral density diagnostic on CTH

There are three metrics presented to show that the neutral density diagnostic accurately measures the neutral density of CTH. First, agreement between synthetic and experimental spectra shows that the atomic model being used for the diagnostic well represents the plasma. Second, there is similarity in the neutral density calculated from various wavelengths. Finally, there is no change in the combined electron and neutral density with a change in power. As power is increased, there will be an increase in electron density with a corresponding decrease

in neutral density. In absence of Ar II, the combination of electron and neutral densities should remain constant.

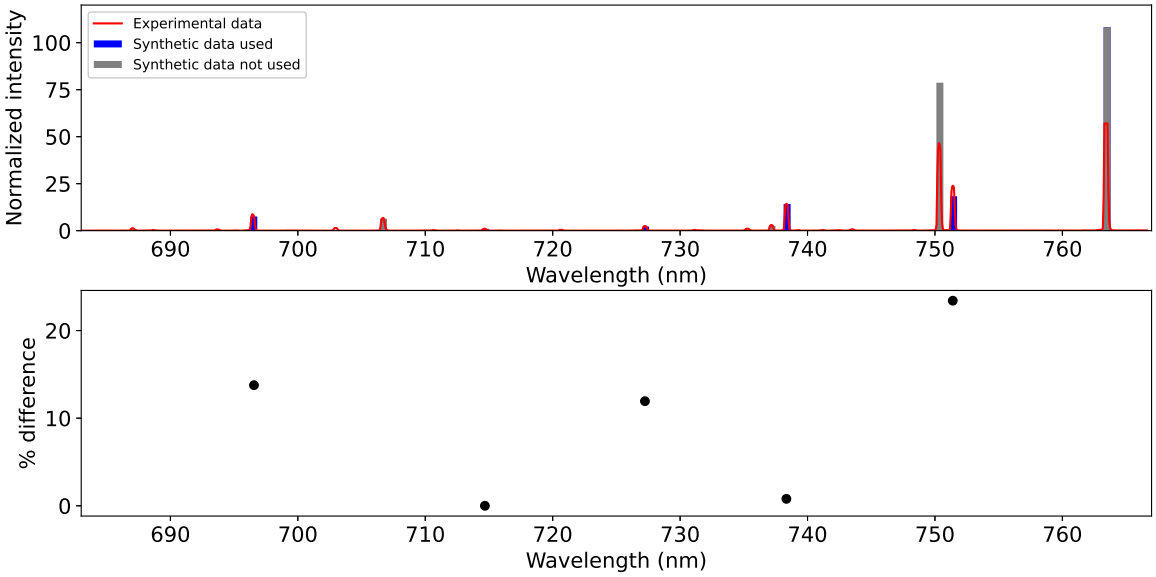

Figure 4.23: Experimental vs synthetic line ratios on CTH. Lines are normalized to 738.34 nm. The top graph shows the experimental data in red, the used synthetic lines in blue, and the synthetic lines that are not used in grey. The bottom graph shows the % difference between the synthetic and experimental data.

First, Fig. 4.23 shows less than 20% difference between relative line intensities of synthetic and experimental spectra. The agreement suggests the validity of the atomic model for use with the plasma. 706.7 nm line is excluded from this analysis due to potential blending with another Ar I line, 706.9 nm. Unfortunately, 706.9 nm has a low Einstein A value. 750.3 nm excluded to due to a consistently poor match between experimental and synthetic data. The cause of the poor match is not known. It is not due to blending as the synthetic data predicts a higher intensity than is observed. The lack of agreement is observed on both CTH and ALEXIS experiments. There is no obvious atomic physics motivation for the poor agreement. 763.5 nm is excluded due to the signal being saturated. The remainder of lines are excluded due to insufficient signal.

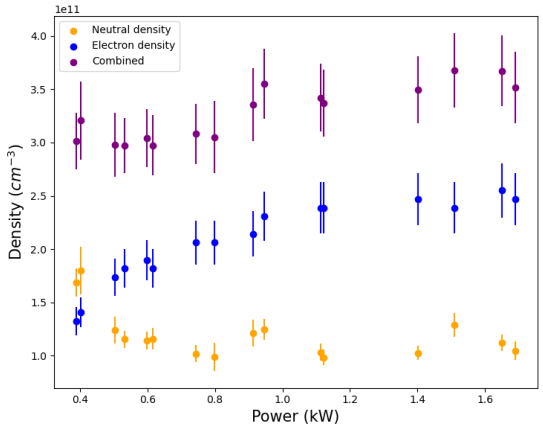

Figure 4.24: Neutral and electron density measured in plasmas with constant input gas but changing power. Neutral density uncertainty comes from variation across wavelengths. Electron density uncertainty is 10%.

Finally, Fig. 4.24 shows no observed change in the combined electron and neutral density with a change in power. As power is increased, there will be an increase in electron density with a corresponding decrease in neutral density. In absence of Ar II, the combination of electron and neutral densities should remain constant.

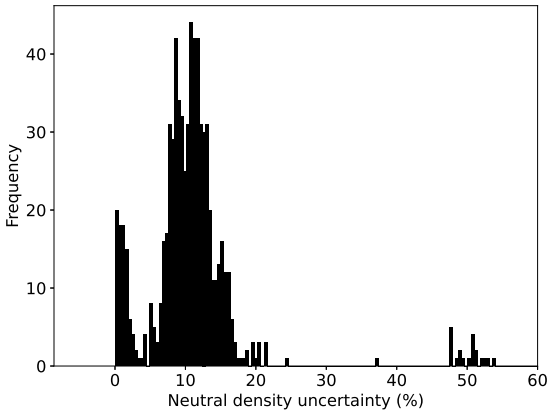

Figure 4.25: The range of uncertainties measured in neutral density, where uncertainty is determined through the standard deviation across all used wavelengths. 461, or 93%, of the 492 plasmas measured have an uncertainty under 20%.

Third, each wavelength separately calculates a value for neutral density, and a small range is observed in calculated neutral densities. Fig. 4.25 shows the range and frequency

in uncertainties measured for all plasmas on CTH, and 93% of the spectra show a standard deviation across the plasmas under 20%. This does not take into account any systemic errors: it is simply the result of calculating the standard deviation across all wavelengths used for the neutral density being measured.

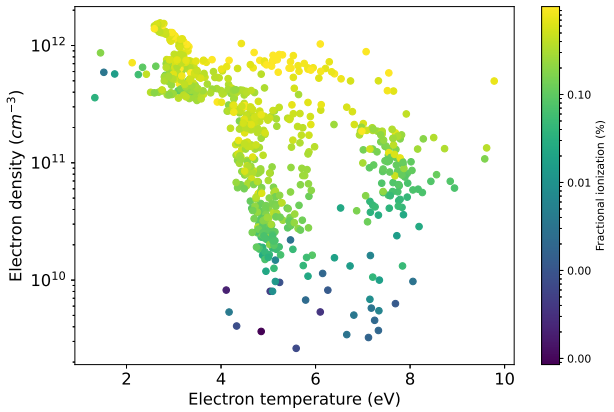

Figure 4.26: The full parameter space achieved on CTH with low temperature Argon plasmas measured the neutral density. x axis corresponds to the electron temperature as measured by the triple probe. y axis corresponds to the electron density as measured by the interferometer. Colorbar shows the fractional ionization. The fractional ionizations measured on CTH range from 0.003% to 99.8%.

Fig. 4.26 shows the range of plasma parameters obtained. Electron temperatures range from 1.33 eV to 9.78 eV. Electron densities range from $3.6 \times 10^9\,\mathrm{cm}^{-3}$ to $1.6 \times 10^{12}\,\mathrm{cm}^{-3}$. Neutral densities range from $1.8 \times 10^9\,\mathrm{cm}^{-3}$ to $8.4 \times 10^{14}\,\mathrm{cm}^{-3}$. Fractional ionizations range from 0.003% to 99.8%, with fractional ionization is defined here as $\frac{n_e}{n_e+n_n}$.

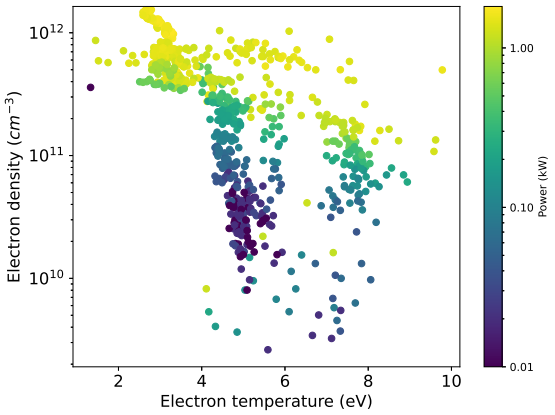

Figure 4.27: The full parameter space achieved on CTH with low temperature Argon plasmas measured the neutral density. x axis corresponds to the electron temperature as measured by the triple probe. y axis corresponds to the electron density as measured by the interferometer. Colorbar shows the ECRH power within every frame of plasma. The ECRH power ranges from 0.1 to 1.0 kW.

Fig. 4.27 shows the range of plasma parameters obtained along with the average ECRH power during the frame in question. Higher input powers correspond to higher electron densities, with high electron temperatures achievable with any input power.

4.8 Neutral density diagnostic used to estimate resistivity on CTH

Neutral density has been measured on CTH for Ohmic plasmas with small amounts of current, and the resistivity can be measured for these plasmas. Two types of collisions are considered the the investigation of resistivity here: coulomb collisions and collisions between electrons and neutrals. Only resistivity parallel to B matters here: resistivity perpendicular to B does not impact the measured current or voltage. Resistivity from Coulomb collisions, also known as Spitzer resistivity, is shown in Eq. 4.34 [4].

$$\eta_{Spitzer/Coulomb} \approx \frac{\pi e^2 m^{1/2}}{(4\pi\epsilon_0)^2 (KT_e)^{3/2}} = 0.0052 \times \ln\Lambda \times T_e^{-3/2}\ \Omega\, cm \tag{4.34}$$

The Coulomb Logarithm, $\ln\Lambda$, is estimated to be 10. Eq. 4.35 refers to the resistivity resulting from collisions between neutrals and charged particles, either ions or electrons:

$$\eta_{Neutral} = \frac{m_e \nu}{n_e e^2} = \frac{m_e n_n \sigma_n v_{th}}{n_e e^2}. \tag{4.35}$$

The collision frequency, ν, is defined in Eq. 4.8. While both ions and electrons collide with neutrals, only electron collisions are considered here. While the ion-neutral collisional resistivity would be predicted to be higher than that for electrons, the ion current is assumed to be negligible due to the large mass of the ions compared to the electrons.

Finally, resistivity can be turned into resistance through:

$$R = \frac{\eta L}{A} \tag{4.36}$$

For this calculation, CTH is considered to be a cylinder with length of 465 cm and a cross sectional area of 908 cm^2. In modeling ohmic plasmas, we consider Ohm's law:

$$V = IR + \frac{d}{dt}(LI). \tag{4.37}$$

Resistance, as discussed above, is caused by both Coulomb collisions and collisions with neutral particles:

$$V = I * \frac{\pi e^2 m^{1/2}}{(4\pi\epsilon_0)^2 (T_e)^{3/2}} + I * \frac{m_e^{1/2} n_n T_e^{1/2} \sigma_n}{n_e e^2} + \frac{d}{dt}(LI) \tag{4.38}$$

First we focus on the $\frac{d}{dt}(LI)$ component:

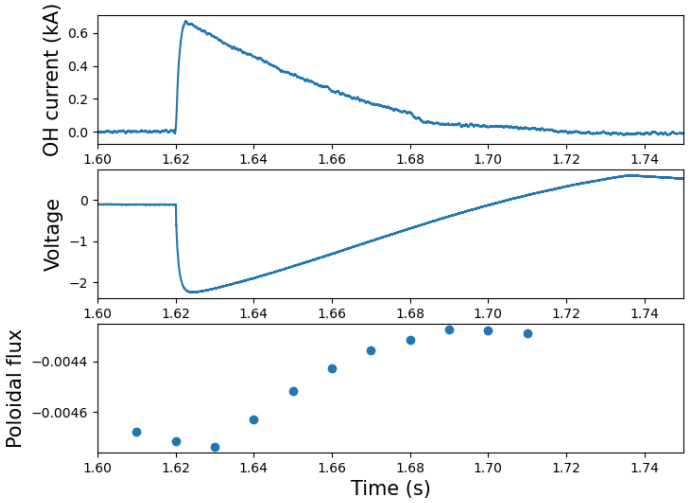

Figure 4.28: Current, poloidal voltage, and poloidal flux of a representative plasma. Change with time of poloidal flux can be compared to total poloidal voltage to determine the importance of considering the $\frac{d}{dt}(LI)$ component.

Fig. 4.28 shows the poloidal flux during a representative low current CTH plasma. The maximum voltage achieved is $-2.24\,V$. The change in flux is $-0.0042\,V$, significantly smaller than the voltage measured. Thus this component can be disregarded.

We return to Ohm's law and ignore the inductance component, focusing on the resistance. Both components of resistance, Coulomb and electron-neutral, are modeled as a constant with a dependence on a measured plasma parameter:

$$\begin{aligned} V &= I * \frac{R_0 n_n K}{n_e} + I * \frac{R_1}{T_e^{3/2}} \\ K &= \sigma_n v_{th} \end{aligned} \tag{4.39}$$

The rate coefficient K is described in Table 4.6 and graphed in Fig. 4.20. It is dependent on the plasma electron temperature.

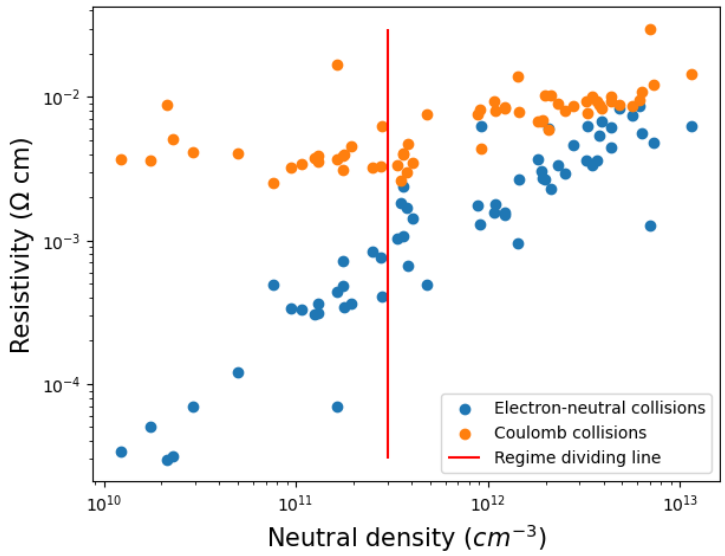

Figure 4.29: Resistivity vs. neutral density for each Ohmic plasma available. Shown here are resistivity resulting from both Coulomb collisions and collisions with neutrals.

Fig. 4.29 shows the parallel theoretical resistivity calculated for each Ohmic plasma available. Coulomb resistivity, shown in blue, does not explicitly depend on neutral density. However, it depends implicitly on neutral density, as Fig. 4.21 shows that an increase in neutral density is shown to result in a decrease in electron temperature due to power balance. By contrast, electron neutral resistivity increases significantly with neutral density. An explicit dependence on neutral density is compounded by an implicit dependence on neutral density through the decrease in neutral density with an increase in plasma density. Two regions are observed in Fig. 4.29. Coulomb resistivity dominates in much of the neutral density regime achieved on CTH, but both become important in a higher neutral density regime. Using all Ohmic plasmas proved impossible: when Coulomb collisions dominated, as is the case in most of the plasmas, the calculated best fit proved to be non-physical. The solution was to select only the those for which the two are expected to be comparable. This was accomplished by only modeling using plasmas with neutral densities above $3 \times 10^{11} cm^{-3}$.

A total of 41 frames of data are used to model ohmic plasmas. 31 frames are used to determine the R_0 and R_1 coefficients, with 10 frames leftover to test those coefficients.

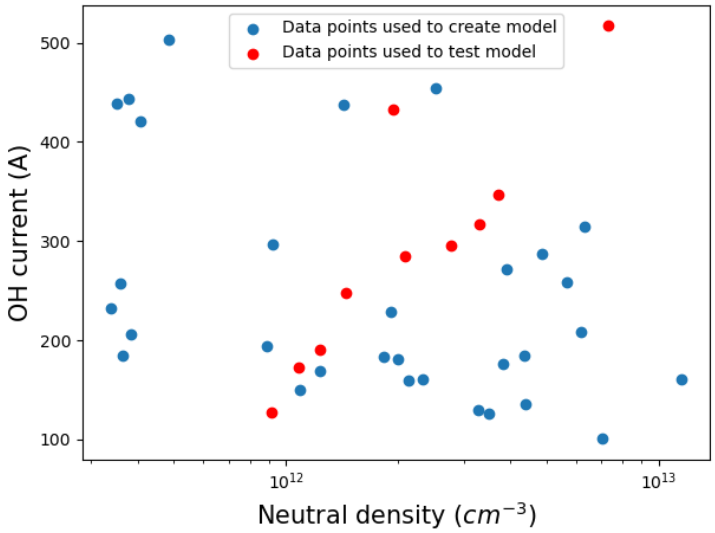

Figure 4.30: Breakdown of data used for assessing Ohmic plasmas.

Fig. 4.30 shows the breakdown of datapoints used to create the model and points used to test the model. Points are not chosen at random: there are so few points that a random distribution of points to test the model does not give a sufficiently uniform distribution of points to test in every region of interest.

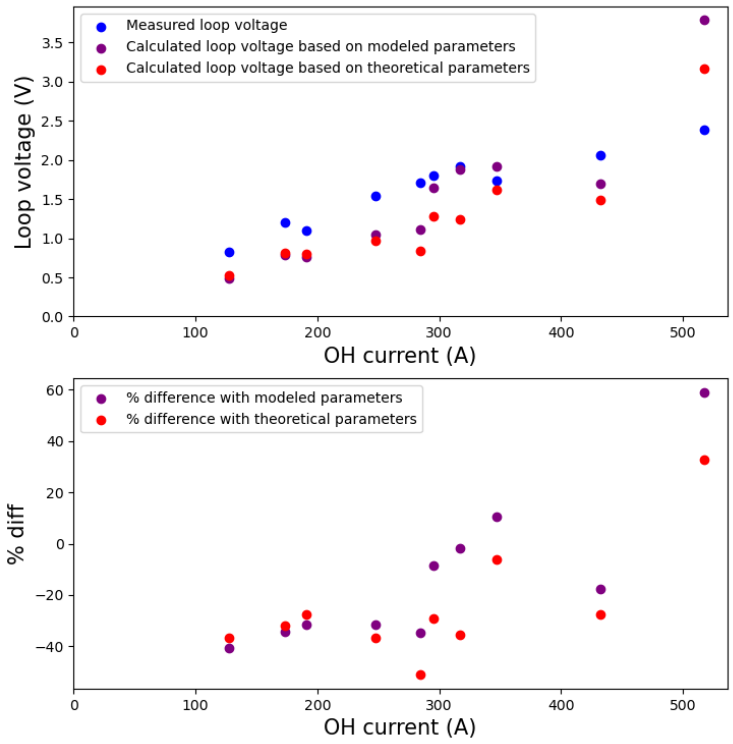

Figure 4.31: The top graph shows a comparison between the measured loop voltage in blue, the calculated loop voltage based on modeled parameters in purple, and the calculated loop voltage based on theoretical parameters in red.

The top graph in Fig. 4.31 shows a comparison between the true loop voltage in blue, the loop voltage predicted by the model in purple, and the loop voltage predicted by theoretical parameters in red. The bottom graphs shows the % difference between the measured loop voltage and modeled parameters in purple and measured loop voltage and modeled parameters in red. There is more data tested between 100 A and 400 A than above 400 A. This is because the data tested is representative of the data available, and there is less data available above 400 A.

There is reasonable agreement between the two, suggesting that the estimated coefficients are a good match to the plasma. Furthermore, the calculated coefficient for the Coulomb resistivity is 0.026, whereas the modeled coefficient is 0.021. The calculated coefficient for the resistivity from electron-neutral collisions is 8.08×10^8 whereas the modeled coefficient is 2.07×10^9. There are two important take-aways from this result. First, this

lends confidence to the neutral density diagnostic. Second, this shows the diagnostic being used to model the plasma.

Chapter 5

Summary and future work

5.1 Summary

The primary result of this thesis is the development and implementation of a spectroscopic neutral density diagnostic on CTH. Three factors lead to the conclusion that this diagnostic is successful. First, there is overlap between synthetic and experimental line ratios, suggesting the validity of the model. Second, the vast majority of the neutral densities measured produce a standard deviation across available wavelengths of under 20%. Third, there is a decrease in neutral density and little change in the combination of neutral and electron density with an increase in power when input gas is kept constant.

The secondary conclusion of this thesis lies in the analysis of metastable states on ALEXIS. A comparison between synthetic and experimental data on ALEXIS has shown that the assumption of time dependence for metastable states is crucial. Unlike CTH, excited states of neutral Argon on ALEXIS do not have enough time to reach steady-state before reaching the wall and returning to ground. Assuming short-lived metastable states significantly improves the match between synthetic and experimental spectra.

The final result of the thesis is the success in using the neutral density diagnostic to model Ohmic plasmas on CTH. The resistivity of the plasma arises from both Coulomb collisions and collisions between electrons and neutral particles. Reasonable agreement was observed between the measured loop voltage on CTH, the calculated loop voltage based on modeled parameters, and the calculated loop voltage based on theoretical parameters.

The spectroscopic neutral Argon density diagnostic on ALEXIS faces a number of challenges, described in Section 4.6.2. It is possible that neutral-neutral collisions are important

or that more complex plasma effects need to be considered. As a result, further work is required for the development of a neutral Argon density diagnostic on ALEXIS. However, the importance of the role of metastable states on ALEXIS has been demonstrated and should help to guide studied of other plasmas.

While all evidence points to the Ar I atomic dataset being of sufficiently high accuracy for spectral diagnostics, the Ar II dataset shows a poor agreement with CTH data. This is likely due to the dataset only being LS resolved, while CTH requires a dataset that is J resolved. The feedback to ADAS from this dissertation provided part of the motivation for a new calculation on Ar II currently underway at Queen's University at Belfast.

Possible Ar I line ratio diagnostics for T_e and n_e on CTH were explored, but no available line ratios showed enough sensitivity to be used.

5.2 Future work

With the ability to measure fractional ionization, CTH is an invaluable testbed for plasma physics that depends on neutral density. A prime example of this is Cowling Resistivity, which depends explicitly on both electron and neutral density. Another example is Alven wave dynamics. Future work on CTH will involve investigating the role of neutral density on these plasma effects.

There is currently a poor match between synthetic and experimental data on CTH for Argon II, and the primary expectation for why lies in atomic rates that are not resolved among J values. A new calculation of these rates would provide an opportunity to test theory against experiment. This calculation would provide better benchmarking for the experiment on CTH: a match between the density of ionization argon and the electron density would further confirm the successful implementation of the neutral density diagnostic.

Neutral density can be measured on CTH at various vertical windows, leading to the possibility of future experimentation. Measuring neutral density at various windows could be used to test the assumption of uniformity. A lack of uniformity could result from a decrease

in neutral density around regions in the chamber where ECRH heating occurs. Similarly, neutral density could be measured at various toroidal locations around the plasma to test the toroidal neutral density uniformity.

The use of the neutral density on ALEXIS proves an ongoing question, and more work should be done to determine cause of the poor match between the pressure gauge on ALEXIS and the spectroscopic neutral density result. Furthermore, it would be valuable to measure neutral density on ALEXIS at lower pressure values, where preliminary results show a better match between the pressure gauge and the spectrometer.

References

[1] D Eldon, E Kolemen, J L Barton, A R Briesemeister, D A Humphreys, A W Leonard, R Maingi, M A Makowski, A G Mclean, A L Moser, and P C Stangeby. Controlling marginally detached divertor plasmas. *Nuclear Fusion*, 2017. doi: 10.1088/1741-4326/aa6b16.

[2] M. S. Yalim, A. Prasad, N. V. Pogorelov, G. P. Zank, and Q. Hu. Effects of Cowling Resistivity in the Weakly Ionized Chromosphere. *The Astrophysical Journal*, 899(1):L4, 8 2020. ISSN 20418213. doi: 10.3847/2041-8213/aba69a.

[3] C. J. Weng, L. C. Lee, C. L. Kuo, and C. B. Wang. Effects of ion-neutral collisions on Alfvén waves: The presence of forbidden zone and heavy damping zone. *Physics of Plasmas*, 20(3), 3 2013. ISSN 1070664X. doi: 10.1063/1.4796043.

[4] Francis F Chen. Langmuir Probe Diagnostics, 2003.

[5] Isabell Plattfaut, Manuela Besser, Anna Lena Severing, Ewa K. Stürmer, and Christian Opländer. Plasma medicine and wound management: Evaluation of the antibacterial efficacy of a medically certified cold atmospheric argon plasma jet. *International Journal of Antimicrobial Agents*, 57(5), 5 2021. ISSN 18727913. doi: 10.1016/j.ijantimicag.2021.106319.

[6] Akikazu Sakudo, Yoshihito Yagyu, and Takashi Onodera. Molecular Sciences Disinfection and Sterilization Using Plasma Technology: Fundamentals and Future Perspectives for Biological Applications. *International Journal of Molecular Sciences*, 2019. doi: 10.3390/ijms20205216.

[7] T Kremeyer, K Flesch, O Schmitz, G Schlisio, and U Wenzel. Wisconsin In Situ Penning (WISP) gauge : A versatile neutral pressure gauge to measure partial pressures in strong magnetic fields Wisconsin In Situ Penning (WISP) gauge : A versatile neutral pressure gauge to measure partial pressures in strong magne. *Review of Scientific Instruments*, 043504, 2020. doi: 10.1063/1.5125863.

[8] Ella M. Sciamma, Roger D. Bengtson, W. L. Rowan, Amy Keesee, Charles A. Lee, Dan Berisford, Kevin Lee, and K. W. Gentle. Method to estimate the electron temperature and neutral density in a plasma from spectroscopic measurements using argon atom and ion collisional-radiative models. *Review of Scientific Instruments*, 79(10):10–13, 2008. ISSN 00346748. doi: 10.1063/1.2953577.

[9] M. Klindworth, A. Piel, A. Melzer, U. Konopka, H. Rothermel, K. Tarantik, and G. E. Morfill. Dust-free regions around langmuir probes in complex plasmas under microgravity. *Phys. Rev. Lett.*, 93:195002, Nov 2004. doi: 10.1103/PhysRevLett.93.195002.

[10] M. Klindworth, O. Arp, and A. Piel. Langmuir probe system for dusty plasmas under microgravity. *Review of Scientific Instruments*, 78(3):033502, 03 2007. ISSN 0034-6748. doi: 10.1063/1.2714036.

[11] Xi-Ming Zhu and Yi-Kang Pu. Optical emission spectroscopy in low-temperature plasmas containing argon and nitrogen: determination of the electron temperature and density by the line-ratio method. *Journal of Physics D: Applied Physics*, 43(40):403001, sep 2010. doi: 10.1088/0022-3727/43/40/403001.

[12] I. Koleva S. Iordanova. Optical emission spectroscopy diagnostics of inductively-driven plasmas in argon gas at low pressures. *Spectrochimica Acta Part B*, 62:344–356, 2007.

[13] Chun C Lin John B Boffard, R O Jung and A E Wendt. Optical emission measurements of electron energy distributions in low-pressure argon inductively coupled plasmas. *PLASMA SOURCES SCIENCE AND TECHNOLOGY*, 19, 2010.

[14] Sergey G. Belostotskiy, Tola Ouk, Vincent M. Donnelly, Demetre J. Economou, and Nader Sadeghi. Gas temperature and electron density profiles in an argon dc microdischarge measured by optical emission spectroscopy. *Journal of Applied Physics*, 107(5): 053305, 03 2010. ISSN 0021-8979. doi: 10.1063/1.3318498.

[15] John B Boffard, R O Jung, Chun C Lin, and A E Wendt. Measurement of metastable and resonance level densities in rare-gas plasmas by optical emission spectroscopy. *Plasma Sources Science and Technology*, 18(3):035017, jun 2009. doi: 10.1088/0963-0252/18/3/035017.

[16] N Ivan Arnold. *An investigation into the role of metastable states on excited populations of weakly ionized argon plasmas, with applications for optical diagnostics.* PhD thesis, Auburn University, 2017.

[17] F. M. Laggner, A. Bortolon, A. M. Rosenthal, T. M. Wilks, J. W. Hughes, C. Freeman, T. Golfinopoulos, A. Nagy, D. Mauzey, and M. W. Shafer. Absolute calibration of the Lyman- α measurement apparatus at DIII-D. *Review of Scientific Instruments*, 92(3), 2021. ISSN 10897623. doi: 10.1063/5.0038134.

[18] A. M. Rosenthal, J. W. Hughes, F. M. Laggner, T. Odstrčil, A. Bortolon, T. M. Wilks, and F. Sciortino. Inference of main ion particle transport coefficients with experimentally constrained neutral ionization during edge localized mode recovery on DIII-D. *Nuclear Fusion*, 63(4), 2023. ISSN 17414326. doi: 10.1088/1741-4326/acb95a.

[19] Drew Elliott, Derek Sutherland, Umair Siddiqui, Earl Scime, Chris Everson, Kyle Morgan, Aaron Hossack, Brian Nelson, and Tom Jarboe. Two-photon LIF on the HIT-SI3 experiment: Absolute density and temperature measurements of deuterium neutrals. *Review of Scientific Instruments*, 87(11), 2016. ISSN 10897623. doi: 10.1063/1.4955494.

[20] Saeid Houshmandyar, Stephanie H. Sears, Saikat Chakraborty Thakur, Jerry Carr, Matthew E. Galante, and Earl E. Scime. Measurements of neutral helium density in

helicon plasmas. *Review of Scientific Instruments*, 81(10), 2010. ISSN 00346748. doi: 10.1063/1.3466796.

[21] Doyle, J. G., Summers, H. P., and Bryans, P. The effect of metastable level populations on the ionization fraction of li-like ions. *Astronomy and Astrophysics*, 430(2):L29–L32, 2005. doi: 10.1051/0004-6361:200400125.

[22] A. V. Phelps and J. P. Molnar. Lifetimes of metastable states of noble gases. *Phys. Rev.*, 89:1202–1208, Mar 1953. doi: 10.1103/PhysRev.89.1202.

[23] G. J. Hartwell, S. F. Knowlton, J. D. Hanson, D. A. Ennis, and D. A. Maurer. Design, construction, and operation of the compact toroidal hybrid. *Fusion Science and Technology*, 72(1):76–90, 7 2017. ISSN 15361055. doi: 10.1080/15361055.2017.1291046.

[24] Xinxing Ma. *Non-axisymmetric equilibrium reconstruction and suppression of density limit disruptions in a current-carrying stellarator*. PhD thesis, Auburn University, 2018.

[25] Jeffrey Friedberg. *Plasma physics and fusion energy*. Cambridge University Press, 2007.

[26] Allen H Boozer. Physics of magnetically confined plasmas. *Review of Modern Physics*, 76, 2004.

[27] Donald A Spong. 3D toroidal physics: Testing the boundaries of symmetry breaking ARTICLES YOU MAY BE INTERESTED IN 3D toroidal physics: Testing the boundaries of symmetry breaking a). *Phys. Plasmas*, 22:55602, 2015. doi: 10.1063/1.4921255.

[28] M. D. Pandya, M. C. Archmiller, M. R. Cianciosa, D. A. Ennis, J. D. Hanson, G. J. Hartwell, J. D. Hebert, J. L. Herfindal, S. F. Knowlton, X. Ma, S. Massidda, D. A. Maurer, N. A. Roberds, P. J. Traverso, ; M C Archmiller, ; M R Cianciosa, D. A. Ennis, ; J D Hanson, ; G J Hartwell, ; J D Hebert, J. L. Herfindal, ; S F Knowlton, ; X Ma, ; S Massidda, D. A. Maurer, N. A. Roberds, and ; P J Traverso. Low edge safety factor operation and passive disruption avoidance in current carrying plasmas by the addition

of stellarator rotational transform. *Physics of Plasmas*, 22(11):110702, 11 2015. ISSN 10897674. doi: 10.1063/1.4935396.

[29] James D Hanson, J C Schmitt, J N Talmadge, Steven P Hirshman, Stephen F Knowlton, Lang L Lao, Edward A Lazarus, and John M Shields. V3FIT: a code for three-dimensional equilibrium reconstruction. *IOP PUBLISHING and INTERNATIONAL ATOMIC ENERGY AGENCY*, 2009. doi: 10.1088/0029-5515/49/7/075031.

[30] Mark Cianciosa. *Measurements and Modification of Sheared Flows and Stability on the Compact Toroidal Hybrid Stellarator*. PhD thesis, Auburn University, 2012.

[31] A. Kramida. NIST: Atomic Spectra Database Lines Form. https://physics.nist.gov/PhysRefData/ASD/lines_form.html, 2014.

[32] Takashi Fujimoto. *Plasma Spectroscopy*. Oxford Science Publications, 2004.

[33] M C Miller, ; J D Hanson, ; G J Hartwell, ; S F Knowlton, D A Maurer, B A Stevenson, J D Hanson, G J Hartwell, and S F Knowlton. Design and implementation of a multichannel millimeter wave interferometer for the Compact Toroidal Hybrid experiment. *REVIEW OF SCIENTIFIC INSTRUMENTS*, 83:10–332, 2012. doi: 10.1063/1.4732056.

[34] Fundamentals of Convection-Enhanced Pirani Gauges. https://www.digivac.com/fundamentals-of-convection-enhanced-pirani-gauges/.

[35] Ella Sciamma. *Plasma Spectroscopic Diagnostic Tool Using Collisional-Radiative Models and Its Application to Different Plasma Discharges for Electron Temperature and Neutral Density Determination*. PhD thesis, The University of Texas at Austin, 2007.

[36] D. C. Griffin, C. P. Ballance, S. D. Loch, and M. S. Pindzola. Electron-impact excitation of Ar+: An improved determination of Ar impurity influx in tokamaks. *Journal*

of Physics B: Atomic, Molecular and Optical Physics, 40(23):4537–4550, 2007. ISSN 09534075. doi: 10.1088/0953-4075/40/23/013.

[37] D. R. Bates, A. E. Kingston, and R. W. P. McWhirter. Recombination between electrons and atomic ions. i. optically thin plasmas. *Proceedings of the Royal Society of London. Series A, Mathematical and Physical Sciences*, 267(1330):297–312, 1962. ISSN 00804630.

[38] H P Summers, W J Dickson, M G O'Mullane, N R Badnell, A D Whiteford, D H Brooks, J Lang, S D Loch, and D C Griffin. Ionization state, excited populations and emission of impurities in dynamic finite density plasmas: I. the generalized collisional–radiative model for light elements. *Plasma Physics and Controlled Fusion*, 48(2):263, jan 2006. doi: 10.1088/0741-3335/48/2/007.

[39] ADAS: Docmentation. https://www.adas.ac.uk/manual.php.

[40] C. A. Johnson, S. D. Loch, and D. A. Ennis. ColRadPy: A Python collisional radiative solver. *Nuclear Materials and Energy*, 20(10):100579, 8 2019. ISSN 2352-1791. doi: 10.1016/J.NME.2019.01.013.

[41] A. Hartgers, J. van Dijk, J. Jonkers, and J.A.M. van der Mullen. Crmodel: A general collisional radiative modeling code. *Computer Physics Communications*, 135(2):199–218, 2001. ISSN 0010-4655. doi: https://doi.org/10.1016/S0010-4655(00)00231-9.

[42] M F Gu. The flexible atomic code. *Canadian Journal of Physics*, 86(5):675–689, 2008. doi: 10.1139/p07-197.

[43] Curtis Alan Johnson. *Theoretical modeling combined with experimental spectroscopic measurements for the diagnosis of high-Z erosion and transport applications in plasmas*. PhD thesis, Auburn University, 2020.

[44] Jonathan Tennyson. *Astronomical Spectroscopy: An Introduction To The Atomic And Molecular Physics Of Astronomical Spectra*. Imperial College Press, 1 edition, 2005.

[45] C.A. Johnson, D.A. Ennis, S.D. Loch, and C.P. Ballance. Time-dependent collisional radiative modeling of tungsten in the magnetic sheath for erosion diagnosis. *Nuclear Fusion*, 63(9):096017, aug 2023. doi: 10.1088/1741-4326/ace3d9.

[46] K. Behringer. The influence of opacity on hydrogen line emission and ionisation balance in high density divertor plasmas. *Max-Planck-Institute for Plasma Physics Report, IPP 10/5*, 1997.

[47] J. A. Bittencourt. *Fundamentals of Plasma Physics*. Springer US, 2004.

[48] Gorur G. Raju. Electron-atom collision cross sections in argon: An analysis and comments. *IEEE Transactions on Dielectrics and Electrical Insulation*, 11(4):649–673, 2004. ISSN 10709878. doi: 10.1109/TDEI.2004.1324355.

[49] G García, M Roteta, F Manero, F Blanco, and A Williart. Electron scattering by Ne, Ar and Kr at intermediate and high energies, 0.5-10 keV. *Journal of Physics B: Atomic, Molecular and Optical Physics*, 32(8):1783–1794, 4 1999. ISSN 0953-4075. doi: 10.1088/0953-4075/32/8/302.

[50] M Inokuti, R P Saxon, and J L Dehmer. Total cross-sections for inelastic scattering of charged particles by atoms and molecules. vii. systematics for atoms in the first and second row. *Int. J. Radiat. Phys. Chem., v. 7, no. 2/3, pp. 109-120*, 7(2), 4 1975. doi: 10.1016/0020-7055(75)90054-6.

[51] A.V. Phelps, Chris H. Greene, and J. P. Burke. Molecular and Optical Physics Related content Collision cross sections for argon atoms with argon atoms for energies from 0 . 01 eV to 10 keV. *Journal of Physics B: Atomic, Molecular and Optical Physics Collision*, 33(2965):2965, 2000.

[52] Lennart Minnhagen. Spectrum and the energy levels of neutral argon, Ar I. *Journal of the Optical Society of America*, 63(10):1185–1198, 1973.

[53] P Palmeri and E Biemont. Energy Levels of High-l States in Neutral and Singly Ionized Argon. *Physica Scripta*, 51:76–80, 1995.

[54] Pfeiffer vacuum. https://www.pfeiffer-vacuum.com/en/know-how/introduction-to-vacuum-technology/fundamentals/thermal-velocity/.

[55] Michael A. Lieberman and Allan J. Lichtenberg. *Principles of Plasma Discharges and Materials Processing: Second Edition*, volume 148. Wiley, 2005. ISBN 0471720011. doi: 10.1002/0471724254.

Appendix A

Spectrometer setup

This section will show a detailed description of how to set up the spectrometer.

When the spectrometer and camera are both properly set up with LightField, you will be greeted with the screen shown in A.1. I've never had to fuss about getting the camera and the spectrometer to talk to each other.

Start by attaching the fiber-optic to the spectrometer.

[H]

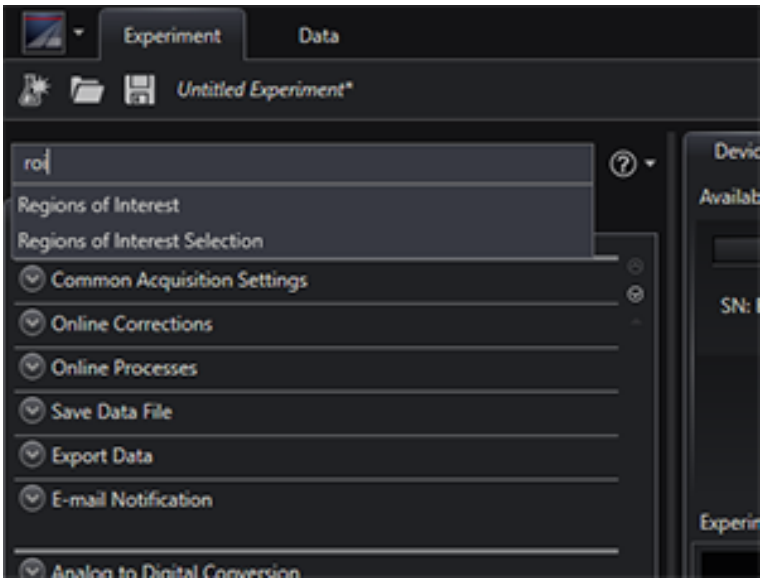

Figure A.1: Initial list of lightfield options

1. Under Common Acquisition Settings, you want Time Stamping exposure started and ended as well as frame tracking. They're easy to save. Frames to save depends on the use. If I'm looking at a steady state plasma I'll typically go with 50 because it gives me enough to do statistics with.

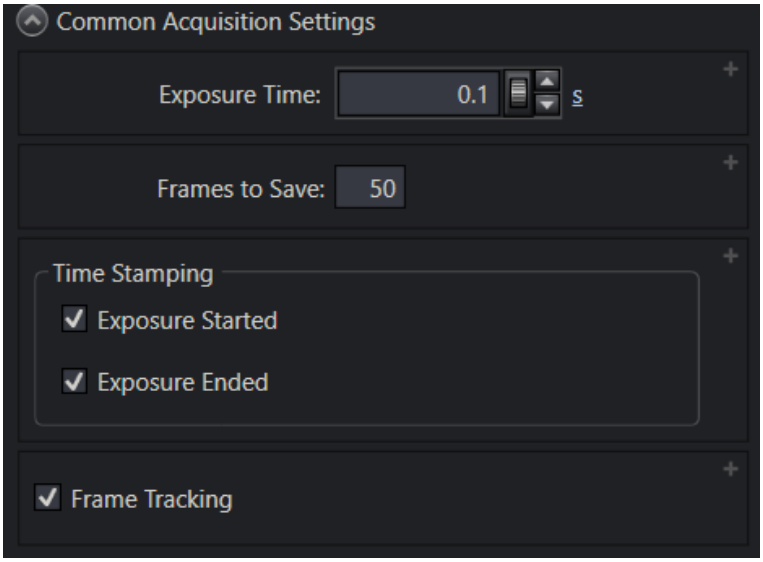

Figure A.2: Exposure time

Exposure time is something you're likely to be changing. The two ways of changing the amount of light going into the spectrometer are by changing the exposure time and the entrance slit width. Entrance slit width also affects the resolution, which may be important, and has to be kept constant for proper absolute calibration. Conversely, if you're dealing with a short plasma like CTH, you may want as small an exposure time as you can get.

While calibrating the spectrometer you'll probably want to play with the exposure time some to make the wavelength and intensity calibrations light not overexposed. Set a time here and know that you'll almost certainly end up changing it later.

2. Under "Save Data File, change the file path to whatever suits. I have never found "Increment File Name" to be necessary because the automatic file name structure includes time down to the second of when frames started being collected for that file.

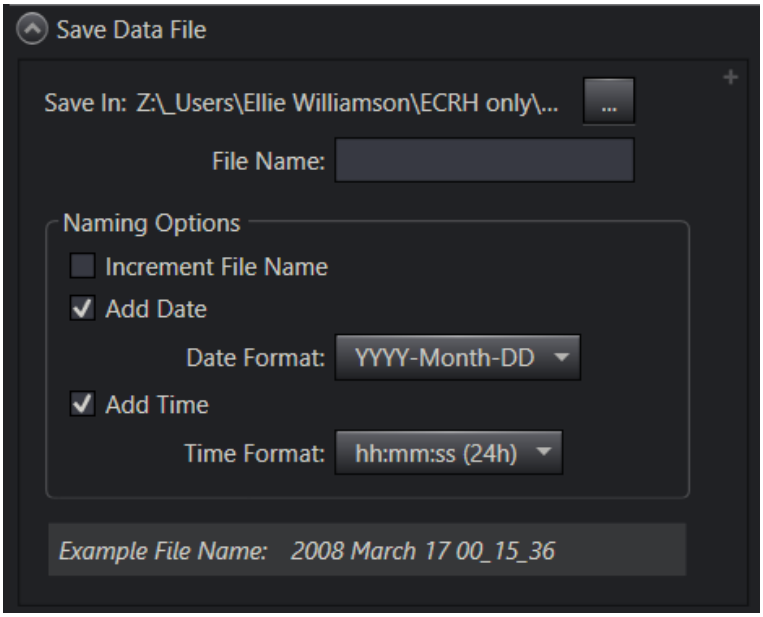

Figure A.3: File save screen

3. Under "Export Data", change "file type" to CSV, or whatever other file type you want. I've only ever used CSV. Also quite important: Change "Header labels" to "Long Names" and add to the list of columns everything important. A.4 shows the columns I've found important to save. It is possible to go back and export from the Lightfield file format, but to do so would take time.

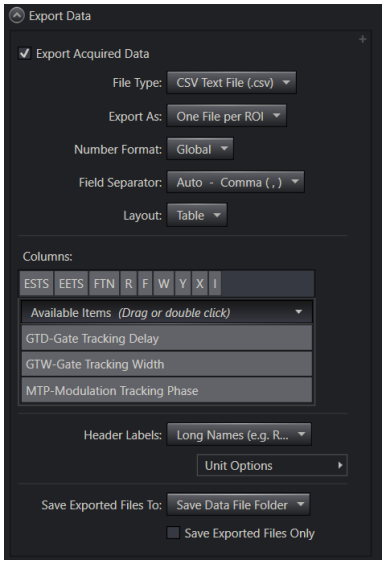

Figure A.4: Export data screen

4. Under "Spectrometer", choose the grating and center wavelength of your choice. If 0 is chosen under "Center Wavelength" you will see the full beam. By choosing 0 and opening the slit quite wide you can see the full spot coming off the fiber-optic cable. This can be used to make sure that optics are aligned properly.

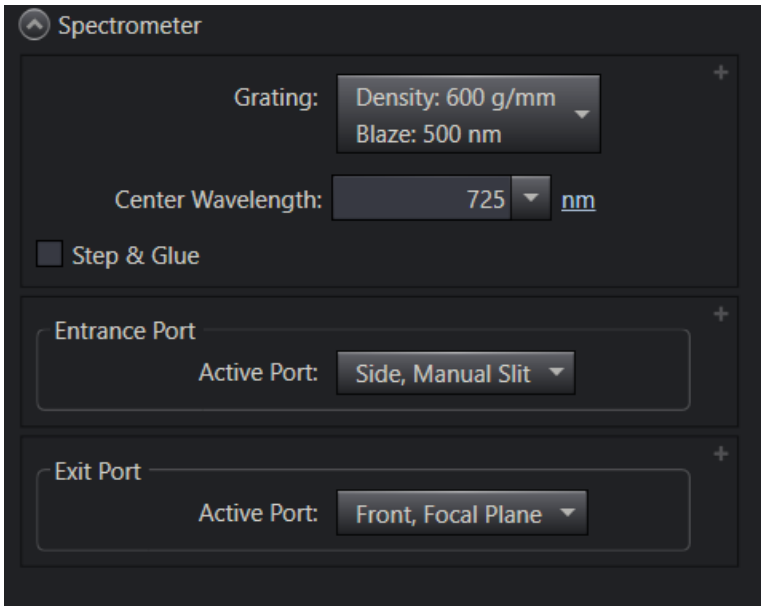

Figure A.5: Grating and wavelength selection

5. Once the proper central wavelength is chosen we'll go to wavelength calibration. I've consistently used the intellical system that comes with the device. It is imperfect: I am sometimes off by as much as 0.5 Angstroms. But I only use wavelengths distinguishable from other wavelengths, my diagnostics are intensity-dependent rather than wavelength dependent, and an error of 0.5 Angstroms in my intensity calibration will make no real difference.

   This is done by detaching the fiber from the spectrometer and attaching the wavelength calibration device. Select the "Calibration" menu. Select either PI Mercury or PI Neon/Argon. The choice will depend on your wavelength window: each has wavelength windows with more lines. There exists a handful of wavelength windows without a good

line in either selection, and in those you'll need to calibrate a different way. You will need to make sure the switch on the side is on the same element.

Click "intellical". If Lightfield thinks there are enough lines in this wavelength window it will show "fixed" as an option. You then start calibration and use the calibration it chooses. It is worth noting that Lightfield thinks that 1 is enough lines. I think you need at least 1 on each side of the central wavelength. But again, it depends on what you're doing.

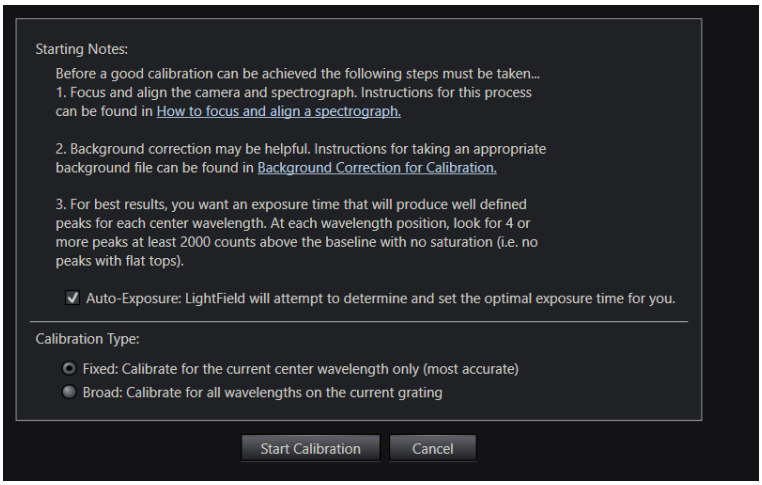

Figure A.6: Wavelength intellical selection

6. Once your wavelength is calibrated, it's time to move on to "Regions of Interest". I've only ever used "Rows Binned": this will give you all your rows binned into 1. This both takes data significantly faster and makes it easier to use the data once it's in csv format. The dropdown menu allows you to choose how many rows total you're using. It will select rows from around the central row of the camera. Collecting fewer rows will allow the camera to readout faster. 400 is the whole camera, 200 is half the camera leaving out the top and bottom quarters.

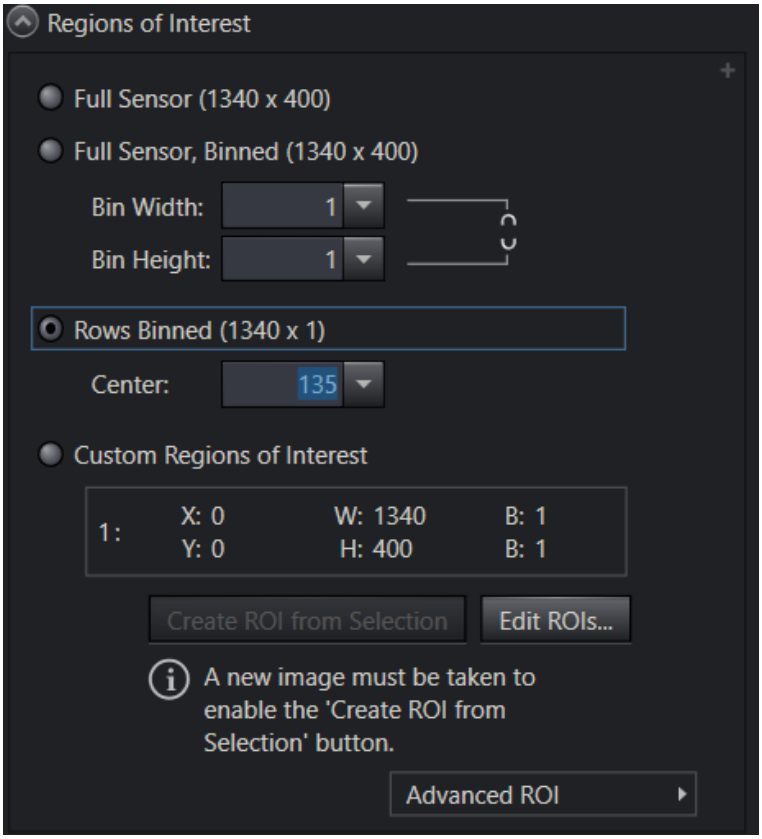

Figure A.7: Regions of interest selection

Regions of interest ends up being incredibly helpful for another reason: it's an effective way to see how much of the camera captures light.

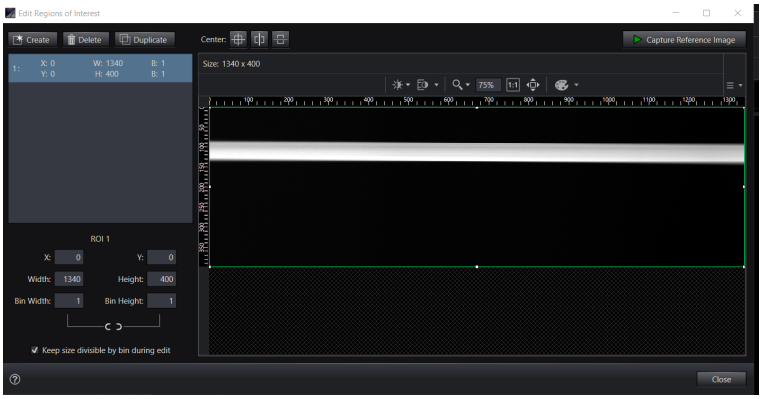

Figure A.8: Active Area

If you want to use the Princeton Instrument intensity calibration tool to intensity calibrate the spectrometer, this is where you do that.

7. Go to "Online Corrections" and allow the spectrometer to take background and flatfield spectra. This needs to be done for each wavelength window of interest with the fiber in place and the background conditions of interest (no lights for example), but only needs to be done once. When doing my absolute calibration I do a background subtraction, but I do it by taking a background spectrum and substracting it, not through Lightfield.

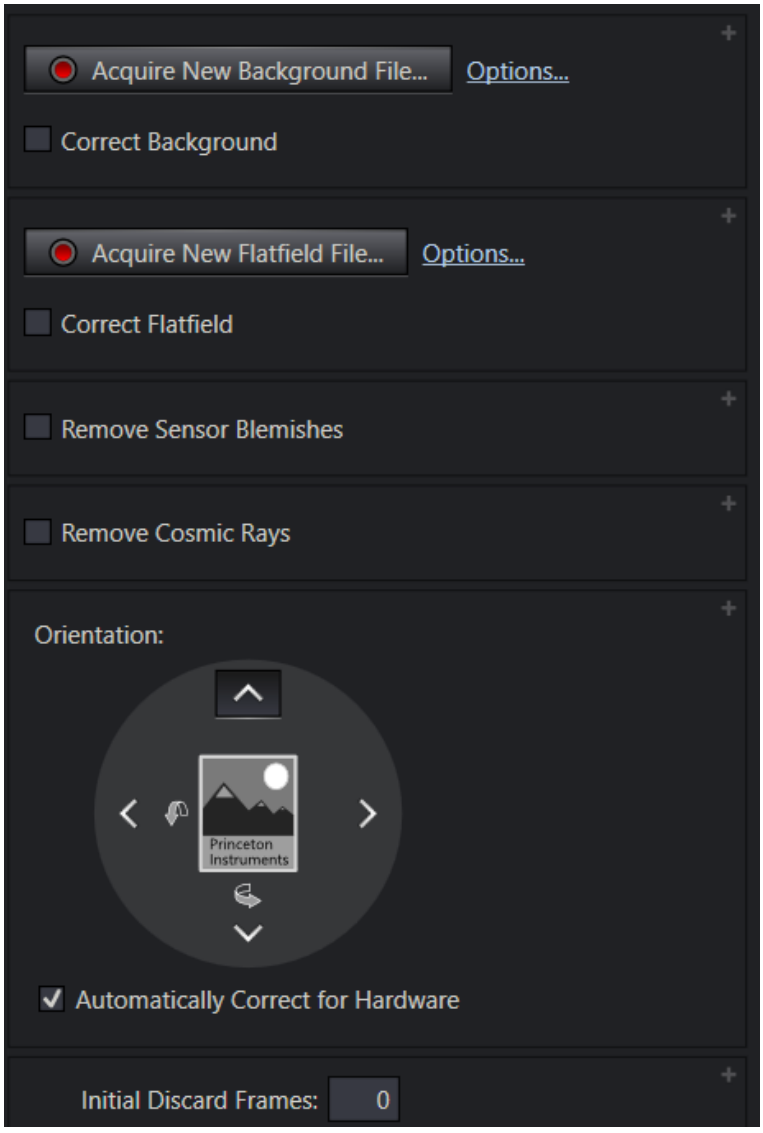

Figure A.9: Active Area

8. Next go to "Calibrations" and go to "intensity calibration". Turn the light on and allow it to do the calibration.

Other details that need to be sorted out but not in any particular order:

- I always set the shutter to always open, and, not shown in this image, set the close delay to 0. I THINK, but have not properly tested this, that even if the shutter is set to always open, Lightfield will impose whatever closing delay exists between frames.

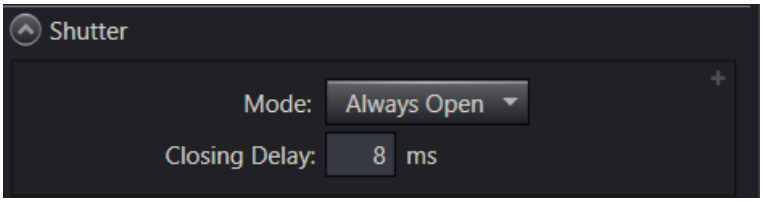

Figure A.10: Shutter selection

- During any kind of setup with the spectrometer the trigger needs to be set to not trigger. When I'm taking data on CTH and the spectrometer will be sent a trigger, this will then be set to Positive Polarity.

- Under sensor, you shouldn't do anything until the sensor temperature comes to the temperature setpoint.

  If you're only using a certain number of rows, under rows binned, you can set a corresponding inactive area here. I also set the vertical shift rate as fast as it will go.

Appendix B

Code

B.1 Neutral density calculation

```
shotnum=all_shotnums[i]
data_file = file_path + '\\'+all_data_files[i]+'.csv'
# Singly Ionized:
#calibration_file = '2021 April 14 14_44_33.csv'
#shotnum = 21041453
#data_file = '2021 April 14 15_25_36.csv'

'''
Recall that there are 2 spectra of interest: the spectrum of the calibration
source and the spectrum of the plasma. obs_wave and obs_calib_intensity pull
in the spectrum of the calibration source. The obs_wave variable has to be
the same between spectra. The code breaks if that's not the case, but it
should be anyway: the system is quite sensitive, and inconsistencies in the
wavelengths suggest that something was moved.

The start and end times that are the most important  are in the plasma data
file. By starting with this file we make sure we don't have to worry about
later.

I make sure to pull a frame that's not in the first or last few frames so I
don't have to worry about start or end issues.
```

```
,,,

# We do this first because otherwise we get into trouble with start times
[obs_wave, obs_calib_intensity,start_time,end_time]=\
ad.import_raw_spectrum(calibration_file,frame=12,frames=1)


frame_time = (end_time-start_time)/1e6 # frame exposure time in s
obs_calib_intensity = np.divide(np.array(obs_calib_intensity),\
frame_time) # this is to convert from count to count/s



interpolated_values = calibration_function(obs_wave)
# interpolated values are in radiance
calibration_factor = interpolated_values/obs_calib_intensity
# obs calib_intensity is in counts/s
interpolated_calibration_factor = si.interp1d(obs_wave,\
calibration_factor)

# interpolated_calibration_factor is now the variable that will provide the
# calibrated intensity.

# On CTH data we are able to pull a background intensity file from the same
# spectrum as the plasma data. The first and last few frames have no plasma.
# By using these as the background frame we make sure to have the background
```

```
# parameters most true to the plasma.

# On ALEXIS we can't do this because the plasma is steady state.

[background_wave, \
background_intensity,start_time,end_time]=ad.import_raw_spectrum(data_file,\
frame=3,frames=1)

# We do NOT convert from counts to counts/s on the background.

# Getting the data we actually care about
[obs_wave, \
obs_intensity,start_time,end_time]=ad.import_raw_spectrum(data_file,time=1.63)

# We subtract the background before dividing by frame time.
obs_intensity = obs_intensity - background_intensity


# We add 0.016 s to the frame time: this is how long the spectrometer reads in
# data from the camera, and it is collecting for the duration. The shutter
# does not close quickly enough to solve this. We should ostensibly add this
# to the ALEXIS data too, but the frame times are consistently long enough
# that it is not necessary.
frame_time = (end_time-start_time)/1e6
obs_intensity = np.divide(np.array(obs_intensity),frame_time) # this is to
# convert from count to count/s
```

```
# Here we convert from counts/s to radiance.
real_intensity = obs_intensity*interpolated_calibration_factor(obs_wave)
real_wave = obs_wave
# plt.plot(real_wave,real_intensity)
#
frame_start=[]
frame_end=[]
triple_probe_data= tpm.triple_probe_values(shotnum)
interferometer_data  = tpm.interferometer(shotnum)
system  = tpm.triple_probe_sys_variables(shotnum)
frame_time_start =  (start_time)/1e6+1.5 # The spectrometer trigger
# fires at 1.5 seconds.
frame_time_end = (end_time)/1e6+1.5
frame_start.append(frame_time_start)
frame_end.append(frame_time_end)

   #  This is for neutral argon


neutral_density=[]


frame_time_start =  (start_time)/1e6+1.5
frame_time_end = (end_time)/1e6+1.5
# print(frame_time_start,frame_time_end)


#frame_time_start = 1.70
```

```
#frame_time_end = 1.72
interferometer_start = ad.nearby(interferometer_data['Time'],frame_time_start)
interferometer_end = ad.nearby(interferometer_data['Time'],frame_time_end)
interferometer_density = \
np.mean(interferometer_data['Electron Density 1']['Value']\
[interferometer_start:interferometer_end])
#interferometer_density = 1.08e18

triple_probe_start = ad.nearby(triple_probe_data['Time'],frame_time_start)
triple_probe_end = ad.nearby(triple_probe_data['Time'],frame_time_end)

# I get the average Te and ne for the entire time that the frame is running.

triple_probe_temperature = \
np.mean(triple_probe_data['Temperature']['Value']\
[triple_probe_start:triple_probe_end+1])
avg_ne_TP =(np.mean(triple_probe_data['Electron Density']['Value']\
[triple_probe_start:triple_probe_end+1])/1e6)

power_start = ad.nearby(system['Power time'],frame_time_start)
power_end = ad.nearby(system['Power time'],frame_time_end)
power = np.mean(system['Power 1'][power_start:power_end])

#triple_probe_temperature = 2.59
#

interferometer_density = interferometer_density/1e6
```

```
te = ad.nearby(temperature_arr,triple_probe_temperature)
ne = ad.nearby(density_arr,interferometer_density)


if (density_arr[ne]-interferometer_density)/interferometer_density > 1:
    print("Setup density set to wrong experiment.")
    # exit()

for i in range(0,5):


    transition = ad.nearby(ar0.data['processed']['wave_air'],\
    calibration_wavelength[i])
    upper_level = ar0.data['processed']['pec_levels'][transition][0]

    # Now we need to calculate the radiance at that wavelength

    # First we're gonna do some nonsense to extract Te and ne

    radiance = ad.exp_size(real_wave, \
    real_intensity,calibration_wavelength[i])

    # print(radiance)

    # I used to have code that actually pulled the A coefficient,
    # but I found it more reliable to just make sure there's a variable
```

```
        # carrying it. Counting is hard in this context.
        einstein_A = a_coeff[i]# ar0.data['rates']['a_val'][transition+3]


        energy =  6.63e-34 * 2.99e8/(calibration_wavelength[i]*1e-9) # hc/lambda

        if radiance>1.8e-5:
            \neutral_density.append(1e-6*4*\
            np.pi*radiance/(einstein_A*energy*length*\
            ar0.data['processed']['pops'][upper_level-1,0,te,ne]))
        else:
            neutral_density.append(0)
```

B.2 nearby

```
def nearby(comparison_array,array_to_change):

    # Gives the location of the value in comparison array nearest to
    # array_to_change

    # For example, "comparison_array" could be an array of wavelengths
    # and "array_to_change" could be the wavelength of interest.
    # In theory this was supposed to work for a lot of different values of
    # array_to_change but it hasn't been tested for more than one.
```

```
    # The limitation is that if there's one value that's dead on, it will
    # find the first one and then stop.

    end_size = np.size(array_to_change)
    if end_size > 1:
        changed_array = np.zeros(end_size,dtype = int)
        for i in range(0,end_size):
            changed_array[i] = int(np.abs(comparison_array -\
            array_to_change[i]).argmin())
    else:
        changed_array = int(np.abs(comparison_array - array_to_change).argmin())

    return changed_array
```

B.3 import raw spectrum

```
    def import_raw_spectrum(file,time=1.70,frames=0,frame=15):

    # if you want to look for a particular frame, set frames=1. If you want to
    # look for a particular time, set frames=0.

    true_start = []
    wavelength = []
    intensities = []
    start_time = []
    end_time = []
    row_size=1340
    num_rows = 1
```

```
frame_size= 1340#



if frames==0:
    all_data = pd.read_csv(file)

    true_start = all_data['Exposure started time stamp'][0]

    start_times = np.unique(all_data['Exposure started time stamp'])

    close_enough = nearby(start_times,time*1e6 + true_start-1.5*1e6)



    wavelength = np.unique(np.array(all_data['Wavelength']))
    intensities = np.zeros(np.size(wavelength))

    for i in range(0,np.size(wavelength)):
        wave_locs = np.where((np.array(all_data['Wavelength']) == \
        wavelength[i]) & (all_data['Exposure started time stamp']==\
        start_times[close_enough]))
        intensities[i] = sum(np.array(all_data['Intensity'])[wave_locs])

    start_time = start_times[close_enough]-start_times[0]
    end_time = all_data['Exposure ended time stamp']\
    [np.where(all_data['Exposure started time stamp']==\
    start_times[close_enough])[0][0]]-start_times[0]
```

```
if frames == 1:
    all_data = pd.read_csv(file,nrows=frame_size,\
    skiprows=range(1,frame*frame_size-1))
    if np.size(all_data['Wavelength']>10):
        wavelength = np.unique(np.array(all_data['Wavelength']))
        intensities = np.zeros(np.size(wavelength))

        for i in range(0,np.size(wavelength)):
            wave_locs = np.where(np.array(all_data['Wavelength']) == \
            wavelength[i])
            intensities[i] = sum(np.array(all_data['Intensity'])[wave_locs])

        initial_data = pd.read_csv(file,nrows=1)

        start_time = all_data['Exposure started time stamp'][0]-\
        initial_data['Exposure started time stamp'][0]
        end_time = all_data['Exposure ended time stamp'][0]-\
        initial_data['Exposure started time stamp'][0]
    else:
        wavelength = math.nan
        intensities = math.nan
        start_time= math.nan
```

```
        end_time=math.nan


return wavelength, intensities,start_time,end_time
```

Appendix C

V3fit Parameters